ELECTROKINETIC GRADIENT-BASED FOCUSING MECHANISMS FOR RAPID, ON-CHIP CONCENTRATION AND SEPARATION OF PROTEINS

by

Gregory Jon Sommer

A dissertation submitted in partial fulfillment
of the requirements for the degree of
Doctor of Philosophy
(Mechanical Engineering)
in The University of Michigan
2008

Doctoral Committee:

Associate Professor Katsuo Kurabayashi, Co-Chair
Professor Mark A. Burns, Co-Chair
Professor Robert T. Kennedy
Professor Edgar Meyhofer

DEDICATION

To my family

For their love, support,
and for trying to understand this stuff.

ACKNOWLEDGEMENTS

Hmmmm… acknowledgements. It's kind of interesting to look back over the past several years and think about everything that has happened during my graduate career. To quote Jeffrey Lebowski [1], it's been full of "ups and downs… strikes and gutters." Seems like just last week that I showed up in Ann Arbor: somewhat energetic and excited, but mostly intimidated, and completely naive. Little did I realize the challenges and headaches that lie ahead of me (I'll forever blame my hair loss on the qualifying exam). To acknowledge all of the people that have helped me since that day seems not only exhausting, but also inadequate: some of these people I should at least be taking out for a steak dinner (or a tofu dinner… graduate school seems to have a lot of vegetarians). I guess I'll take care of that later. For now, here it goes.

I would first like to thank my advisors for their guidance, patience, and assistance. Professor Charlie Hasselbrink was the first to introduce me to the microfluidics field. I immediately admired his passion and dedication to his research and students, and I decided that he would be a great fit as my advisor. He got me started on the TGF project and pushed me to tackle some interesting problems. I appreciate his technical advice as much as our long conversations about life, sports, and whatever else came up. I am grateful to Prof. Burns, Prof. Kennedy, and Prof. Kurabayashi for their guidance and willingness to assist me in continuing my research following Prof. Hasselbrink's career "shift". I very much appreciate their patience and flexibility throughout the somewhat unique situation. I also would like to thank Prof. Meyhofer for his advice and service on my committee.

I need to thank Prof. Sun Min Kim for his assistance and friendship during his time at Michigan. Sun Min and I worked side-by-side on many aspects of the TGF project, and I thank him for his dedication and patience with the "new guy" in the lab. We also had some heated battles on the golf course, and I think in the end we're both better men for it. I thank my other labmates Taesung Kim, Sanghyun Lee, Meng-Ping

Chang, and Roel Huerta for all of their experimental help and insight. I also thank the members of the Kennedy and Burns groups, especially Zech Sandlin and Dr. Greg Roman for assisting with device fabrication, and Sean Langelier for helping with SU-8 mold fabrication.

Additionally I need to thank several people at Sandia National Labs in Livermore, CA for their assistance with the µIPG and µPLE projects presented here. I especially thank Dr. Anson Hatch for his mentorship over my two internships at the lab. I admire Anson for his professional and personal conduct, and I look forward to continuing to work with him in the future. I also thank Dr. Anup Singh, Dr. Amy Herr, Dr. Rajat Sapra, Dr. Robert Meagher, Dan Throckmorton and Carrie Kozina for their assistance and guidance in the lab.

I must acknowledge the Medtronic Fellowship Program and the U.S. Department of Homeland Security Fellowship Program for their funding support over the past four years. Without their funding, my academic career would have most certainly been much different.

I can't let my acknowledgements go by without thanking all of my friends in Ann Arbor and in our department. I may have been naive on day one, but I was smart enough to befriend some good people. Whether it be studying for quals, defending our bowling title, or bringing home an intramural championship, I couldn't have done it without them and I'm glad to say that we're still good friends. I know that they all will be successful in their future endeavors. I suppose I should give an extra thanks to Bobby Littrell because, although he may have never cleaned the bathroom, he's been a good roommate. Amazingly, four years later we still share the same apartment. He also was very helpful in modeling our TGF device (chapter 3) and provided useful insight for that publication.

Finally I need to thank my family for all of their love and support. My parents have always encouraged me to pursue whatever I wanted to do, and have provided me with whatever they could to help me get there. Some say that "parents are just like that," but I know that's not always true. I also thank my sister Amy for the encouragement and motivation that I think only an older sister can provide… I still regret my A- in eighth grade.

TABLE OF CONTENTS

LIST OF TABLES

LIST OF FIGURES

ix

LIST OF APPENDICES

ABSTRACT

Biochemical assays have seen a trend toward miniaturization as researchers strive to develop faster, more sensitive, and less expensive assays. Sample enrichment is often required in assays where dilute sample concentrations fail to meet instrumental limits of detection. This work describes three independent microfluidic techniques developed for electrokinetic concentration and separation of protein samples along imposed gradients by exploiting molecular properties unique to individual species. All three methods are embodied in microdevices with simple fabrication requirements, and are operable with solely the application of an external electric field.

In temperature gradient focusing (TGF) via Joule heating, focusing is achieved by balancing the bulk fluid flow against the temperature-dependent electrophoretic velocity of an analyte. Here a temperature gradient is induced by exploiting Joule heating along a variable-width microchannel embedded in a simple PDMS-glass device. Focusing is demonstrated with fluorescent dyes, BSA, and insulin, with concentration factors > 500 achievable in < 10 minutes. A theoretical and numerical analysis captures the transport and heat transfer behavior of this device in a quasi-1D model. Numerical simulations show good agreement with experimental results.

Next, a microscale immobilized pH gradient (μIPG) is photopolymerized in a glass microdevice for rapid isoelectric focusing (IEF) of proteins, marking the first on-chip realization of IPG-IEF methodology. Immobilines are linearly distributed via diffusion across the IPG segment prior to polymerization, and a numerical solver predicts the resulting pH profile. Focusing along a pH $3.8 - 7.0$ μIPG is demonstrated in < 20 minutes with resolving power of $\Delta pI_{min} \approx 0.040$.

Finally, polyacrylamide porosity gradients are generated by linearly varying the acrylamide monomer and bisacrylamide crosslinker concentrations along a channel prior to polymerization. Microscale pore limit electrophoresis (μPLE) is demonstrated, in

which proteins are separated based on their pore limit – the pore size at which their migration is nearly halted due to their molecular size. The "effective" pore limit is shown to be logarithmically dependent on the molecular weight of the protein. The inherent stacking effect of this process leads to improved peak resolution along the gel, as well as a means to preconcentrate dilute samples. Concentration factors > 40,000 are demonstrated.

CHAPTER 1

INTRODUCTION

Motivation

Microfluidic technology has grown remarkably over the last few decades and is being employed in an ever-expanding range of applications including biology, chemistry, clinical diagnostics, genetics, pharmaceuticals, and defense. The wealth of interest and research in the technology has spurred the emergence of fields known as *micro Total Analysis Systems (μTAS)* or *Lab-on-a-chip (LOC)* devices. The main focus of these systems is the analysis of chemical and biological samples, such as DNA and proteins. The fundamental benefits of scaling down transport phenomena to the micro (or nano) scale lead to several advantages of these systems over their macroscale counterpart. Many of these advantages are summarized in Table 1.1.

Table 1.1. Advantages of biological assay miniaturization

Microfluidic Advantage	Description
Less sample and reagent consumption	Microfluidic devices typically require $10^2 – 10^3$ less sample volume than conventional assays.
Enhanced heat transfer	Higher surface area-to-volume ratio of microfluidic channels increases effective thermal dissipation. Especially beneficial in electrokinetics as higher E-fields can be applied without inducing Joule heating.
Faster separations	Higher E-fields results in faster sample migration.
Laminar flow	Low Reynolds number flows reduce sample dispersion.
Electrokinetic manipulation	Electroosmotic flow enables fluid pumping with flat "plug-like" velocity profiles solely via applied E-fields.
Lower power consumption	Fewer components and enhanced thermal dissipation require less power input.
Parallelization	Several assays can be "multiplexed", or run in parallel on a single chip
Portability	System integration and reduced power allows for assays to be conducted using portable, hand-held device.
Improved separation efficiency	Electrophoretic separation efficiency (i.e. number of theoretical plates) proportional to L/d.

While these microsystems provide obvious benefits, they can still lack the ability to detect dilute analyte concentrations in solution due to poor limits of detection of the instrumentation. For example, fluorescence-based systems often have detection limits on the order of 1nM. However, many analytes of interest are often present in pM or fM concentrations. Therefore preconcentrating or focusing the sample prior to detection becomes crucial to enhancing an assay's sensitivity and allowing for accurate analysis.

The work presented in this dissertation is aimed at developing microfluidic technologies for rapid focusing and separation of proteins. Since the completion of the *Human Genome Project*, the genetic focus has shifted to the proteome for enhanced understanding of our biological and chemical processes [2]. Proteomics unlocks signaling pathways in physiological processes and can lead to the discovery of biomarkers which signal the presence or absence of a systemic disease. Early clinical detection of dilute disease markers can drastically increase the potential for full recovery. Proteins are also used for monitoring and detection of environmental toxins, bio-warfare agents, and narcotics. Current laboratory analytical methods are often slow and labor-intensive, leading (from a clinical viewpoint) to delayed diagnoses, reduced recovery rates, and increased hospital time and costs. Microfluidics offers the potential for portable, point-of-care (POC) diagnostics for not only bedside patient care, but also for

airport and border patrol officials, military personnel, and global public health workers [3].

However, analyzing proteins is significantly more difficult than manipulating and fractionating DNA and RNA samples. Proteins are composed of long chains of amino acids that arrange themselves into complex tertiary and quaternary structures through intermolecular bonds. Environmental influences (such as temperature, pH, salt concentrations, reducing agents, and physical stress) can disrupt these bonds and cause the protein to unravel, or denature. Therefore precise control is needed to ensure accurate protein response and behavior in an assay. Additionally, proteins have no self-replication technique, such as polymerase chain reaction (PCR) used in DNA and RNA amplification. Thus preconcentration or enrichment of dilute protein species becomes necessary.

Several previous groups have developed focusing mechanisms for microfluidic protein assays. Some techniques simply preconcentrate species prior to separation via capillary electrophoresis (CE) or other methods. Khandurina *et al* fabricated a porous sodium silicate membrane within glass microchannels for sized-based exclusion of DNA [4], and more recently large proteins [5]. Similarly, Hatch *et al* locally polymerized highly-concentrated polyacrylamide membranes that trap proteins prior to sizing with SDS-PAGE [6]. In a related technique, Wang *et al* electrokinetically trapped proteins near a microchannel-nanochannel junction using the ion depletion zone that forms due to concentration polarization near the interface [7]. More recently, Kim *et al* achieved a similar effect with a simple PDMS/glass device in which nanochannels are formed at the bonded interface [8].

Other focusing mechanisms electrokinetically separate and concentrate species along an imposed gradient. In isotachophoresis [9], analytes are separated into zones based on mobility by loading between a leading (high mobility) electrolyte and a trailing (low mobility) electrolyte. Electric field gradient focusing [10, 11] was developed in Cornelius Ivory's lab as a similar technique that balances hydrodynamic flow with a gradient in electric field established by individually-controlled electrodes along the channel. Isoelectric focusing (IEF) separates species based on their unique isoelectric points (pH at which the net molecular charge = 0) along an established pH gradient. IEF

is commonly used as the first step in a macroscale two-dimensional separation. While several researchers have attempted IEF miniaturization [12, 13], the technique has struggled due to difficulties in establishing and stabilizing a pH gradient along a free-flow microdevice.

In this work, three independent yet similar on-chip methods are presented in which species migrate electrokinetically along an imposed gradient and are focused by exploiting intrinsic molecular properties, including a protein's temperature-dependent electrophoretic mobility, isoelectric point, and molecular mass. The microdevices are all fabricated with simple techniques and geometries using standard PDMS and glass substrates, and all operate solely with the application of external electrical fields without the requirements of complex valves, pumps, thermal regulators, etc. By enacting these design protocols we have produced highly reproducible, reliable, rapid, and inexpensive proteomic tools.

Organization of Dissertation

This dissertation is comprised of three original techniques for the focusing and separation of proteins within microfluidic devices. The manuscript is organized as follows.

Chapter 2 presents an experimental study of temperature gradient focusing (TGF) exploiting an inherent Joule heating phenomenon. A simple variable-width PDMS device delivers rapid and repeatable focusing of model analytes using considerably low energy. High electric potential applied to the device induces a temperature gradient within the microchannel due to the channel's variable-width, and the temperature-dependent mobility of the analytes causes focusing at a specific location. The PDMS device also shows simultaneous separation and concentration capability of a mixture of two sample analytes in less than 10 minutes. An experiment combining Joule heating with external heating/cooling further supports the hypothesis that temperature is indeed the dominant factor in achieving focusing with this technique.

Chapter 3 provides a detailed theoretical and numerical analysis of temperature gradient focusing (TGF) via Joule heating. The governing transport equations are presented, analyzed, and implemented into a quasi-1D numerical model to predict the resulting temperature, velocity, and concentration profiles along a microchannel of varying width under an applied electric field. Numerical results show good agreement with experimental trials presented in Chapter 2. The model is used to analyze the effects of varying certain geometrical and experimental parameters on the focusing performance of the device. Simulations also help depict the separation capability of the device, as well as the effectiveness of different buffer systems used in the technique. The analysis provides rule-of-thumb methodology for implementation of TGF into analytical systems, as well as a fundamental model applicable to any lab-on-a-chip system in which Joule heating and temperature-dependent electrokinetic transport are to be analyzed.

Chapter 4 presents the first successful adaptation of immobilized pH gradients (IPG's) to the microscale (μIPG's) using a new method for generating precisely-defined polymer gradients on-chip. Gradients of monomer were established via diffusion along 6mm flow-restricted channel segments. Precise control over boundary conditions and the resulting gradient is achieved by continuous flow of stock solutions through side channels flanking the gradient segment. Once the desired gradient is established, it is immobilized via photopolymerization. Precise gradient formation was verified with spatial and temporal detection of a fluorescent dye added to one of the flanking streams. Rapid (< 20 minutes) isoelectric focusing of several fluorescent p*I* markers and proteins is demonstrated across pH 3.8 – 7.0 μIPG's using both denaturing and non-denaturing conditions, without the addition of carrier ampholytes. The μIPG format yields improved stability and comparable resolution to prominent on-chip IEF techniques. In addition to rapid, high-resolution separations, the reported μIPG format is amenable to multiplexed and multidimensional analysis via custom gradients as well as integration with other on-chip separation methods.

In Chapter 5, precise and well-controlled polyacrylamide porosity gradients are photopolymerized in microchannels for conducting microscale pore limit electrophoresis (μPLE) of proteins. Porosity is controlled via distributions of acrylamide monomer and bisacrylamide crosslinker. μPLE provides high-resolution fractionation of complex

samples based on the spatial dependence of each species' electrophoretic pore limit - the porosity at which a protein's electrophoretic mobility is negligible due to its molecular size. This method can be used to preconcentrate dilute samples by exploiting the stacking phenomenon associated with an analyte's decreasing electrophoretic mobility.

Finally, Chapter 6 provides conclusions and future investigations that may stem from these projects. Conceptual devices are included that operate based on the principles presented here. The objective of this dissertation and future research is the development of simple, rapid, reliable, sensitive and commercializable micro-analytical devices.

Table 1.2 below summarizes and compares the techniques presented in this work.

Table 1.2. Summary of investigated techniques

Technique	Established gradient	Molecular separation dependencies	Fabrication simplicity	Demonstrated focusing time	Demonstrated concentration factor (c/c_0)	Advantage over conventional method
Temperature gradient focusing via Joule heating (TGF)	Joule heating-induced axial temperature gradient	μ_{ep} temperature dependence in specific buffers (primarily due to mass and charge)	Very simple (PDMS slab bound to glass slide)	< 10 minutes	~500	- Completely on-chip - No external heating or cooling required - No external pressure regulation required
Isoelectric focusing across microscale immobilized pH gradients (µIPG)	pH gradient immobilized on polyacrylamide matrix	Isoelectric point (charge vs. pH)	Simple (polyacrylamide gel polymerized in glass channels)	< 20 minutes	NA	- ~100-fold improvement in separation time - >1000-fold improvement in req'd sample volume
Microscale pore limit electrophoresis (µPLE)	Polyacrylamide porosity gradient	Mass	Simple (polyacrylamide gel polymerized in glass channels)	Several hours, but can be improved by adjusting channel length	> 40,000	- Simpler and more reliable fabrication scheme - Easy incorporation with other on-chip separation mechanisms

CHAPTER 2

RAPID, LOW-POWER CONCENTRATION AND SEPARATION USING TEMPERATURE GRADIENT FOCUSING VIA JOULE HEATING

Introduction

Species preconcentration and separation are significant challenges in the design of microfluidic chemical analysis systems. In a typical electrophoretic separation, the sample concentration is often too dilute for adequate detection. This lack of sensitivity results in either an inaccurate reading or a considerable waste of a limited sample volume.

Several preconcentration techniques have been developed and studied. Many methods trap the analyte against a porous membrane that prohibits the passing of large molecules such as DNA [4, 5, 7, 14]. Other methods rely on the establishment of a field gradient to suppress the mobility of the analyte at a single location. For example, isoelectric focusing is a commonly-used technique that focuses an analyte at its specific isoelectric point along a pH gradient [15, 16], and isotachophoresis uses variable ion mobility zones for sample focusing [9]. Similar methods rely on electric field gradients to suppress the net analyte velocity at a point in a channel [11, 17]. While powerful, many of these techniques are difficult to apply to a broad range of analytes due to the specificity of the method to a certain type of molecule.

Microfluidic temperature gradient focusing (TGF) is a new field gradient focusing method introduced by Ross and Locascio in 2002 [18]. TGF is a technique that focuses and separates charged analytes by balancing electrophoretic velocity against the bulk velocity of the buffer. The electrophoretic mobility of a charged species is highly

temperature-dependent. TGF exploits this property to suppress the net analyte velocity (electrophoretic + bulk) at a certain location along a temperature gradient, resulting in a concentration of species at that unique point. Ross and Locascio demonstrated successful focusing using both external heating and cooling as well as Joule heating along a variable cross-sectional area microchannel. Because electrophoretic mobility is a unique property of a given analyte, TGF allows for species separation by concentrating different analytes at unique locations along the temperature gradient. The technique has been successfully used to achieve DNA hybridization [19] and chiral separations [20].

TGF is an excellent technique for concurrent signal enhancement and separation of a mixture of analytes, however it currently has certain shortcomings which limit its specificity and applicability. From the standpoint of device miniaturization, the main issue is energy consumption: previous TGF approaches use external heating and cooling equipment to establish a temperature gradient along a channel. Establishing a temperature gradient across the entire chip requires a significant amount of energy; for example, two 1×1 cm thermoelectric devices with coefficient-of-performance (COP) of about 1.5, require at least 2kJ of energy to maintain a 50 ºC temperature difference across a chip for 5 minutes [21]. Assuming 50% of the analysis cycle is devoted to TGF, this corresponds to only 5 runs if powered by a typical cell-phone battery, and this does not account for other power requirements (such as the HV power supplies). This limits the technique's applicability to portable applications. This chapter explores the use of Joule heating within the buffer itself, which uses considerably less power.

A secondary concern with TGF is that specific buffers are required; the more commonly-used buffers will normally yield negligible or highly-unstable focusing. In this chapter, although we do not look at a wide variety of buffers, we do illustrate a simple step-by-step approach to designing a TGF system for a set of analytes that can predict whether an analyte can be focused *a priori*. We hope that this assay-development methodology accelerates the rate of TGF's adoption as an analytical technique.

Underlying both of these aims is a need for rule-of-thumb prediction of thermal characteristics of TGF-based microdevices, especially the prediction of temperature distributions and criteria for stable focusing. In this chapter we also show that it is possible to combat poor resolution via a secondary electrophoretic separation. In the

following chapter (chapter 3) we will delve further into computational prediction of temperature distribution and mass transport (*e.g.* focusing rates, and the width of focused bands).
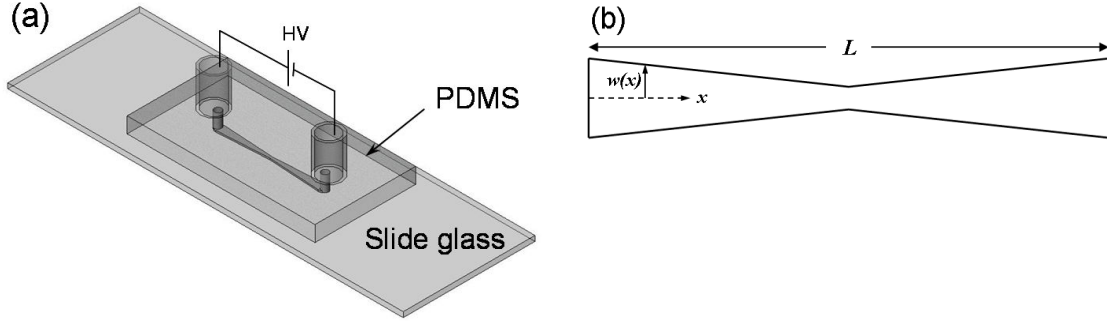
Figure 2.1. (a) Schematic drawing of experimental micro-device composed of a PDMS slab with a patterned microchannel, a slide glass substrate and two sample reservoirs. (b) Geometrical schematic of patterned microchannel. The channel width varies with *x*, the channel length is *L*, and its depth is *d*. The channel width is symmetric and is narrowest at *L/2*.

Theory

Temperature Gradient Focusing works analogously to isoelectric focusing. The bulk fluid velocity, u_{bulk}, arising from electroosmotic flow (EOF) and/or pressure driven flow (PDF) opposes the electrophoretic drift velocity, u_{ep}, of an analyte. Since u_{ep} is a function of temperature, T, if we make T a function of x (a coordinate along the length of the channel), then u_{ep} is a function of x. The net velocity, $u_{net} = u_{bulk} + u_{ep}$, can be manipulated to achieve focusing at a specific location along a channel if $u_{net} = 0$ and $\frac{\partial u_{net}}{\partial x} < 0$. Conversely, if $\frac{\partial u_{net}}{\partial x} > 0$ at the spot where $u_{net} = 0$, then depletion occurs.

The quasi 1-D transport equation for the concentration of a species, c, at any location i along the channel, neglecting diffusion, is:

$$A_i \frac{\partial c_i}{\partial t} = -\frac{\partial}{\partial x}\left[A_i\left(u_{bulk,i}c_i + u_{ep,i}c_i\right)\right] \qquad (2.1)$$

where A is the cross-sectional area of the channel. Simplifying this equation using the continuity condition, $\frac{\partial}{\partial x}(u_{bulk}A) = 0$, (assuming constant mass density of the solution) yields:

$$A_i \left[\frac{\partial c_i}{\partial t} + (u_{bulk,i} + u_{ep,i}) \frac{\partial c_i}{\partial x} \right] = -c_i \frac{\partial}{\partial x}(A_i u_{ep,i}) \tag{2.2}$$

At steady state, $\frac{\partial c_i}{\partial t} = 0$, and the resulting differential equation can be solved to yield:

$$\frac{c_{x=x1}}{c_{x=x0}} = \frac{(u_{bulk,x0} + u_{ep,x0})A_{x0}}{(u_{bulk,x1} + u_{ep,x1})A_{x1}} \tag{2.3}$$

Thus when the net velocity at x_1 is zero, the concentration theoretically approaches $\pm\infty$, but diffusion and dispersion (ignored in the above analysis) will, of course, prevent the singularity from occurring in reality.

The electrophoretic and electroosmotic mobilities, μ_{ep} and μ_{eof}, are temperature-dependent due primarily to the varying viscosity of the buffer solution, and zeta potential of the channel surface, with temperature. This phenomenon allows for a variable u_{net}, and proper device design will yield focusing along the microchannel.

In this work the temperature gradient will be created by exploiting the Joule heating effect within the bulk fluid due to the applied electric field. If the microchannel is much smaller than the medium in which it is formed (e.g., the glass substrate), the 1-D steady heat transfer equation, considering only Joule heating within the channel and radial heat conduction away from the channel, can be written in an approximate form:

$$\frac{I^2}{\sigma_i(T_i)d_i w_i} = Kk \frac{T_i - T_\infty}{d_i} w_i \tag{2.4}$$

where I is the current through the channel, $\sigma(T)$ is the electrical conductivity, d is a length scale on the order of the depth of the microchannel, w is the channel width, k is the thermal conductivity of the glass surrounding the microchannel, and K (which is $O(1)$) accounts for the geometry of the microchannel. If we assume that σ is roughly proportional to temperature difference above ambient, then the temperature varies approximately inversely with the channel width. Thus regions of narrower cross-sectional area along the channel will reach higher temperatures, and a temperature

gradient is induced.   This simple rule-of-thumb estimate forms the design basis of the system.

Experimental Materials and Methods

Materials

900mM Tris-Borate buffer (900mM Tris, 900mM Boric acid, pH 8.0) and phosphate buffer (dibasic sodium phosphate, 20mM, pH 7.2) solution were used for the buffer systems. Fluorescein isothiocyanate conjugate bovine serum albumin (FITC-BSA) (Sigma-Aldrich, St. Louis, MO) and fluorescein-Na (Sigma-Aldrich, St. Louis, MO) were used for focusing experiments and each sample was diluted with the buffer solution at several concentrations (100nM, 25µM and 0.1mM). Rhodamine B dye (Molecular Probes) diluted with the 900mM Tris-Borate buffer was used to measure the temperature distribution in the microchannel. Protein sample was kept in a freezer to prevent deterioration and all liquid samples were filtered with a 0.1 µm syringe filter (Whatman, Maidstone, UK) to remove particulates.

Microchip fabrication

The microchannel system in Figure 2.1 was fabricated by casting poly(dimethylsiloxane) (PDMS) over an SU-8 photoresist (SU 8-2010, MicroChem Inc., Newton, MA) mold on a silicon substrate fabricated by photolithography, as previously described [22, 23]. Briefly, a mixture of the PDMS prepolymer and the curing agent (Sylgard 184, Dow Corning, Midland, MI) was prepared and degassed. A 5:1 mass ratio of prepolymer and curing agent was used to increase the rigidity of the cured PDMS slab, as described previously [24]. The uncured mixture was poured over the mold in a Pyrex Petri dish about 4mm-thick and cured for 1 hour at 150°C. The cured PDMS was detached from the mold and 2mm-diameter holes for reservoirs were punched vertically through the slab. The PDMS slab with a designed microchannel pattern and a slide glass substrate were treated with an air plasma of 100 W RF power in ~200mTorr vacuum using a PlasmaPrepII system (SPI supplies, West Chester, PA) for 3 minutes, then

contacted together and heated at 150°C for 15 minutes to create an irreversible bond [22, 23]. Cylindrical glass reservoirs (1cm-long, 5mm inner diameter) were bonded concentrically over the holes on the PDMS slab using UV-curable optical adhesive (Norland, New Brunswick, NJ) with a UV lamp for 10 minutes.

Temperature measurement

The temperature gradient inside a microchannel produced by Joule heating was measured with a fluorescence thermometry method previously described [25, 26]. Briefly, electric field was applied to a microchannel filled with a 900mM Tris-Borate buffer containing 100μM rhodamine B dye, which has a strongly temperature-dependent quantum efficiency, through platinum electrodes (A-M Systems, Carlsborg, WA) placed in the reservoirs using a high voltage power supply (PS350, Stanford Research Systems, Sunnyvale, CA). The fluorescence intensity of the rhodamine B was monitored using an inverted fluorescence microscopic system (IX-71, Olympus, Japan) equipped with a spectral filter set for rhodamine B (excitation: 500- 550 nm, emission: > 565nm) and a 100W mercury lamp. A CCD camera (Hamamatsu, Japan) was mounted on the microscope for image acquisition and IPLab 3.6 software (Scanalytics, Fairfax, VA) was used for camera control and image processing. To prevent photobleaching, a neutral density filter (ND 1.0, Omega Optical, Brattleboro, VT) was installed to reduce excitation light intensity. The ratio of the fluorescence intensity after applying electric field to the intensity of initial state (room temperature) was used to calculate the temperature at each point of the microchannel using a calibration curve generated from the intensity measurement with a thermostated silica capillary.

Temperature-dependent mobility measurements

The electrophoretic and net mobilities, $\mu_{ep}(T)$ and $\mu_{net}(T)$, were measured using a photobleached dye imaging method similar to techniques previously described [27-29]. The ends of 10cm-long × 50μm-inner diameter capillaries were connected to plastic tubing and a small viewing region was created in the center of the capillary using a razor blade. The entire system was rinsed with DI water for 5 minutes, flushed with air, filled

with the analyte/buffer solution, and secured along the bottom of a thermal water bath with a viewing window sitting above an inverted fluorescent microscope. The reservoirs were also held in the thermal bath to ensure that the entire capillary system was maintained at the same temperature.

To measure the fluid velocity through the capillary, a small region of the capillary was exposed to a focused laser beam (496nm, 200mW, Melles Griot Series 43 Ion Laser, Carlsbad, CA) for 3 seconds using an electronic shutter controller (ThorLabs SC10, Newton, NJ). The photobleaching creates a concise dark region within the fluorescent sample. Upon removal of the laser beam, electric potential was immediately applied through platinum electrodes in the reservoirs and the migration of the photobleached region was captured at a known frame rate (typically 100ms/frame) through a CCD camera using image processing software (NI Vision Assistant 7.1.1, National Instruments). An in-house written Matlab (Mathworks, Natick, MA) code was used to determine the velocity of the photobleached region, from which the mobility can be determined using $\mu = u/E$.

To measure the electrophoretic mobility, $\mu_{ep}(T)$, 50μm-inner diameter *Zero Flow* fused silica capillaries (MicroSolv, Long Branch, NJ) were used. These capillaries are coated internally to suppress the EOF in the channel. Regular, uncoated 50μm-inner diameter fused silica capillaries (Polymicro Technologies, Phoenix, AZ) were used to measure $\mu_{net}(T)$. The electroosmotic mobility was then calculated using the relation $\mu_{net}(T) = \mu_{eof}(T) + \mu_{ep}(T)$.

Focusing measurement

The focusing of FITC-BSA and fluorescein-Na was performed in the microchannel shown in Figure 2.1. The device was treated with air plasma of 100W RF power in ~ 200mTorr vacuum for 90 seconds to enhance the hydrophilicity of the channel surface. The microchannel and each reservoir were then filled with DI water and flushed out to clean the channel. The buffer solution used for diluting the sample was introduced into the channel to capture a background image for image processing and flushed out after 5 minutes. The microchannel and reservoirs were then filled with sample solution and platinum electrodes were placed in each reservoir to apply the electric field.

Fluorescence imaging of the sample was acquired by the same fluorescence microscopic system described in the temperature measurement section, equipped with a different filter set (488nm) for FITC and fluorescein.

For the combined Joule heating and external heating focusing experiments, two small thermoelectric heat sinks (Melcor OT 1.5-31-F2A, Trenton, NJ) were placed on the bottom of the glass substrate using thermal grease (Cool-Grease, Melcor) to promote conduction, attached to a ¼" thick copper block, and operated by a DC power supply (Tektronix PS280, Beaverton, OR). During either operation (cooling or heating), the same power was applied to both heat sinks to ensure that the heat flux to the glass substrate was as uniform as possible. For reliable quantification of the sample, all experiments were performed with a fresh new device to prevent nonspecific binding of labeled protein on the channel surface [30-33], and corrections for background were implemented.

Results and Discussion

The experiments conducted in the present work were performed with 2 primary goals. First, bulk fluid and molecular electrophoretic mobilities are measured at various temperatures in different buffers to illuminate the advantage certain buffers have in achieving TGF. Secondly, a microdevice was fabricated to show that concentration and separation via TGF can be achieved very simply by utilizing the electric potential through a microchannel to provide a temperature gradient via Joule heating. This device is then combined with an external heating/cooling system to show both the effect of temperature on the focusing capability, and that TGF can be performed with more commonly-used buffers.

Mobility and temperature measurements

The electrophoretic and net mobilities, $\mu_{ep}(T)$ and $\mu_{net}(T)$, of 0.1mM fluorescein-Na were measured in both 900mM Tris-Borate buffer and 20mM phosphate buffer using the photobleached dye imaging method described earlier, with sample images shown in

Figure 2.2. To ensure that no PDF was present in the system, tests were completed in which the velocity was measured with no applied external field. Measurements at temperatures ranging from 25°C to 79°C were achievable with the experimental apparatus. The electroosmotic mobility, $\mu_{eof}(T)$, was calculated using the relation $\mu_{eof}(T) = \mu_{net}(T) - \mu_{ep}(T)$.
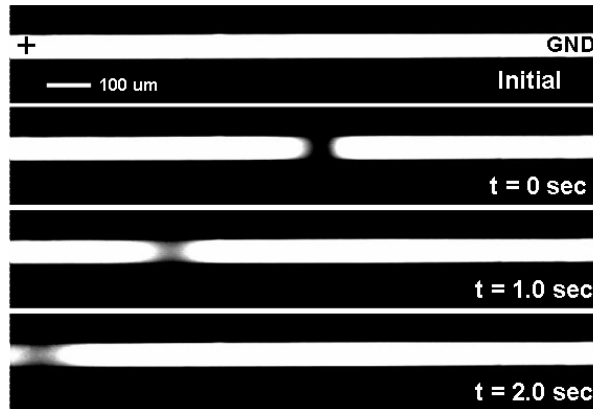
Figure 2.2. Time sequence images of the electrophoretic velocity of bleached fluorescein-Na in a 50 μm coated (*Zero Flow*) silica capillary held in a thermal bath. The capillary is filled with the 0.1mM fluorescein-Na in 900mM Tris-Borate buffer solution, and a small region is exposed to a laser for 3 seconds to photobleach the dye. A 2500V electric potential (~150V/cm) is applied to both ends of the capillary and the bleached plug migrates following the electric field. The mobility of the fluorescein-Na solution is calculated through image processing.
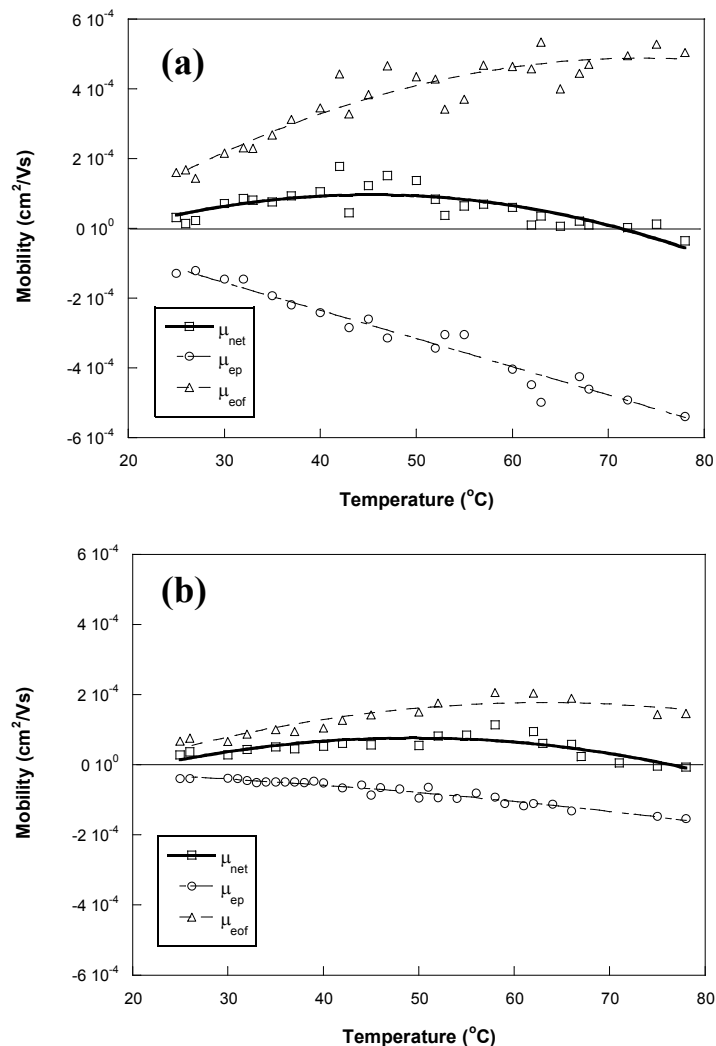
Figure 2.3. Temperature-dependent mobility profile of 0.1mM fluorescein-Na in (a) 900mM Tris-Borate buffer and (b) 20mM phosphate buffer. The square markers represent the net mobility variations of the fluorescein-Na and the circle markers represent the electrophoretic mobility variations. The electroosmotic mobility (triangle markers) is calculated by subtracting the electrophoretic mobility from the net mobility. Each line is a 2nd order polynomial fitted curve.

Figure 2.3(a) shows that, as expected, the magnitude of $\mu_{ep}(T)$ increases with temperature in the 900mM Tris-Borate buffer. The curve exhibits the inverse proportionality of μ_{ep} with viscosity of the buffer throughout the entire temperature range. The $\mu_{net}(T)$ curve shows that electroosmosis dominates the migration of the sample at low temperatures. At ~50 ºC, however, the curve begins to decrease towards zero and at temperatures > ~70 ºC the net mobility is idle and even shows that electrophoresis may

dominate at high temperatures. Note that while $\mu_{ep}(T)$ continues increasing at high temperatures, $\mu_{eof}(T)$ appears to plateau.

Similar trends are seen in Figure 2.3(b) for the 20mM phosphate buffer. However, the magnitudes of the mobilities and $\dfrac{\partial \mu_{net}}{\partial T}$ are less than half those seen in Figure 2.3(a). The shallower $\dfrac{\partial \mu_{net}}{\partial T}$ gradient suggests that focusing will be more difficult with this buffer. A steeper $\dfrac{\partial \mu_{net}}{\partial T}$, such as that for the 900mM Tris-Borate buffer, corresponds to a steeper $\dfrac{\partial u_{net}}{\partial x}$ along the channel and both an increased probability of focusing and an increased concentration magnitude.

The temperature increase within the microchannel is generated by the inherent Joule heating effect from an applied electric potential. The cross-sectional area variations of the microchannel create a temperature gradient because the current density of a narrow part of the channel is higher than it is in the wider part, leading to a temperature change inversely proportional to the square of the channel diameter or width.

The temperature within the microchannel was measured using the temperature-dependent fluorescence intensity of 100μM rhodamine B in 900mM Tris-Borate buffer solution, with the calibration curve shown in Figure 2.4. Figure 2.5(a) shows the temperature variations along the center line of the microchannel after applying 1200V, and Figure 2.5(b) shows the temperature distribution at 5 minutes (inverse false color image of rhodamine B fluorescence). As expected, the temperature near the narrowest region of the channel is higher than the wider regions. However, the highest temperature point is slightly off-center because of convectional heat transfer from the electroosmotic flow. At the beginning of the run, the temperature increase is quite fast but the rate slows with time. Establishing this temperature profile required only ~25J of energy, which is about 1/80th of the energy needed to obtain the same profile using external thermoelectric heat sinks, thus supporting the low-power advantage of this system.
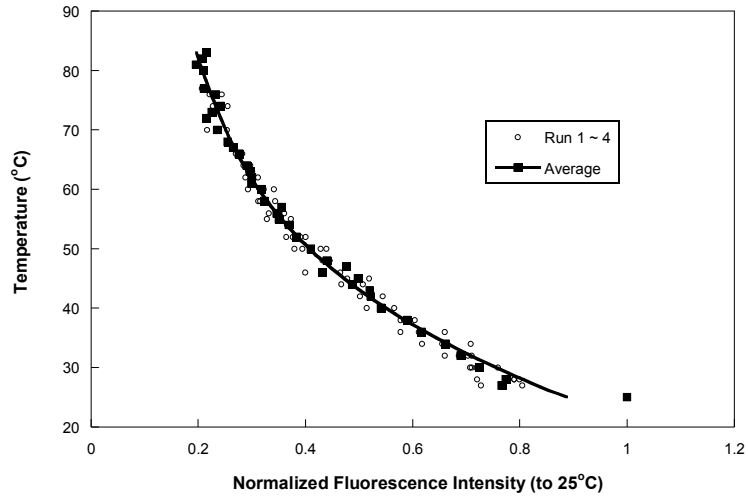
Figure 2.4. Temperature calibration curve for 100μM rhodamine B in 900mM Tris-Borate buffer. Fluorescence intensity at different temperatures is normalized by the intensity at the room temperature (25°C). Circle markers represent the experimental data of 4 runs and square markers represent the average. The resulting fitted exponential calibration curve is *T (°C) = 105.05 × exp(–1.6949 × I)*.
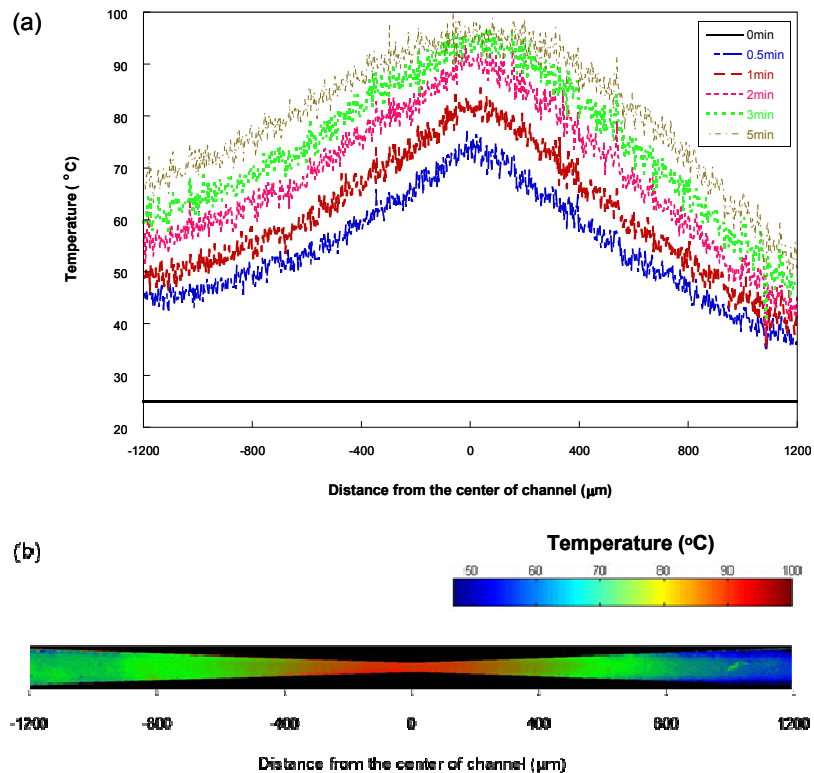
Figure 2.5. Temperature profile of 900mM Tris-Borate buffer in the analog shape microchannel due to an applied electric potential of 1200V and the temperature distribution at 5 minutes. (a) Temperature profile along centerline of microchannel. (b) Temperature distribution at 5 minutes after applying 1200V (inverse false color image of rhodamine B fluorescence in channel).

Temperature gradient focusing by Joule heating

Several focusing experiments were performed with two model analytes (Fluorescein-Na and FITC-BSA, both of them are negatively charged at the buffer pH values used) in 900mM Tris-Borate buffer in the microchannels. Figure 2.6(a), (b) and (c) show the focusing of fluorescein-Na, FITC-BSA, and FITC-insulin, respectively, after applying 1200V for 5 minutes in individual runs. Initially, the microchannel was filled with a diluted sample solution uniformly distributed within the channel. After high electric potential was applied to the channel, the analytes were slowly focused at the central region of the microchannel and the analyte concentration increased at this location.

19
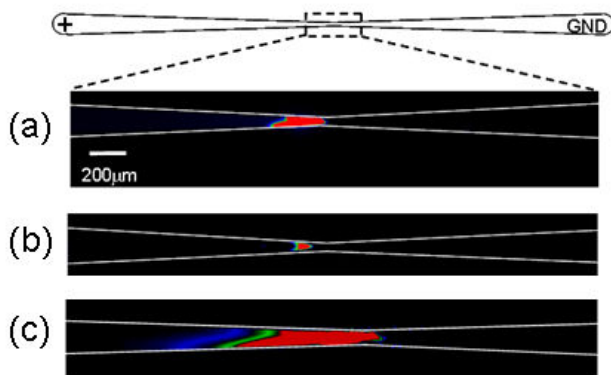
Figure 2.6. Images after 5 minutes of sample analyte focusing with an applied electric potential of 1200V in individual runs. Focusing of (a) 25μM fluorescein-Na, (b) 100nM FITC-BSA, and (c) 100nM FITC-insulin in 900mM Tris-Borate buffer. Each image is a magnified view of the middle region of the microchannel. Approximate E-field in center region of channel: 2.5×10^3 V/cm.

The preconcentration capability of this system was investigated by comparing the fluorescence intensity of the focused sample with that of several standard concentration samples (5μM, 10μM, and 20μM). Figure 2.7 shows the concentration of 100nM FITC-BSA due to an applied 1200V in the microchannel. At least 200-fold concentration was achieved in just 2 minutes. Fluorescence intensity is measured at the location of maximum intensity over the entire microchannel because the focused sample plug is quite wide and the intensity is not uniform within this plug.
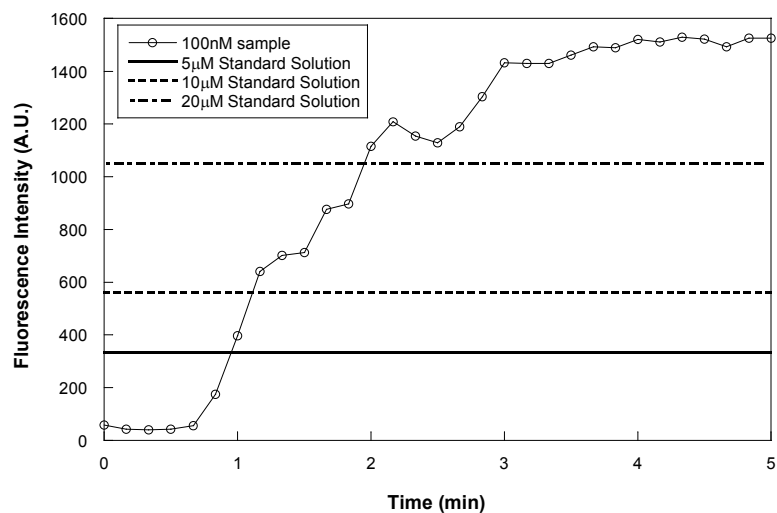
Figure 2.7. Concentration of 100nM FITC-BSA due to applied 1200V in analog microchannel. Concentration of 100nM sample is compared with standard concentration samples (5μM, 10μM, and 20μM). At least 200-fold concentration was achieved in 2 minutes. Fluorescence intensity is measured at the location of maximum intensity over the entire microchannel.

The same focusing experiments were performed with both model analytes diluted with 20mM phosphate buffer, but stable focusing was not achieved. The temperature-dependent mobility curve in Figure 2.3(b) shows that focusing should be possible with this buffer as long as a sufficient temperature profile can be reached. However, the conductivity of the phosphate buffer is around 3 times that of the 900mM Tris-Borate buffer at room temperature, and increases 1.5 times faster with temperature (empirical results). The higher conductivity creates "thermal runaway" control problems in achieving a stable temperature profile by Joule heating. This condition led to rapid boiling in the microchannel and hindered all focusing attempts. When a lower voltage was applied to prevent boiling, an insufficient temperature profile resulted and focusing was not possible.

An interesting phenomenon occurring during the focusing process was that the focused sample plug slowly moved toward the anode side and finally disappeared from the viewing area. One possible explanation is that because a steady-state temperature profile is difficult to achieve, the temperature may be continually increasing in this region and the electrophoretic mobility of the sample analyte may be dominant over the bulk flow, as seen in Figure 2.3(a). The location where the net velocity of the analyte reaches

zero moves away from the horizontal center of the microchannel because the temperature of the sample solution keeps increasing due to the continuous electric current.

The temperature gradient in the system is generated via Joule heating through varying channel geometry and the temperature within the microchannel keeps increasing until the electric field is removed or the sample solution boils. To prevent the sample solution from boiling and migration of the focused sample plug, the current flowing through the microchannel was manually controlled by changing the applied electric potential. When the sample analyte started to focus, the voltage was lowered to keep the current magnitude stable and the focused sample plug remained idle. However, if the voltage is lowered too much, the temperature gradient is not sufficient to achieve zero net velocity and the focused sample plug moves toward the cathode side due to higher electroosmotic flow. The sample plug movement is very sensitive to the current intensity (*i.e.* the temperature variation); thus proper current control is required for well-maintained sample focusing.

The focusing of a mixture of two analytes was performed to show the separation capability of the temperature gradient via Joule heating. Two analytes (25µM fluorescein-Na and 100nM FITC-BSA) were concurrently focused at the same location for 5 minutes by 1200V of electric potential (Figure 2.8 (a) and (b)), and subsequently separated due to the mobility difference for t > 5 minutes (Figure 2.8 (a) and (c)). Because of the difficulty in achieving a steady-state temperature profile, the temperature along the channel continually increases due to the constant electric field. As evident in Figure 2.3(a), electrophoresis begins to dominate at higher temperatures and thus the species begin to drift toward the anode. During this separation process, the two focused plugs slowly migrate toward the anode side at different rates due to the dissimilar electrophoretic mobilities of the analytes, and the separation distance between the two plugs increased. The movement of the analytes lessens the concentration of the focused plugs due to the increasing channel width and diffusion, but enhances the separation of the two species. The increasing distance between two plugs may also be caused by the widening channel, which reduces the electroosmotic flow opposing the electrophoretic movement of negatively charged molecules.
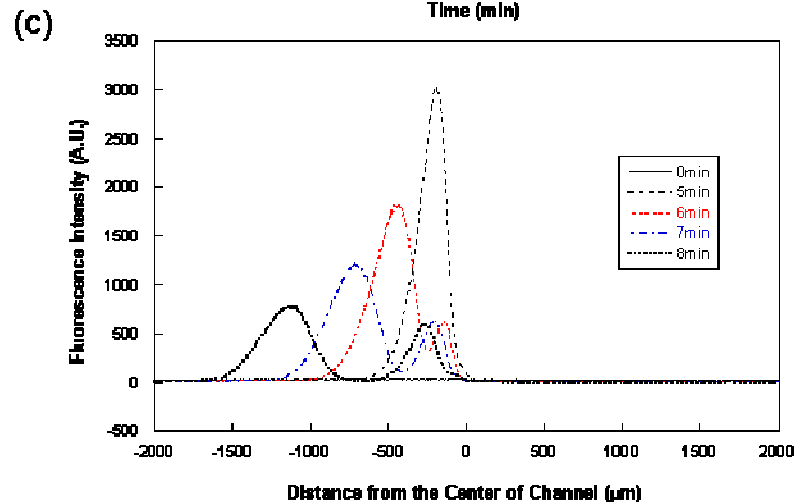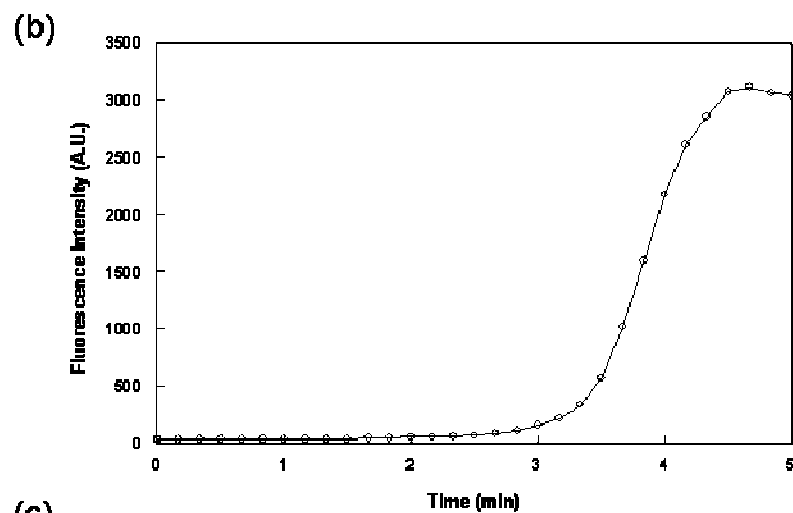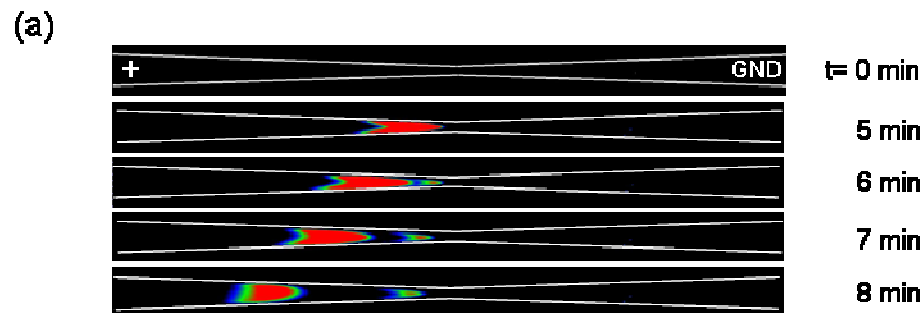
Figure 2.8. Time sequence images and fluorescence intensity profiles during separation of a mixture of 25μM fluorescein-Na and 100nM FITC-BSA in 900mM Tris-Borate buffer due to applied 1200V electric potential. (a) Time sequence images show the separation of the two species over time. Both species were focused at the same area until t = 5 minutes, and subsequently separated due to the mobility difference for t > 5 minutes. (b) Plot shows the fluorescence intensity during concurrent focusing of fluorescein and FITC-BSA. (c) Plot shows the fluorescence intensity variations following the centerline of the microchannel over time.

23

Perhaps a more powerful method of species separation using this device involves coupling species preconcentration with a subsequent electrophoretic separation along the same channel, as shown in Figure 2.9. Note that more difficult protein-protein separations were not performed in this device due to the short length of the channel. However, this concentration technique should be able to be coupled to almost any length separation system.
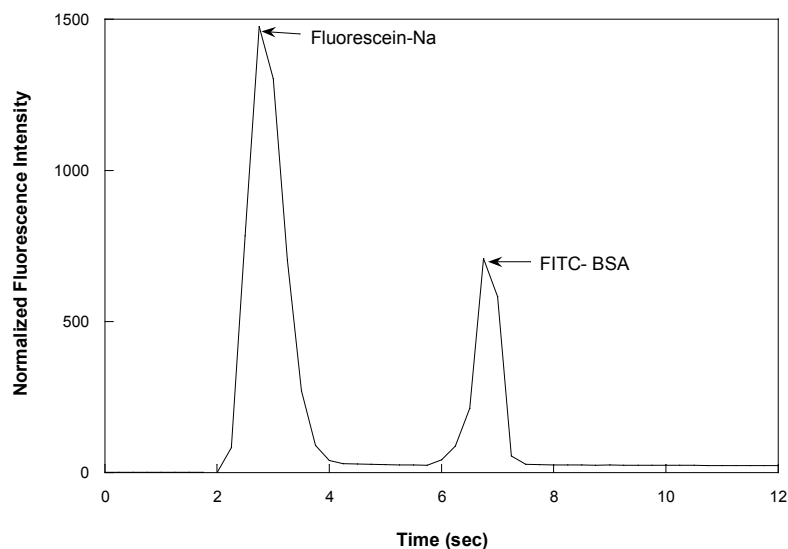
Figure 2.9. Electropherogram showing separation of 25μM fluorescein-Na and 0.25μM FITC-BSA following preconcentration in same microchannel. Samples were focused at inlet to center region for 5 minutes, as before. The electric field was removed for 5 seconds to allow the channel to cool and the focused plug to drift into the cathode side of the microchannel. An electric potential of 600V was then applied to carry the species toward the cathode, initiating species separation. Fluorescence intensity was measured at a location ~1.4mm right of the microchannel center.

Temperature importance and TGF with more common buffers

The dominant factor governing the focusing and separation of analytes is the temperature gradient within the microchannel caused by Joule heating due to the electric field. To validate the temperature effect on the focusing mechanism, an experimental setup incorporating thermoelectric heat sinks was developed as shown in Figure 2.10(a). At first, the heat sinks were used to heat the sample solution within the microchannel. Figure 2.10(b) shows the profile of the current and the fluorescence intensity of the 0.1mM fluorescein-Na. Focusing of the sample was not achieved by simply applying an 1100V electric potential for 3 minutes and the current remained quite stable, implying

24

that there is little temperature increase. Sample focusing began after applying external heating (~45°C) for t > 3 minutes with constant 1100V electric potential still applied to the microchannel. The solution in the microchannel began boiling when the temperature reached the boiling point (~100°C) and the focused plug abruptly disappeared. Sample focusing did not occur during the same time frame with only the 1100V electric potential, as the dash-dot line shows in Figure 2.10(b). The electric potential alone is not enough to form the temperature gradient in the microchannel needed to obtain sample focusing.

Next, a similar experiment was performed using the thermoelectric heat sinks to cool the microdevice. Sample focusing was achieved by applying a 1600V electric potential, but the focused sample plug disappeared when external cooling (~10°C) was applied (in Figure 2.10(c)). The sample was focused again after the external cooling was turned off and the focusing disappeared again due to external cooling.
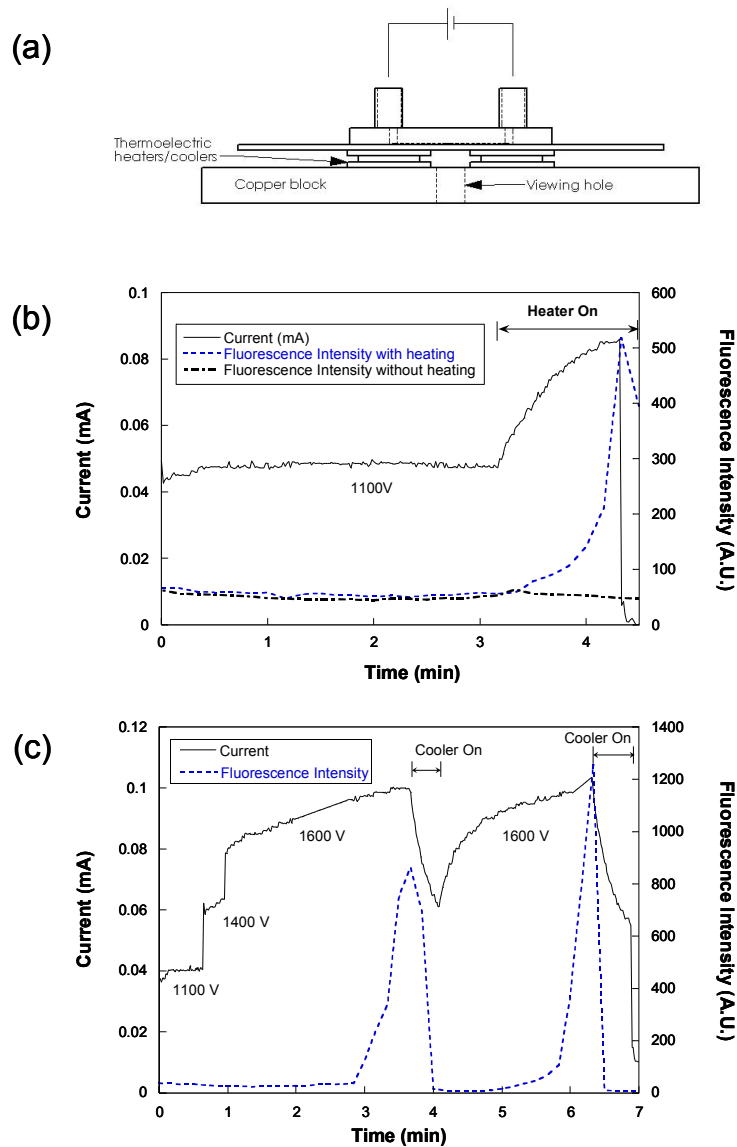
Figure 2.10. Focusing of 0.1mM fluorescein-Na in 900mM Tris-Borate buffer using combination of Joule heating and external heating/cooling. (a) Schematic drawing showing the system composed of a copper block, two thermoelectric heat sinks and the experimental microdevice from Figure 2.1. (b) Focusing of the sample was not achieved by simply applying an 1100V electric potential for 3 minutes. Sample focusing began after applying external heating for t > 3 minutes with constant 1100V electric potential. The solution in the microchannel began boiling when the temperature reached the critical value and the corresponding fluorescence intensity abruptly dropped. The dash-dot line shows the fluorescence intensity profile when only 1100V electric potential is applied to the channel with no external heating/cooling. (c) Sample focusing was achieved by applying a 1600V electric potential, but the focused sample plug disappeared when external cooling was applied. The sample was focused again after the external cooler was turned off and the focusing disappeared again due to external cooling.

Focusing experiments were attempted again with fluorescein-Na diluted in 20mM phosphate buffer using the combined Joule heating and external heater system. The external heater was used to increase the base temperature up to 40°C and the applied potential to the microchannel was ramped up from 250V to 600V over 10 minutes. >10-fold focusing of sample analyte was achieved after 10 minutes; a sample focusing image is shown in Figure 2.11. In a combined Joule heating and external heater system, a steady-state temperature profile can be more readily achieved in a microchannel compared to a system only using Joule heating. The external heater elevates the base temperature of the microchannel, thus reducing the Joule heating, or electric potential, needed for focusing of analytes. Due to the low electric potential required for achieving the necessary temperature, the temperature profile can be more stable than a system without the external heater, and higher conductivity buffer solutions can be employed for TGF. The focused plug, however, drifted toward the left side of the channel slowly after focusing in the middle. Further study is needed to resolve this drifting problem in the phosphate buffer system, as the cause of this drift is still unclear.
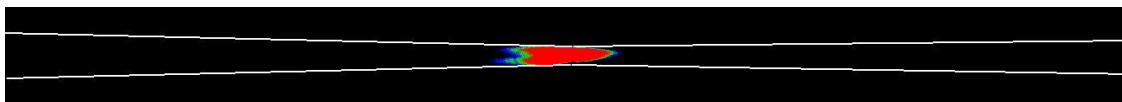
Figure 2.11. Image shows focusing of 25µM fluorescein-Na in 20mM phosphate buffer using a combined Joule heating and external heater system. The base temperature via external heating is ~ 40°C and the applied potential to the microchannel was ramped up from 250V to 600V over 10 minutes. However, the focused plug drifted to the left side of the channel slowly after focusing at the middle of channel.

Conclusions

This chapter presented an analysis of temperature-dependent transport behavior along a microchannel, and the theory was used to develop a simple TGF device exploiting an inherent Joule heating effect. A variable-width PDMS device delivers rapid and repeatable focusing of model analytes using relatively low-power compared to current TGF approaches. However, maintaining a steady-state temperature profile with this system was difficult due to the thermal runaway induced by the increasing buffer conductivity with temperature. This effect led to difficulty in achieving a stable and maintained concentration, elucidating the need for a more controlled system.

The combined Joule heating with external heating/cooling experiments strongly suggests that temperature indeed is the dominant factor in achieving focusing. Future work will involve employing that technique to focus molecules in systems otherwise thought impossible. For instance, it was showed that the 900mM Tris-Borate buffer is more conducive to TGF than the 20mM phosphate buffer because it is less conductive yet yields steeper $\frac{\partial \mu_{net}}{\partial T}$ curves. However, the combined system device may allow for better focusing using the 20mM phosphate buffer as it can more precisely control temperature and prevent thermal runaway commonly seen.

The device was used to concentrate and separate two species in solution, 25 μM fluorescein-Na and 100nM FITC-BSA, in less than 10 minutes. Future research will include using the technique to achieve more interesting separations, such as an on-line immunoassay. We recognize that the high temperatures currently used to achieve focusing will most likely be harmful to more sensitive biomolecules, but we are optimistic that a future design will yield non-destructive separations using this simple, repeatable technique.

CHAPTER 3

THEORETICAL AND NUMERICAL ANALYSIS OF TEMPERATURE GRADIENT FOCUSING VIA JOULE HEATING

Introduction

Microchip-based electrokinetic sample preconcentration and separation mechanisms have been extensively studied and developed over the past decade, especially in the field of analytical chemistry. Sample preconcentration is a critical operation generally required for the determination of trace amounts of compounds of interest for which the concentration in the original solution does not meet the detection limits of the instrumentation [4, 6-8, 34]. This is even more important in the case of microfluidic chip-related applications given the very small volumes of samples that can be handled within the microchip [35]. Several electrokinetic field gradient focusing techniques enabling sample analyte concentration during separation have been developed for on-chip proteomic analyses, including isoelectric focusing [36], electric field gradient focusing [11, 17, 37, 38], and isotachophoresis [9].

Temperature gradient focusing (TGF) [18-20, 39] has emerged as an effective and reliable method for analytical species concentration and separation. TGF achieves focusing by balancing the bulk flow in a channel against the electrophoretic migrative flux of an analyte along a controlled temperature profile. The temperature dependence of a sample's electrophoretic velocity, due to the temperature dependence of the buffer's ionic strength and viscosity, allows for focusing at a unique location along the channel.

Chapter 2 showed that TGF could be accomplished using a simple variable-width channel to induce a temperature gradient. An applied electric field generates Joule heating along the channel, and the higher current density produces a

higher temperature in the narrower region. The same electric field is used to invoke bulk electroosmotic flow and migrative drift of the sample. The device, shown schematically in Figure 2.1, was used to achieve rapid, repeatable concentration and separation of analytes using significantly less power than systems requiring external heating and cooling of the channel, thus allowing for simpler incorporation into multi-component systems.

Despite the demonstrated experimental success of TGF, a thorough theoretical analysis is still needed for systemic design and implementation into lab-on-a-chip devices. TGF has certain limitations, including specific buffer requirements and limited resolution, which can be addressed and better understood through numerical simulation. In addition, although the extremely low-power consumption of Joule heating is attractive, runaway heating can occur, and so a fundamental heat transfer analysis is needed both to implement and control such a system. Several prior groups have presented numerical studies of Joule heating and its effects on electrokinetic transport and separations [40-47]. Those efforts provide a framework for applying numerical techniques to the highly nonlinear Joule heating problem.

This analysis will expand upon the previous work and delve deeper into the theory driving TGF. The governing equations needed to fully depict the electrokinetic transport phenomena along a variable-width microchannel will be provided. Those equations will then be implemented into a quasi-1D code, along with empirical data for various temperature-dependent parameters to predict thermal behavior in the channel, focusing locations, focusing rates, and sample band widths. Comparison with experiment is conducted to verify the validity of the numerical code. In addition to this computational tool, the aim is to provide rule-of-thumb methodology for device design and accelerate TGF's adoption as a viable analytical technique.

While the current concern is the systemic design and analysis of a TGF device, this analysis also provides a generalized fundamental model of temperature-dependent electrokinetic transport. In particular, a simple quasi-1D energy analysis is presented that accurately depicts the transient temperature behavior due to Joule heating seen in on-chip microchannels. The governing equations and model presented here can be used to analyze electrokinetic phenomena in many lab-on-a-chip systems.

Theory

In TGF, the bulk fluid velocity, u_{bulk}, arising from electroosmotic flow (EOF) and/or pressure driven flow (PDF) opposes the electrophoretic drift velocity, u_{ep}, of an analyte. Because u_{ep} is a function of temperature, T, and T varies with x, a coordinate along the length of the channel, the net velocity, $u_{net} = u_{bulk} + u_{ep}$, can be manipulated to achieve focusing at a specific location along a channel if $u_{net} = 0$ and $\frac{\partial u_{net}}{\partial x} < 0$. Sample will deplete from the location if $u_{net} = 0$ and $\frac{\partial u_{net}}{\partial x} > 0$. The following derivation will yield the quasi-1D equations needed to depict the transport phenomena of a species along a temperature gradient.

Mass conservation

To describe the motion of the analytes, the conservation of mass equation for the bulk fluid is given as:

$$\frac{\partial}{\partial x}\left(u_{bulk} A\right) = 0 \tag{3.1}$$

where A is the cross-sectional area of the channel. Note that u_{bulk} represents the mass-averaged velocity of all species; in the quasi-1D formulation used here, we ignore the variation of velocity across the channel cross-section.

Equation of bulk fluid motion

The bulk fluid velocity at any location i in the channel is composed of the sum of the velocities due to both PDF and EOF:

$$u_{bulk,i} = u_{eof,i} + u_{pdf,i}$$

$$u_{bulk,i} = \left(\frac{\varepsilon_0 \varepsilon_i(T)\zeta_i(T)}{\eta_i(T)}\right)\frac{d\phi_i}{dx} - \left(\frac{1}{32}\frac{d_{h,i}^2}{\eta_i(T)}\right)\frac{dP_i}{dx} \tag{3.2}$$

where ε_0 is the permittivity of a vacuum ($8.854 \times 10^{-12}\frac{C^2}{Nm^2}$), $\varepsilon(T)$ is the temperature-dependent dielectric constant of the electrolyte, $\zeta(T)$ is the zeta potential, $\eta(T)$ is the

buffer viscosity, ϕ is the electric potential, d_h is the channel's hydraulic diameter

($d_h = \dfrac{4A}{Perimeter}$), and P is the fluid pressure at location i along the channel. The

term $\left(\dfrac{\varepsilon_0 \varepsilon_i(T) \zeta_i(T)}{\eta_i(T)} \right)$ is known as the electroosmotic mobility, $\mu_{eof}(T)$, of the fluid. We

note that the second term in the RHS is an approximation for channels with cross-sections
of modest aspect ratios (width/height). While this approximation has the obvious flaw of
not matching the experiment exactly, it has the merit of capturing all the essential physics
with a consistent and simple model that is at most a factor of 2 off in terms of the
hydraulic permeability of the channel at any point along its length.

Molecular mass transport equation

The concentration, c, of a charged species at any point i in the channel will
depend on the gradient of the species flux, j, due to diffusion, bulk convection, and
electrophoresis, as well as the reaction rate of the species in the channel. Conservation of
species can be expressed as equation (3.3), with the flux, j, defined using the convection-
diffusion equation (3.4).

$$A_i \frac{\partial c_i}{\partial t} + \frac{\partial}{\partial x}(A_i j_i) = A_i \omega_i \tag{3.3}$$

$$j_i = -D_{eff,i}(T) \frac{\partial c_i}{\partial x} + c_i u_{bulk,i} - c_i \mu_{ep,i}(T) \frac{d\phi_i}{dx} \tag{3.4}$$

where ω is the species reaction rate, and $\mu_{ep}(T)$ is the electrophoretic mobility of analyte.
$D_{eff}(T)$ is the effective dispersion coefficient of the solute given by the following
approximation [48]:

$$D_{eff}(T) = D(T)\left[1 + \frac{Pe_h^2}{210} \right] \tag{3.5}$$

where Pe_h is the Peclét number based on the height, d, of the channel, $Pe_h = \dfrac{ud}{D(T)}$. The

temperature-dependent mass diffusivity of the analyte, $D(T)$, is given by

$$D(T) = 0.025 D_0 (T - 25°C) + D_0 \tag{3.6}$$

where D_0 is the diffusion coefficient of analyte at room temperature [41, 49]. Note that equation (3.5) is an approximation for flow between two flat plates, and equation (3.6) linearizes the diffusion coefficient's dependence on viscosity. While these expressions introduce a small amount of error into the model, they do provide a simple approximation for the analyte dispersive behavior and will only slightly affect the predicted amplitude or width of an experimentally focused band.

With the reaction rate set to zero (assuming inert species):

$$A_i \frac{\partial c_i}{\partial t} = -\frac{\partial}{\partial x}(A_i j_i) = \frac{\partial}{\partial x}\left(A_i D_{eff,i}(T)\frac{dc_i}{dx}\right) - \frac{\partial}{\partial x}\left(c_i A_i u_{bulk,i}\right) + \frac{\partial}{\partial x}\left(c_i A_i \mu_{ep,i}(T)\frac{\partial \phi_i}{\partial x}\right) \quad (3.7)$$

$$A_i \frac{\partial c_i}{\partial t} = -\frac{\partial}{\partial x}\left[A_i\left(u_{bulk,i} c_i + u_{ep,i} c_i\right)\right] \quad (3.8)$$

Simplifying this equation using the continuity condition in equation (3.1):

$$A_i\left[\frac{\partial c_i}{\partial t} + (u_{bulk,i} + u_{ep,i})\frac{\partial c_i}{\partial x}\right] = -c_i \frac{\partial}{\partial x}\left(A_i u_{ep,i}\right) \quad (3.9)$$

At steady state, $\frac{\partial c_i}{\partial t} = 0$, and the resulting differential equation can be solved to yield:

$$\frac{c_{x=x1}}{c_{x=x0}} = \frac{\left(u_{bulk,x0} + u_{ep,x0}\right)A_{x0}}{\left(u_{bulk,x1} + u_{ep,x1}\right)A_{x1}} \quad (3.10)$$

(This is actually easier to derive using equations (3.1) and (3.2), setting reaction, diffusion, and unsteady terms to zero). Thus if there were no diffusion, the concentration at steady state would be infinite at locations where the net velocity is zero. Although this is a contrived solution, this analysis does tell us the location where (or condition under which) concentration of analytes occurs.

A second interesting solution gives the initial rate of sample concentration increase at the concentration spot. In equation (3.7), assuming concentration is locally constant (initially uniformly distributed) and the area locally constant (ignore gradual area variation), one finds that $\ln(c/c_o) = (\partial u_{ep}/\partial x)t$. This means that an initially exponentially-increasing concentration in time is expected, and that the stronger the gradient in the velocity (or temperature), the higher the initial concentration rate. However, this rate will quickly slow to a rate limited by advective transport, so it is not necessarily true that steeper gradients will speed the process if large concentration factors

are desired. Also note that the concentration factor, c/c_o, is independent of the initial concentration with the assumptions used in this model.

Finally, to complete the above equations, an approximation to the temperature dependence of an analyte's electrophoretic mobility is needed. When possible this dependence should be measured experimentally, as shown previously. However, if empirical determination is difficult or a quick estimation is desired, the electrophoretic mobility for a globular protein molecule can be approximated using the equation,

$$\mu_{ep} = \frac{q}{6\pi r \eta(T)} \tag{3.11}$$

where q is the net charge at a given pH, and r is the "effective" radius of the protein [50].

Electrostatics

Assuming an electrostatic condition, the current induced by the applied electric potential is constant along the channel (but may vary slowly in time) and can be written as:

$$I = \sigma(T)AE = -\sigma(T)A\frac{d\phi}{dx} \tag{3.12}$$

where $\sigma(T)$ is the temperature-dependent electrical conductivity of electrolyte. The Joule heating-induced temperature gradient causes a spatial distribution of both the buffer and analyte electrical conductivity.

Energy equation

A schematic of the assumed cross-sectional heat transfer phenomena in the device is shown in Figure 3.1.
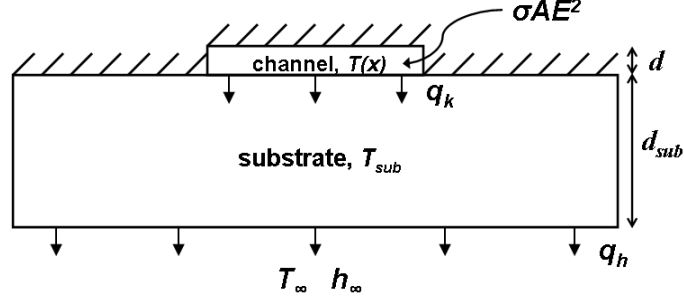
Figure 3.1. Axial schematic showing heat transfer approximations used in thermal analysis. The approximate thickness of the glass substrate is 1mm, and that of the PDMS slab is 3mm.

The temperature at any point along the microchannel due to Joule heating can be approximated using the 1-D transient energy equation, coupled with a *"zero-dimensional"* energy equation for the glass substrate [51]:

$$\frac{\partial}{\partial t}\left(\rho_i c_{p,i} A_i T_i\right) + u_{bulk} \cdot \frac{\partial}{\partial x}\left(\rho_i c_{p,i} A_i T_i\right) = \frac{\partial}{\partial x}\left(k_i A_i \frac{\partial T_i}{\partial x}\right) + \sigma_i A_i \left(\frac{\partial \phi_i}{\partial x}\right)^2 - \frac{2 k_{sub} w_i}{l}(T_i - T_{sub}) \quad (3.13)$$

$$\frac{2 k_{sub} w_i}{l}(T_i - T_{sub}) - h_\infty w_{sub}(T_{sub} - T_\infty) = \rho_{sub} c_{p,sub} w_{sub} d_{sub} \frac{\partial T_{sub}}{\partial t} \quad (3.14)$$

where ρ is the buffer density, c_p is the buffer specific heat, k is the buffer thermal conductivity, k_{sub} is the substrate thermal conductivity, w is the channel half-width in contact with the substrate, l is a length scale characteristic of the distance between the centers of the channel and the substrate, w_{sub} the width of the solid substrate, T_{sub} is the temperature of the substrate, h_∞ is the external convective heat transfer coefficient of the air surrounding the substrate, T_∞ is the external temperature, ρ_{sub} is the substrate density, $c_{p,sub}$ is the substrate specific heat, and d_{sub} is the depth of the substrate. The idea behind these two coupled equations is quite straightforward. Equation (3.13) is simply conservation of energy for the fluid in the channel with the terms in the RHS accounting for axial diffusion, energy input via Joule heating, and heat loss via conduction to the glass substrate, respectively. Equation (3.14) is conservation of energy for the substrate. The LHS accounts for heat flux into the substrate from the fluid and heat loss to the surrounding air; the RHS accounts for storage of energy in the substrate.

Using this analysis it is assumed that all heat transfer occurs through the glass substrate (due to its relatively low thermal conductivity and vast size, the PDMS slab is

35

assumed to be completely insulating.) A quick calculation of the Biot number for the vertical heat conduction through the glass substrate shows that $Bi_{sub} = \dfrac{h_\infty d_{sub}}{k_{sub}} \ll 0.1$, meaning we can neglect any vertical temperature gradient in the glass. A similar analysis on the channel side of the glass substrate reveals that $\dfrac{4wL}{w_{sub}l} \ll 0.1$, further supporting the lumped substrate temperature approximation. Furthermore, due to the significantly higher thermal conductivity in the glass than the buffer, we assume that the entire substrate has the same temperature (T_{sub} has no spatial dependence).

It is important to note that by coupling the energy analysis of the substrate to that of the channel, we can more accurately depict the thermal behavior of the channel than with a simple 1-D analysis. More specifically, we can capture the two timescales associated with heating the channel fluid. Due to its small scale, the fluid will initially experience a very rapid heating, followed by a slower heat rate limited by the parallel thermal capacitance of the glass substrate.

Equations (3.13) and (3.14) can be simplified and solved analytically to better illustrate the concept of two thermal timescales. The following assumptions were used in simplifying the coupled equations: 1) u_{bulk} and k are neglected, 2) σ, ρ, and c_p are constant with temperature, 3) I is a linear function of time, t, with a negligible $\dfrac{dI}{dt}$, and 4) the time constant of T_{sub} is independent of the temperature difference between the channel and substrate. Using these assumptions the substrate temperature is approximated by:

$$T_{sub}(t) = T_\infty + \frac{I^2(t)}{h_\infty A_{sub}\sigma d} \int_{x=0}^{L/2} \frac{1}{w(x)}\left(1 - e^{-\frac{h_\infty A_{sub}}{m_{sub}c_{p,sub}}t}\right)dx \qquad (3.15)$$

where $A_{sub} = w_{sub}L$, d is the depth of the microchannel, and $m_{sub} = \rho_{sub}w_{sub}d_{sub}L$. Using equation (3.15), the temperature of the channel fluid can then be solved as:

$$T(x,t) = Ae^{-\frac{k_{sub}}{dl\rho c_p}t} + Be^{-\frac{h_\infty A_{sub}}{m_{sub}c_{p,sub}}t} + C \qquad (3.16)$$

where A, B, and C are defined as:

$$B = \dfrac{\dfrac{k_{sub}I^2(t)}{l\rho c_p h_\infty A_{sub}\sigma d^2} \displaystyle\int_{x=0}^{L/2} \dfrac{1}{w(x)}\,dx}{\dfrac{h_\infty A_{sub}}{m_{sub}c_{p,sub}} - \dfrac{k_{sub}}{dl\rho c_p}}$$

$$C = \dfrac{I^2(t)}{h_\infty A_{sub}\sigma d} \int_{x=0}^{L/2} \dfrac{1}{w(x)}\,dx + T_\infty + \dfrac{I^2(t)l}{4k_{sub}\sigma w^2(x)d} \qquad (3.17)$$

$$A = T_\infty - B - C$$

Numerical simulation

A 1-D code was developed to numerically approximate the transient temperature profile and subsequent fluidic and molecular transport of an analyte/buffer solution along a microchannel of a given geometrical design. This model can be used in the design of a TGF device once the temperature dependent parameters of a species and buffer system are assumed or experimentally determined. The code was developed using Matlab (Mathworks, Natick, MA). The following assumptions were used in formulating the model: 1) The ends of the channel are an infinite reservoir of buffer/analyte compared to the channel volume, 2) The concentration of analyte molecules is negligible compared to the concentration of buffer ions in solution, 3) The system is electrostatic, and (d) Buffer pH is constant.

Equations (3.1), (3.2), (3.7), (3.12), (3.13) and (3.14) were used as the governing equations of the model and discretized along x. The temperature and species concentration at each point were calculated using a Crank-Nicolson scheme to solve equations (3.7) and (3.13) at each time increment. Briefly, the Crank-Nicolson scheme is an implicit, second-order accurate, finite difference method that is inherently stable. Following discretization the method results in a tri-diagonal system of linear equations to be solved at each time step. The time increments based on the stability recommendation for solving the mass transport equation were calculated as:

$$dt \leq \frac{N(dx)^2}{2D_{eff,max}} \qquad (3.18)$$

where N is the number of nodal coordinates and dx is the nodal spacing. A moving average of both the T and c values was computed after each time step to reduce oscillations in the solutions. Values of temperature-dependent parameters were updated after each time step. The simulations were conducted using a graphical user interface (GUI) for simple parameter adjustment and visualization. Further details of the formulation scheme used can be found in Appendix 1.

The following initial conditions and boundary conditions were implemented into the code:

At $t = 0$: $c(x) = c_0$, $T(x) = T_0$

At $x = 0$: $\left.\frac{\partial c}{\partial x}\right|_{x=0} = 0$, $\phi_{x=0} = prescribed$, $P_{x=0} = 0$, $T_{x=0} = T_0$,

At $x = L$: $\left.\frac{\partial c}{\partial x}\right|_{x=L} = 0$, $\phi_{x=L} = grounded$, $P_{x=L} = 0$, $T_{x=L} = T_0$,

To evaluate the validity of the numerical formulation, simulations of pure diffusion were calculated and compared with analytical solutions. Equation (3.7), assuming constant $A(x)$ and $u_{ep} = u_{bulk} = 0$, simplifies to the basic 1-D diffusion equation:

$$\frac{\partial c}{\partial t} = D\frac{\partial^2 c}{\partial x^2} \qquad (3.19)$$

This equation, assuming Neumann boundary conditions, can be solved to yield:

$$c = \sum_{n=1}^{\infty} B_n e^{\left(-\left(\frac{n\pi}{L}\right)^2 Dt\right)} \cos\left(\frac{n\pi}{L}x\right) + B_o \qquad (3.20)$$

$$B_o = \frac{1}{L}\int_0^L c(x)dx \qquad (3.21)$$

$$B_n = \frac{2}{L}\int_0^L f(x)\cos\left(\frac{n\pi}{L}x\right)dx \qquad (3.22)$$

where $f(x)$ is the initial concentration condition.

Experimental

Procedural and equipment details regarding the results presented here can be found in Chapter 2.

Materials

Fluorescein-Na and fluorescein isothiocyanate conjugate bovine serum albumin (FITC-BSA) (Sigma-Aldrich, St. Louis, MO) were used for temperature-dependent mobility, focusing, and separation experiments. 900mM Tris-Borate buffer (900mM Tris, 900mM Boric acid, pH 8.0) and phosphate buffer (dibasic sodium phosphate, 20mM, pH 7.2) were used for the buffer systems. Each sample analyte was diluted with the buffer solution at several concentrations (100nM, 25μM and 0.1mM). Rhodamine B dye (Molecular Probes, Carlsbad, CA) diluted with 900mM Tris-Borate buffer was used to measure the temperature distribution in the microchannel using a fluorescent intensity technique previously described by Ross et al [26]. The protein samples were kept in a freezer to prevent deterioration and treated following the manufacturer's instruction. All liquid samples were filtered with a 0.1 μm syringe filter (Whatman, Maidstone, UK) to prevent channel clogging by particulates.

Temperature-dependent parameters measurement

The temperature-dependent viscosity, $\eta(T)$, and electrical conductivity, $\sigma(T)$, of each buffer solution were measured to be used as buffer properties for numerical simulations. $\eta(T)$ was measured using a Cannon-Fenske routine viscometer (Cannon Instrument, State College, PA). The viscometer was heated using a thermostated water bath over a hot plate. $\sigma(T)$ was measured using a conductivity meter (Oakton CON510, Vernon Hills, IL) with the sample buffer being held in a thermal bath. Each parameter was measured in the range of 25°C - 80°C.

The electrophoretic mobility, $\mu_{ep}(T)$, of 0.1mM fluorescein-Na in both 900mM Tris-Borate buffer and 20mM phosphate buffer was measured using a photobleached dye imaging method similar to techniques previously described [27-29].

Results and Discussion

The numerical simulation presented in this work uses empirical approximations for several transport parameters. Table 3.1 lists the empirical approximations used in the code for modeling the transport of both fluorescein-Na and FITC-BSA in 900mM Tris-Borate buffer and 20mM phosphate buffer, some taken from literature and others evaluated in our lab.

Table 3.1. Summary of empirical approximations used in modeling transport in channel containing fluorescein-Na and FITC-BSA in 900mM Tris-Borate buffer and 20mM phosphate buffer (temperature values in ºC)

Parameter	Value	Source
ε	$305.7 \times \exp[-(T+273)/219]$	Knox [52]
$\zeta(T)$	$\zeta_0 + 0.003\zeta_0(T - T_0)$ V , T_0=room temperature	Evenhuis et al. [53]
ζ_0	45mV *(900mM Tris-Borate buffer)* 10mV *(20mM phosphate buffer)*	Kirby et al. [54]
D_0	0.64×10^{-9} m$^2 \cdot$s^{-1} *(Fluorescein-Na)* 8.0×10^{-11} m$^2 \cdot$s^{-1} *(FITC-BSA)*	Galambos [55] Krouglova et al. [56]
$\eta(T)$	$1.84 \times 10^{-3} \times \exp(-1.76 \times 10^{-2} \times T)$ N$\cdot$s$\cdot$m^{-2} *(900mM Tris-Borate buffer)* $1.39 \times 10^{-3} \times \exp(-1.81 \times 10^{-2} \times T)$ N$\cdot$s$\cdot$m^{-2} *(20mM phosphate buffer)*	Measured in laboratory
$\sigma(T)$	$6.06 \times 10^{-3} \times T + 4.33 \times 10^{-2}$ S$\cdot$m^{-1} *(900mM Tris-Borate buffer)* $9.71 \times 10^{-3} \times T + 0.405$ S$\cdot$m^{-1} *(20mM phosphate buffer)*	
$\mu_{ep}(T)$	$-4.394 \times 10^{-14} \times T^2 - 8.024 \times 10^{-10} \times T + 8.621 \times 10^{-9}$ m$^2 \cdot$V$^{-1} \cdot$s^{-1} *(0.1mM Fluorescein-Na in 900mM Tris-Borate buffer)* $4.900 \times 10^{-13} \times T^2 - 2.944 \times 10^{-10} \times T + 4.660 \times 10^{-9}$ m$^2 \cdot$V$^{-1} \cdot$s^{-1} *(0.1mM Fluorescein-Na in 20mM phosphate buffer)*	
h_∞	20 Wm$^{-2} \cdot$ºC^{-1}	Incropera [51]
ρ	$-5.992 \times 10^{-3} \times T^2 + 2.929 \times 10^{-2} \times T + 999.9$ kg$\cdot$m^{-2} *(water)*	
c_p	$-1.786 \times T + 4206$ J$\cdot$kg$^{-1} \cdot$ ºC^{-1} *(water)*	
k	$1.331 \times 10^{-3} \times T + 0.574$ W$\cdot$m$^{-1} \cdot$ºC^{-1} *(water)*	
ρ_{sub}	2500 kg$\cdot$m^{-2} *(glass)*	
$c_{p,sub}$	750 J$\cdot$kg$^{-1} \cdot$ ºC^{-1} *(glass)*	
$k_{,sub}$	1.4 W$\cdot$m$^{-1} \cdot$ºC^{-1} *(glass)*	

The validity of the numerical formulation was tested by simulating pure diffusion of a plug of sample and comparing the numerical result with the analytical solution, equations (3.20)-(3.22). Results are displayed in Figure 3.2 showing the maximum error between the concentration profiles predicted with the two solutions is approximately 0.4%.
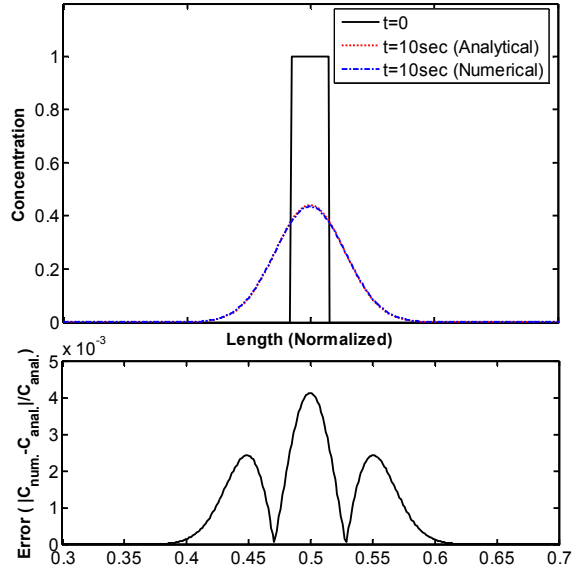
Figure 3.2. Comparison between numerical and analytical solutions for case of pure species diffusion Top: Concentration profile for $t = 0$ and $t = 10$sec. (solid line: initial concentration, dotted line: analytical solution at 10sec, and dashed-dot line: numerical solution at 10sec). Bottom: Error of numerical solution. Error is defined as

$$Error = \frac{C_{num} - C_{anal}}{C_{anal}}.$$

Sample plots showing the resulting transport behavior for a simulation of 0.1mM fluorecein-Na in 900mM Tris-Borate under 1200V for 1 minute are shown below in Figure 3.3.
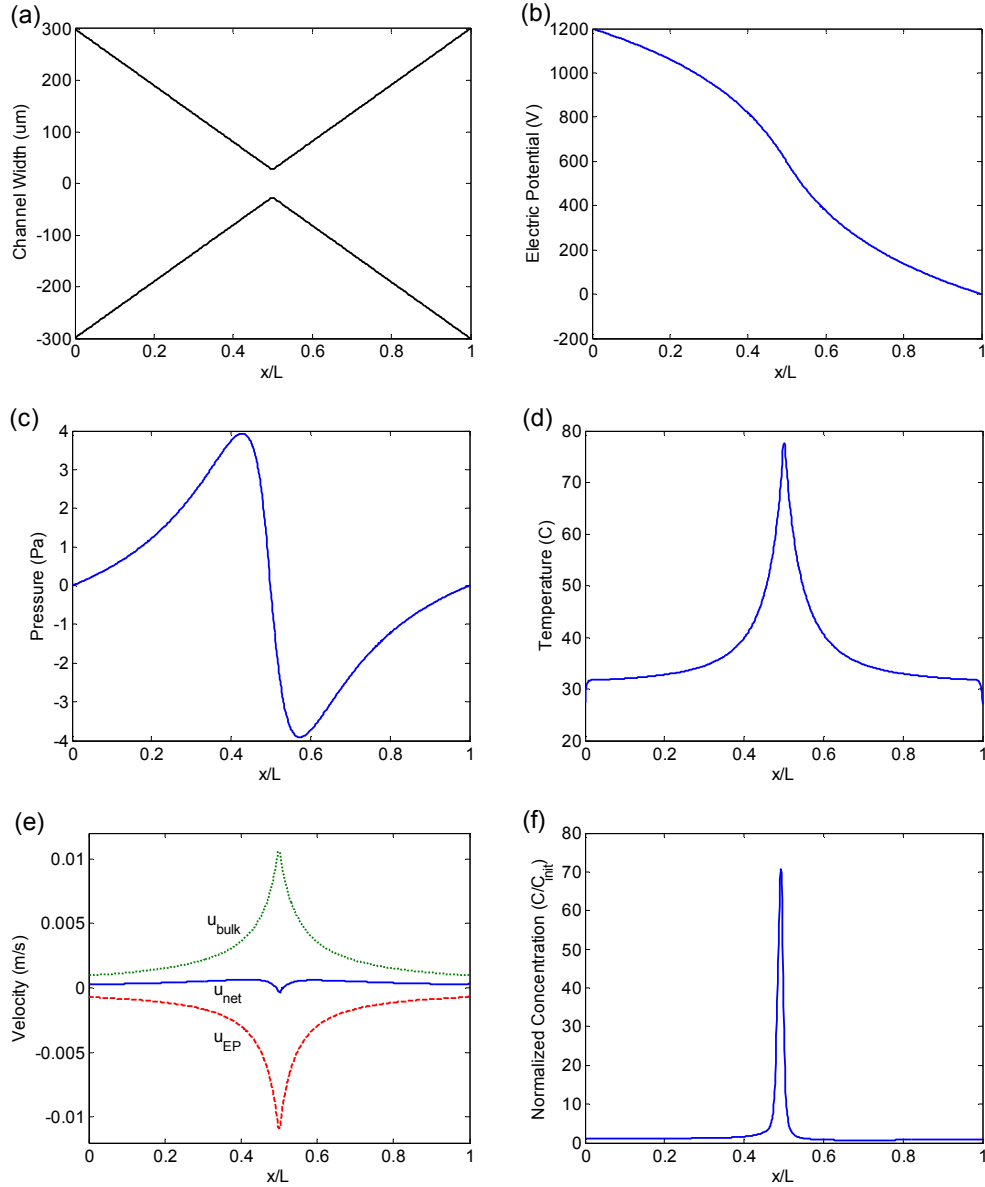
Figure 3.3. Numerical simulation of transport phenomena along analog microchannel after 1 minute of focusing. 0.1mM fluorescein-Na in 900mM Tris-Borate buffer is simulated. (a) Geometrical profile of microchannel (L = 16mm, d = 18μm). (b) Electric potential profile: 1200V applied at x = 0, $x=L$ grounded. (c) Pressure profile: $P = 0$ assumed at both ends. (d) Temperature profile due to Joule heating: $T = 25$ºC assumed at both ends. (e) Resulting velocity profiles of: bulk fluid, $u_{bulk} = u_{eof} + u_{pdf}$ (dashed line), u_{ep} (dashed-dot line) and $u_{net} = u_{bulk} + u_{ep}$ (solid line). (f) Normalized concentration profile.

Transient temperature behavior

The spatial and transient temperature profiles along a microchannel filled with 900mM Tris-Borate buffer were approximated using the numerical model. The geometrical parameters were the same as those used in the experimental study of chapter 2 ($2w_{end}$ = 600µm, $2w_{mid}$ = 55µm, L = 16mm, and d = 18µm). As previously reported, the experimental results were obtained using a rhodamine B-based thermometry technique.

Figure 3.4(a) shows a comparison between experimental, numerical, and analytical approximations for the temperature at the center of the channel, $T(N/2)$, vs. time, as well as the numerical prediction for the lumped substrate temperature vs. time. The predicted transient channel temperature profiles clearly exhibit the two distinct thermal timescales seen in the experimental data, with a very steep initial temperature increase followed by a reduced temperature elevation toward steady-state. The analytical solution, equations (3.16)-(3.17), initially agrees well with the numerical solution but shows increasing error with time due to the inability to capture the nonlinear energy input from Joule heating in the analytical formulation. However, its purpose here is primarily to illustrate the two thermal timescales of interest.

Figure 3.4(b) shows a comparison between numerical and experimental spatial temperature profiles near the center of the channel at t = 2 minutes. Both results show similar maximum temperature magnitudes and slopes, validating the model's accuracy for both the transient and spatial thermal behavior.
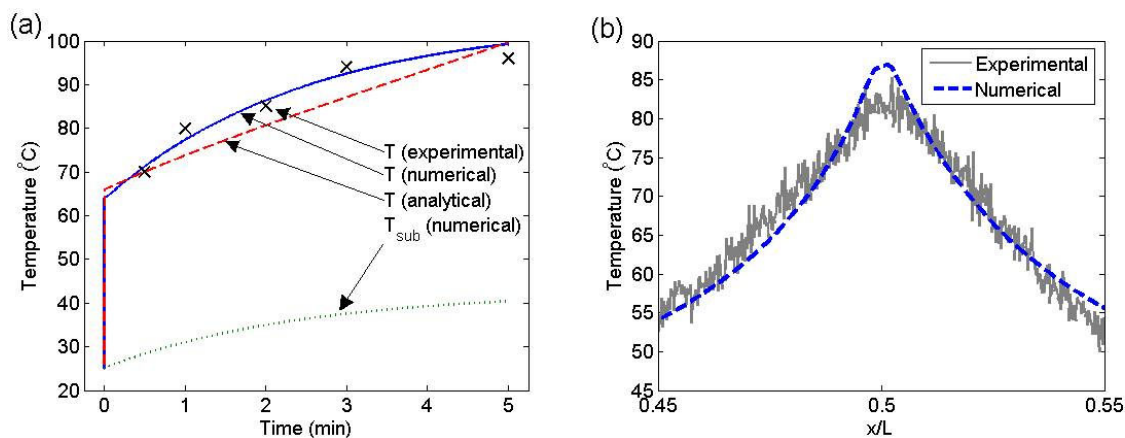
Figure 3.4. Theoretical and experimental comparisons of transient and spatial temperature profiles. (a) Temperature at center of channel, $T(N/2)$, vs. time. T_{sub} represents the transient lumped substrate temperature vs. time. (b) Channel temperature versus x-position at t = 2 minutes. Experimental temperatures measured using the temperature-dependence of the fluorescent intensity of a dilute rhodamine-B in 900mM Tris-Borate solution. 1200V applied at $x = 0$, $x=L$ grounded. $L = 16$mm, $2w_{end} = 600$μm, $2w_{mid} = 500$μm, $d = 18$μm.

Simulations of TGF via Joule heating

Numerical simulations of the TGF mechanism via Joule heating were performed to predict the temperature, velocity, and concentration profiles under variable concentration conditions along the microchannel of the experimental device shown in Figure 2.1(a). The numerical simulation results were compared with experimental results shown earlier.

Figure 3.5 shows a comparison between numerical and experimental results in the concentration behavior of 0.1mM fluorescein-Na in 900mM Tris-Borate buffer during 2 minutes of focusing. The maximum concentration vs. time plots in Figure 3.5(a) show similar behavior and predictions of >200-fold concentration in less than 2 minutes. Note that both curves display an eventual decrease in focusing rates due to increased species migration via diffusion and advective transport. Figure 3.5(b) shows nearly identical results for the species focusing location and concentrated band width at $t = 2$ minutes. Note that the model predicts a slightly wider band than that observed experimentally. This error is most likely due to the approximations used in calculating D_{eff}, equations (3.5) and (3.6).

45
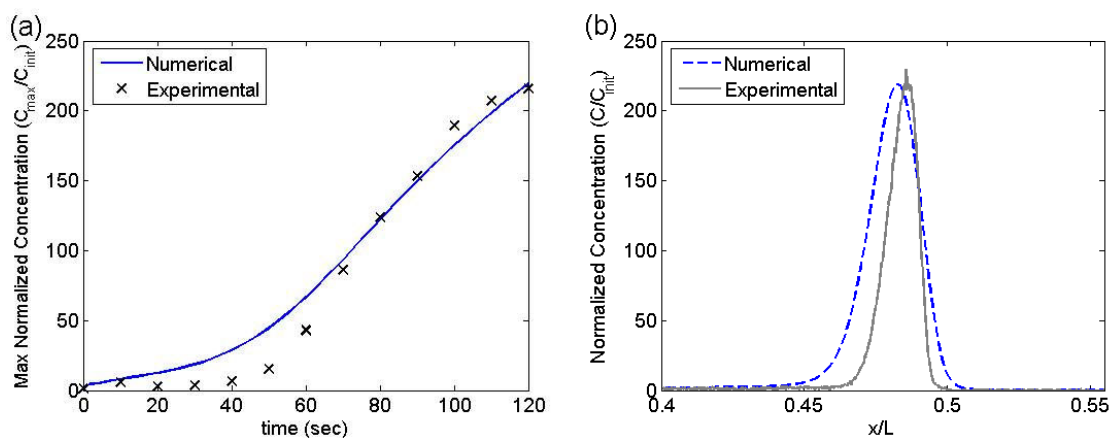
Figure 3.5. Comparison between experimental and predicted concentration profiles of 0.1mM fluorescein-Na in 900mM Tris-Borate buffer. (a) Maximum normalized concentration vs. time. (b) Concentration profiles at t = 2 minutes. Geometrical and experimental parameters same as Figure 3.4.

In perhaps its most useful applications, TGF can separate and focus species of different size and net charge. Our previous work demonstrated a successful separation of 25μM fluorescein-Na and 100nM FITC-BSA in 900mM Tris-Borate buffer. Although these analytes have vastly different sizes, net charges, and mobilities, this demonstration showed the ability of the device to achieve separation. Figure 3.6 shows the simulation results of this same separation using the geometrical configuration from Figure 3.4. Due to the difficulty in photobleaching FITC-BSA with our mobility-measurement system, we were unable to measure its temperature-dependent electrophoretic mobility and therefore approximated a curve using equation (3.10), with r = 5nm and q = -16×(1.602×10^{-19}) coulombs at the pH of this buffer solution [57]. Figure 3.6(a) shows that the net velocity profiles achieve the focusing condition at unique locations for each species, and the concentration profile after 6 minutes of focusing in Figure 3.6(b) displays a separation of analytes comparable with the experimental result from our previous study. Experimentally we achieve baseline resolution for these two components after t > 8 minutes, but we were unable to simulate this result. The most likely cause of the discrepancy is our inability to experimentally measure the species electrophoretic mobility at high temperatures, thus necessitating extrapolated values for T > 80ºC. Nonetheless the primary purpose here is to show that the technique will yield a separation of species with unique temperature-dependent electrophoretic mobility curves.
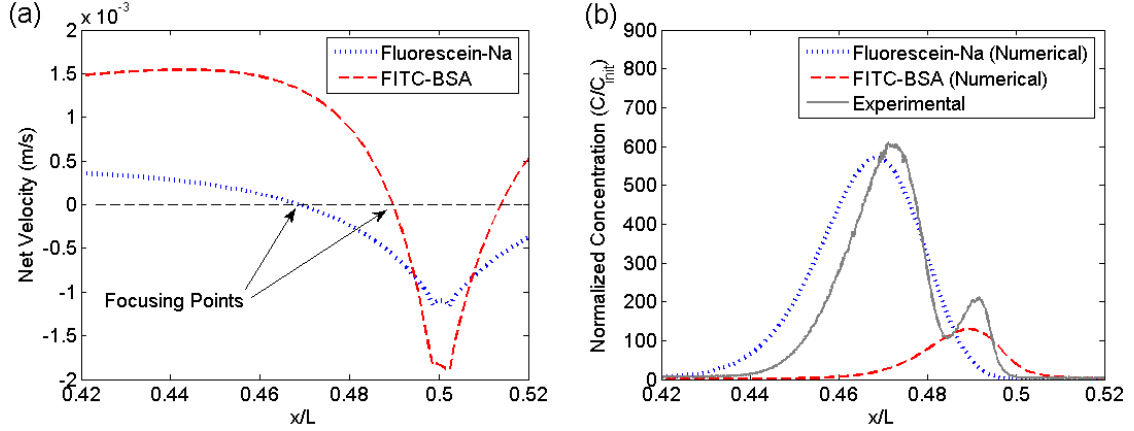
Figure 3.6. Comparison between experimental and numerical simulations of a separation of 25µM fluorescein-Na and 100nM FITC-BSA in 900mM Tris-Borate buffer. (a) Predicted net velocity profiles of each species at t = 6 minutes. (b) Experimental and simulated normalized concentration profiles at t = 6 minutes. Geometrical and experimental parameters same as Figure 3.4.

Parametric studies of geometry and substrate temperature effects

The numerical model was used to study the effects of varying the channel geometry on the focusing phenomena. Figure 3.7 shows the effect of altering the width in the center of the channel, w_{mid}, on the temperature and concentration profiles. Narrowing the center of the channel increases the current density through that region, thus raising its temperature and causing a steeper $\dfrac{\partial T}{\partial x}$ curve. The steeper temperature profile induces a steeper $\dfrac{\partial u_{net}}{\partial x}$ curve, provoking an increased concentration magnitude for the narrowest channel. Even though one can achieve higher and faster concentrations with a narrower center channel, this geometry has a higher risk of inducing thermal runaway and eventual sample solution boiling than the wider center channel. Thus, the trade-off between a stable system and achieving higher concentration should be considered when this TGF system is designed.

The species focusing point is also dependent on the channel geometry. Because of the increased temperature, the focusing point in the narrower center channel is further from x = L/2 because of the location of $u_{net} = 0$ and $\dfrac{\partial u_{net}}{\partial x} < 0$. Note also that the focused

47

band width is seemingly independent of the channel geometry because of the increased concentration gradient at higher concentrations, as well as a slightly higher D_{eff} value at higher temperatures and bulk velocities.
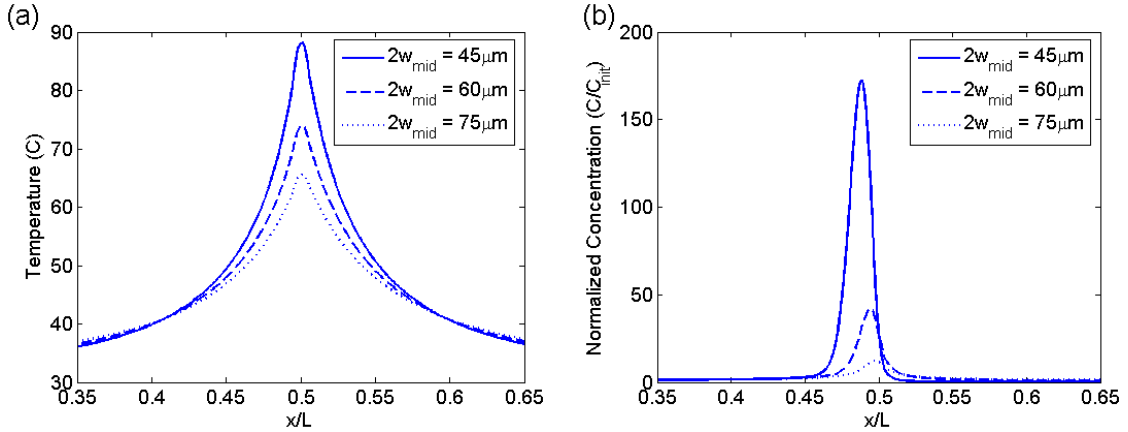
Figure 3.7. Numerical simulation of channel width effects on TGF. 0.1mM fluorescein-Na in 900mM Tris-Borate buffer is simulated. The channel length (L = 16mm), depth (d = 18μm) and end width ($2w_{end}$ = 600μm) are the same for each case. 1200V is applied at $x=0$ and $x=L$ is grounded. Resulting temperature profiles (a) and normalized concentration profiles (b) after 1 minute of focusing. $2w_{mid}$ = 45μm (solid line), 60μm (dashed line) and 75μm (dotted line).

Experimentally we showed that the Joule heating effect can be combined with external heating and cooling of the glass substrate to achieve concentration with a lower applied voltage or a simpler buffer system (chapter 2). Besides requiring less voltage, an externally heated system also has the advantage of being more stable and controlled because of the decreased tendency of the buffer solution's electrical conductivity to induce thermal runaway. An obvious disadvantage of the system, of course, is the increased complexity of introducing external heating and cooling devices. In line with those experiments, the model was used to simulate focusing with different substrate temperatures, T_{sub}, and varied applied voltages, with the results shown in Figure 3.8. Increasing T_{sub} reduces the electric field needed to drive the temperature in the middle of the channel to a temperature sufficient for focusing. For example, focusing is achieved with just 800V applied to the reservoirs when the base temperature is raised to 55ºC. However, the temperature gradient is shallower than that from our standard conditions (1200V applied, T_{sub} = 25ºC), leading to a reduced concentration magnitude. Likewise,

focusing is not achieved with 800V when the base temperature remains at room temperature, or when 1200V is applied with the base temperature lowered to 5°C.
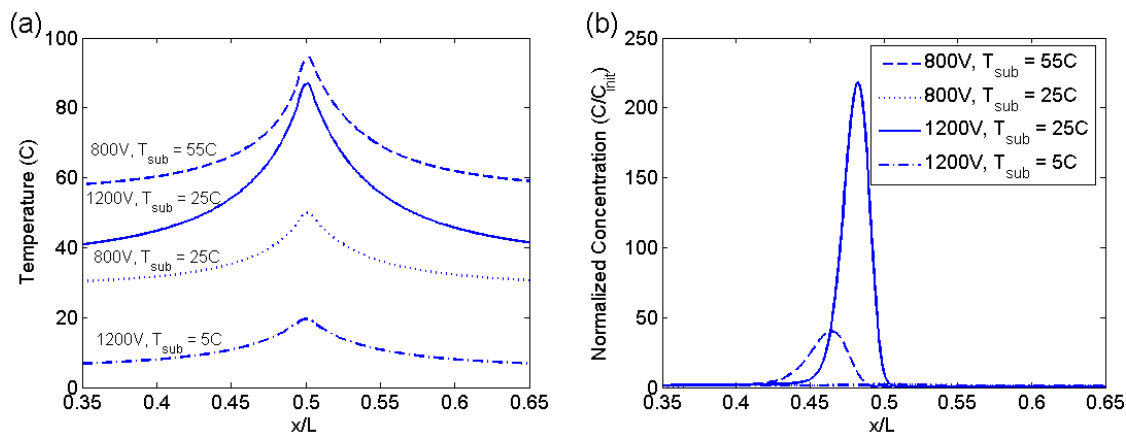
Figure 3.8. Numerical simulation of effects of externally heating and cooling the glass substrate on TGF. Dashed line: $\phi_{x=0}$=800V, T_{base}=55°C (Heating); Dotted line: $\phi_{x=0}$=800V, T_{base}=25°C; Solid line: $\phi_{x=0}$=1200V, T_{base}=25°C; Dashed-dot line: $\phi_{x=0}$=1200V, T_{base}=5°C (Cooling). (a) Temperature profile effects. (b) Concentration profile effects.

TGF using alternative buffer solutions

One of the primary limitations of TGF is that it requires specific buffers with temperature-dependent ionic strengths, such as the 900mM Tris-Borate buffer used thus far. Shackman *et al*. [58] investigated several buffer solutions of various pH using background electrolytes, and demonstrated successful focusing with many of them. Chapter 2 demonstrated focusing using a 20mM phosphate buffer, a result that could significantly accelerate the adoption of TGF in analytical devices. However, the focusing was difficult to achieve, requiring the coupling of external heating devices with a Joule heating device, and was quite unstable as the focused plug quickly dissipated. Figure 3.9 shows a simulation of focusing 0.1mM fluorescein-Na in 20mM phosphate buffer with 800V applied to the left end and the right end grounded. This electric potential profile creates a temperature profile with maximum magnitude very near 100°C, which would cause boiling. The electrophoretic mobility of this analyte-buffer solution was measured as previously described, leading to the net velocity profile shown in Figure 3.9(b). The

velocity profile creates a shallow concentration condition (small $\frac{\partial u_{net}}{\partial x}$) that barely

reaches $u_{net} = 0$ near the center of the channel. This simulation helps illustrate the difficulty of focusing with this buffer as a limited concentration can be achieved only with a steep temperature profile that nearly exceeds 100ºC. Such a temperature profile is experimentally very elusive as the steep temperature dependence of the buffer's electrical conductivity causes a thermal runaway effect under a constant applied voltage, meaning the temperature increases rapidly at higher temperatures. Precise temperature control is difficult yet seemingly essential with this buffer system. Nonetheless, focusing is possible with this simple buffer and more investigation should be given to this and other buffer systems.
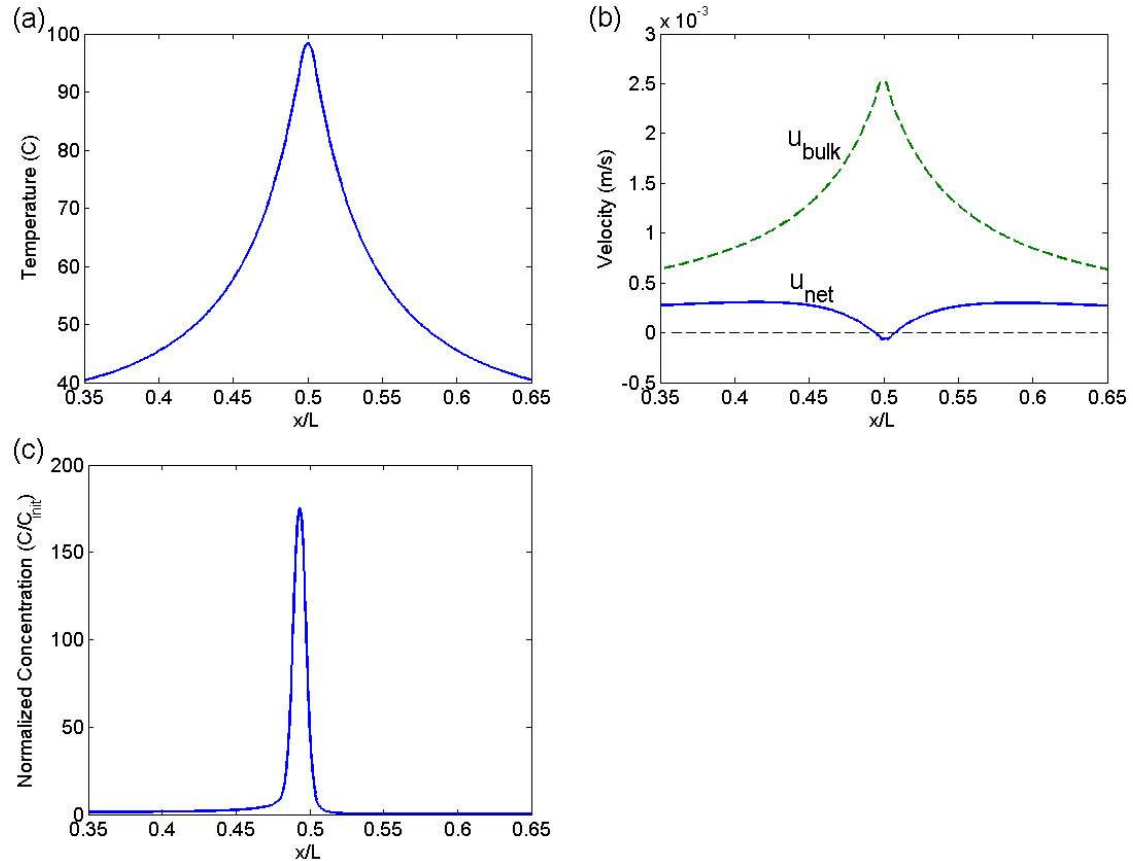
Figure 3.9. Simulated focusing of 0.1mM fluorescein-Na in 20mM phosphate buffer at t = 1 minute. (a) Temperature profile. (b) Bulk and net velocity profiles. (c) Normalized concentration profile. Geometrical profile same as Figure 3.4. 800V applied at $x=0$ and $x=L$ is grounded.

Conclusion

This chapter presented a theoretical analysis of temperature gradient focusing via Joule heating, with the aim of providing rule-of-thumb methodology for the adoption of TGF as a simple and effective focusing technique. A quasi-1D numerical model was developed to simulate the thermal behavior and species transport along a variable-width microchannel. The simulated results show considerable agreement with experimental temperature, concentration, and separation trials, thus validating use of the model as a tool for future device design. The theoretical governing equations and model presented may also serve as a template for analyzing electrokinetic transport in microchannels in devices subject to Joule heating or involving variable-width geometry. In particular, the thermal analysis presented here provides a fundamental depiction of the thermal timescale behavior inherent to many lab-on-a-chip devices.

The numerical model was used to conduct parametric analyses of the effects of varying the channel geometry as well as adjusting the temperature of the device substrate. These parametric studies support experimental results showing that these parameters can enhance the focusing behavior and resolution of the device. The results will be used to maximize separation performance in future device designs and hopefully enable implementation of the technique with a wider range of analytes and buffer systems.

The primary advantage of this device is that it provides a simple, rapid, low-power method for species preconcentration and separation. Implementing a Joule heating-induced temperature gradient vastly reduces the amount of power required for analysis compared with conventional TGF techniques that require external heating and cooling, making it an attractive technique for portable analytical devices. The technique can potentially be combined with other microfluidic diagnostics to yield a compelling tool for proteomic analyses.

CHAPTER 4

ON-CHIP ISOELECTRIC FOCUSING USING
PHOTOPOLYMERIZED IMMOBILIZED pH GRADIENTS

Introduction

Over the past 30 years, isoelectric focusing (IEF) has grown to be a prominent method of separation and detection in proteome research [59-61]. The technique separates and focuses analytical species based on their different isoelectric points (pI), the pH at which an analyte's net charge is zero. Conventional IEF (CA-IEF) is a capillary-based method in which a pH gradient is established using carrier ampholytes (CA's) in solution, which are soluble amphoteric buffers that electrophoretically drift toward their own pI. The CA's in solution provide sufficient buffering capacity and electrical conductivity to establish a pH gradient along the length of the separation channel. However, while today's commercial CA's in general provide adequate buffering capacity and high resolution pH gradients [62], CA-IEF can suffer from poor temporal stability.

The advent of the immobilized pH gradient (IPG) in 1982 by Bjellqvist *et al.* [15] provided a high resolution electrophoretic technique, as well as a means to couple IEF with other gel-based systems to create a powerful 2-D separation tool. IPG's are created by casting a polyacrylamide gel matrix with covalently bonded acrylamido buffers (Immobilines) of different pK. The linear distribution of each Immobiline species imparts a corresponding pH gradient given proper boundary concentrations. IPG's overcome certain disadvantages of CA-IEF separations by enabling temporally stable gradients of any desired pH range. Since its inception, extensive IPG research has led to improved resolution, commercial technology, and its adoption as a reliable and repeatable laboratory proteomic tool [63-65]. Typical IPG-IEF assays are conducted by soaking the

52

sample/buffer solution onto 7-18 cm-long IPG gel strips and applying an electric field for between 12-24 hours. For 2-D separations, solid gel IPG strips provide a convenient means to transfer proteins to a slab gel for subsequent orthogonal separation via electrophoresis.

Several recent investigations have implemented CA-IEF into microscale, on-chip formats [12, 13, 66-68] with some success toward integration with a secondary dimension of separation. Advantages of such devices include the promise of automated total analysis formats, faster separations, no required mobilization for detection, reduced sample volumes, and potentially increased separation efficiencies due to enhanced heat dissipation and, therefore, higher electric fields. However, success has been hindered by lack of temporal stability, CA interactions with proteins, unsuppressed electroosmotic flow, gradient nonlinearity, non-homogeneous buffering capacity and conductivity, and resolution limits achieved on-chip [65]. Additionally, the pH profile is ultimately governed by the carrier ampholyte solution (available commercially in limited pH ranges). Thus control over the resulting pH gradient remains a limitation of these devices. Moreover, CA-IEF is difficult to implement with other modes of separation, such as SDS-PAGE, to achieve multidimensional separations.

Novel alternative IEF approaches are possible on-chip that may not otherwise be practical. Free-flow isoelectric focusing (FFIEF), a variation in which the pH gradient is established transverse to the hydrodynamic flow by electric field, has received considerable attention [69]. Non-ampholyte approaches include pH gradients established by the water electrolysis [70] and thermal gradients [71]. Parallel Isoelectric Devices (PID's) have been developed in which proteins are trapped within Immobiline gel compartments of fixed pH that constitute a step-wise pH gradient [72, 73]. However, many such approaches are at the infant stage and have yet to achieve the success of more traditional macroscale methods. For 2-D separations in particular, chip-based approaches have yet to contend with the slab-gel format.

In spite of the success and wide-spread use of the IPG format, successful implementation of on-chip IPG's have not been reported in the literature. Possible reasons include the difficulty in realizing a microscale casting procedure. Additionally, a gel that remains confined within the chip requires a different approach than typical for the

exposed IPG format. Issues regarding gel "rinsing" steps to remove unpolymerized monomers prior to use, loading of sample and buffer, focused band detection, and mode of integration with a second dimension need to be addressed [74].

In this chapter, a new method for fabricating precise and reproducible on-chip polymer gradients is introduced and used to generate microscale immobilized pH gradients (μIPG's). Established methods of on-chip polyacrylamide gel fabrication [6, 75] are incorporated and adapted to enable pH gradient establishment via diffusion of Immobilines across the separation channel prior to gel photopolymerization.   This technique uses steady-state diffusion and boundary conditions defined by continuous flow of reagents to maintain precise control over monomer distributions across the μIPG segment. A numerical model is used to predict the resulting pH gradient following equilibration of all Immobiline species. The device is then used to separate several fluorescent p*I* markers and proteins via IEF in < 20 minutes.   To our knowledge, this is the first successful on-chip implementation of IPG's. The reported technique offers high resolution IEF with the advantages of an integrated chip-based analysis format amenable to multidimensional separations.

Theory

pH gradient generation

This work presents a new method for fabricating on-chip polymer gradients. The gradient is defined within a channel segment that restricts flow of monomer solution but allows free diffusion of monomer to establish the gradient. Precise control over monomer distribution and a reproducible fabrication process are paramount to successful analysis using IEF. To achieve the required level of precision, aqueous solutions are fed continuously through side channels flanking the gradient segment serving as both "source" and "sink" for monomer at each end. In the specific application of fabricating μIPG's, Immobilines of varying p*K* are distributed across the separation channel from solutions of different pH, such that the desired pH gradient is established following species equilibration. The gradient is then immobilized via photopolymerization.

A numerical model was developed to both track the temporal distribution of Immobiline species and predict the resulting pH gradient across the µIPG based on their boundary concentrations, with the aim of formulating recipes for the aqueous acrylamide solutions of low and high pH. This model has a similar structure as models previously developed [76, 77]. The details of this simulation, including the fundamental equilibrium equations and finite difference scheme used, can be found in Appendix 2.

Separation efficiency

To address the effect of miniaturization on the separation efficiency of an IPG system, we first mention that Giddings and Dahlgren [78] advise against using theoretical plate numbers when assessing IEF due to the steady state nature of its separation mechanism. Therefore, following the theoretical argument employed by Das and Fan [79], we will primarily concern ourselves with the resolution power of the device defined as the minimum analyte pI difference that can be fully resolved, $\Delta(\mathrm{p}I)_{\min}$. The derivation for this parameter, which assumes a similar form as that presented by Das and Fan and stems from classic theory presented by Rilbe [80, 81], can be found in Appendix 2. Here the result is presented in equation (4.1):

$$\Delta(\mathrm{p}I)_{\min} = 4\left(\frac{D}{V}\frac{\Delta pH}{-d\mu/d(pH)}\right)^{1/2} \tag{4.1}$$

Equation (4.1) shows that, given a constant voltage, the resolution power of the system is independent of its separation length. Therefore we can theoretically achieve the resolution of macroscale IPG strips with our device, as long as the same electric potential is applied. We note that this derivation assumes negligible electroosmotic flow (EOF) and Joule heating within the system. Of course the reduced length of a µIPG linearly increases the applied electric field, which can lead to Joule heating and other detrimental affects on the separation efficiency. However, enhanced heat dissipation is an inherent advantage scaling down channel sizes in microfluidic devices due to an increased surface-to-volume ratio, thus limiting the detrimental effect of Joule heating. Joule heating is also less problematic with an IPG system in which buffer concentrations, and thus current, are relatively low. In spite of these advantages, an upper limit to the electric field is reached on-chip as observed by the formation of voids associated with gel

breakdown. This issue seems to be the limiting factor in electric field strength and the deterrent in maximizing separation efficiency.

Another useful consequence of equation (4.1) is that $\Delta(pI)_{min} \propto (\Delta pH)^{1/2}$. This implies that enhanced resolution is achievable by simply reducing the pH range cast in the μIPG. Indeed this is common with macroscale IPG strips, where $\Delta(pI)_{min} \approx 0.001$ has been demonstrated within 10 cm-long IPG strips that span a range of only 0.25 pH units [82].

In practice, the resolving power for IEF systems can be calculated as

$$\Delta(pI)_{min} = \frac{dpH}{dx}(4\bar{\sigma}) \tag{4.2}$$

where $\bar{\sigma}$ is the average bandwidth standard deviation. An additional analytical measure of interest is the peak capacity of the system, calculated simply as

$$n = \frac{L}{4\bar{\sigma}} \tag{4.3}$$

Experimental

Reagents

Urea, thiourea, CHAPS, 3-(trimethoxysilyl)propyl methacrylate (98%), 30% acrylamide/bisacrylamide solution, Carbonic Anhydrase (CA), Hemoglobin (Hb), Phosphorylase B (PhB), and Transferrin (Tfer) were from Sigma (St. Louis, MO). Note: monomeric acrylamide compounds are neurotoxins that can be absorbed through the skin and should be handled only with appropriate precautions. 0.2M acrylamido buffer solutions (pK 3.6, 4.6, 6.2, 7.0, and 9.3), and fluorescent p*I* marker solutions (p*I* 4.0, 4.5, 5.1, 5.5, 6.2, 6.6, and 6.8) were from Fluka (Buchs, Switzerland). Water-soluble photoinitiator 2,2'-azobis[2-methyl-*N*-(2-hydroxyethyl)propionamide] (VA-086) was from Wako Chemicals (Richmond, VA). Alexa Fluor prelabeled Bovine Serum Albumin (BSA) and Ovalbumin (OVA), Alexa Fluor 647 labeling kits and Novex IEF cathode buffer (1X = 20mM Lysine, 20mM Arginine) and anode buffer (1X = 7mM Phosphoric acid) were from Invitrogen (Carslbad, CA). Recombinant Green Fluorescent Protein

(GFP) was from Clontech (Mountain View, CA). CA, Hb, PhB and Tfer were Alexa Fluor-labeled and purified as per the labeling kit instructions.

Device fabrication

Glass (fused silica) microchips were designed in-house and fabricated by Caliper Life Sciences (Hopkinton, MA) using standard isotropic wet etching methods. Channels were ~25 μm deep, ~100 μm wide and arranged in an "H" geometry such that the center 6mm-long channel would eventually support the polymer gradient, as shown in Figure 4.1. To ensure bonding between the polyacrylamide gel and channel wall, the microchannels were coated with acrylate-terminated self-assembled monolayers as previously described [6]. The channels were conditioned with 1M NaOH, rinsed with deionized water, and dried thoroughly using a vacuum. A 2:3:5 (v/v/v) mixture of 3-(trimethoxysilyl)propyl methacrylate, glacial acetic acid, and deionized water was sonicated, degassed, and loaded into the channels. The device was incubated with the solution for 30 minutes, rinsed with a 3:7 mixture of acetic acid and water, rinsed with deionized water, and thoroughly dried with a vacuum.

A thin (~50 μm wide) polyacrylamide membrane was fabricated near the low-pH end of the separation channel [6] by loading a degassed solution of 10%T, 2.6%C[i] acrylamide/bisacrylamide with 0.2% (w/v) VA-086 photoinitiator into the channel, capping the reservoir holes with tape, allowing the solution to equilibrate, and exposing the region to a rectangular shaped 355-nm laser beam for 15 seconds. The membrane prevents fluid flow through the separation channel while allowing a gradient to be established by monomeric diffusion.

A high pH (pH 7.0) solution and low pH (pH 3.8) solution of 5% T, 2.6%C acrylamide/bisacrylamide, 0.2% (w/v) VA-086 photoinitiator, and calculated amounts of acrylamido buffers were mixed using the recipe shown in Table 4.1, sonicated, and degassed. 2μL of each solution was loaded into both reservoir holes on either side of the separation channel. The microchip was then loaded into a custom manifold as previously described [83], allowing simple attachment of 2.5cm tall cylindrical plastic reservoirs fabricated from 200μL pipette tips to each reservoir hole. The reservoirs on either side of the separation channel were then loaded with the monomer/Immobiline/photoinitiator

solutions of different pH so as to induce continuous flow along the side channels adjacent to the separation channel, as shown in Figure 4.1(a).

The microdevice was kept in a damp, dark environment for a sufficient time period to allow linear equilibration of the Immobilines across the separation channel, as shown in Figure 4.1(b). Devices were typically equilibrated overnight for $t_{SS} > 16$ hours to ensure linear distributions.

Following equilibration the excess solution in the reservoirs was removed and the entire microchip was set 6cm above a 100W 365nm lamp for 8 minutes to photopolymerize the gel. The excess gel in each via reservoir was removed and the chip was stored in either deionized water (for native IEF) or denaturing buffer until use. Note that the gel must remain hydrated following polymerization; upon dehydration the gel becomes defective.

Table 4.1. Recipe for preparing pH 3.8 and pH 7.0 solutions for µIPG fabrication

Reagent	pH 3.8 solution	pH 7.0 solution
Acrylamide/bisacrylamide	5%T, 2.6%C	5%T, 2.6%C
Acrylamido buffer pK 3.6	12.7mM	4.40mM
Acrylamido buffer pK 4.6	-	10.3mM
Acrylamido buffer pK 6.2	7.48mM	2.36mM
Acrylamido buffer pK 7.0	-	4.17mM
Acrylamido buffer pK 9.3	-	12.1mM
VA-086 photoinitiator	0.2% (w/v)	0.2% (w/v)
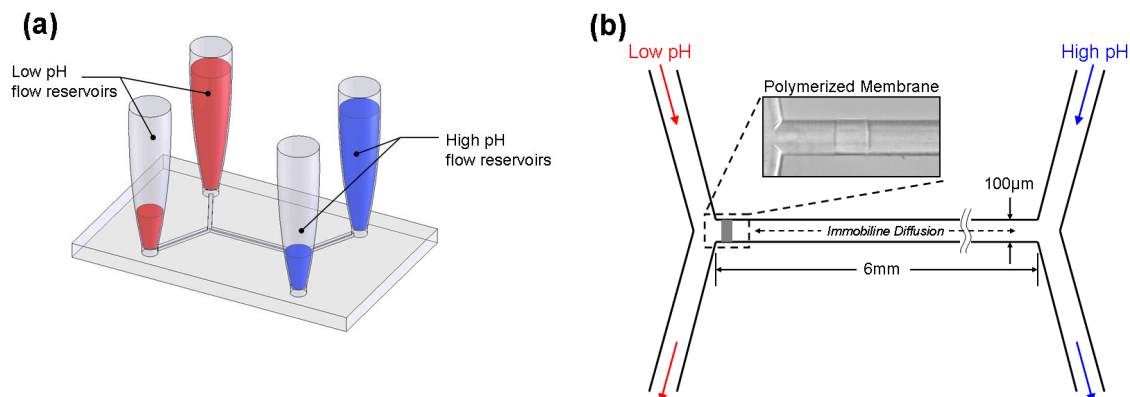
Figure 4.1. µIPG fabrication schematics. (a) Plastic reservoirs are used to provide continuous pressure driven flow through the side channels of the glass microchip. (b) Geometrical schematic of microdevice. A polymerized polyacrylamide membrane prohibits flow across the separation channel yet allows equilibration of Immobiline species via diffusion. Entire chip is polymerized with UV light following equilibration. Depth is ~25µm.

Diffusion-induced linear gradient evaluation

To quantify the linearity and equilibration time of the gradient generation approach employed in this work, microchips were fabricated with a fluorescent dye (Alexa Fluor 555) added to the monomer/photoinitiator solution on one side of the channel (solutions were kept at constant pH in this case). The dye has a slightly larger molecular size than the Immobiline monomers, and thus provides a cautious estimation of the induced gradient. Two solutions of 5%T, 2.6%C acrylamide/bisacrylamide with 0.2% (w/v) VA-086 were mixed and degassed, and one of those solutions was spiked with 5µM Alexa Fluor 555. The microchip was then fabricated as previously described and images were captured at intermittent time steps using an inverted epifluorescence microscope (IX-70, Olympus, Melville, NY) equipped with a 1300 × 1030 pixel, Peltier-cooled interline CCD camera (CoolSnap HQ, Roper Scientific, Trenton, NJ) to approximate the induced gradient profile. All images were captured using Image-Pro Plus imaging software (MediaCybernetics, Bethesda, MD), and analyzed with Image J (National Institutes of Health, Bethesda, MD).

Separation experiments

For all separation experiments, the microdevice was loaded into the same manifold used in chip fabrication and mounted upon the inverted epifluorescence microscope described previously. Electric fields were applied through platinum electrodes using a programmable high-voltage power supply fabricated in-house [83].

The current layout of the µIPG device requires different preparatory and separation protocols than macroscale IPG strips, mostly due to the limited access to the gel via the adjoining microchannels. For instance, new µIPG chips were rinsed both electrophoretically and via diffusive buffer exchange. Chips were electrophoretically rinsed by loading via wells with buffer and applying a low E-field (15 V/cm) across the channel for 1 hour to equilibrate the chip with buffer and remove unpolymerized monomer or other impurities from the device. Note that relying solely on an electrophoretic rinsing protocol may require modification depending on the chip layout and specific recipe employed (e.g., basic Immobilines may stack and not effectively be cleared via electrophoresis through a gel segment that is >2 pH units above the pK, leading to dynamic changes in the gradient profile while clearing unpolymerized monomer that may further limit transport). For native running conditions, Novex IEF cathode buffer (20mM Lysine, 20mM Arginine) and anode buffer (7mM Phosphoric acid) were used as the catholyte and anolyte, respectively. For diffusive rinsing under denaturing conditions, chips were soaked for at least 24 hours with 8M urea, 2M thiourea, and 4% (w/v) CHAPS included in the 1X IEF buffers.

Samples were diluted to concentrations ranging from 1nM (fluorescent pI markers) to 50nM (proteins) in catholyte and introduced via one of the two reservoirs on the pH 7.0 side. Unlike the macroscale IPG format where sample is soaked into the gel, analytes were electrophoretically loaded in stages: first into the cathode side-channel and then into the µIPG segment for focusing. Sample can be electrophoretically loaded and focused simultaneously. To load the analyte into the pH 7.0 side channel, an electric field of ~100V/cm was applied to rapidly drive analyte from sample reservoir toward the other reservoir filled with cathode buffer. This step lasted typically between 2 and 10 minutes depending on the electrophoretic mobility of the injected species to fill the side channel with fully concentrated sample. With sample in the side channel, the electric

field was switched across the IPG segment (cathode buffer reservoir to anode buffer reservoir) to draw in and focus sample. The electric field was slowly ramped up from 50V/cm $< E <$ 350V/cm to minimize tendency for precipitation. Maximal focusing was achieved within 20 minutes or less.

Note that analyte is electrophoretically concentrated within the separation channel for as long as the field is applied from a channel or reservoir containing sample. Sample may be loaded for additional time to further concentrate sample within the µIPG if desired. Bands that may be too dilute for detection, depending on the initial concentration and level of focusing achieved, could be intensified with longer loading time. Because loading rates may vary for each analyte depending on electrophoretic mobility at the pH of the loading channel, a minimum loading time for each analyte achieves the equivalent of a traditional IPG loading step. However, sweeping a channel volume of sample into the µIPG better insures that relative concentrations of analyte mirror the original sample. The sample volume swept from the side channel for the devices used was equivalent to the total volume of the µIPG channel.

Results

Linear gradient evaluation

Precisely defined gradients can be fabricated on-chip using the proposed method in which monomer species distribute via diffusion from side channels acting as both "source" and "sink". To demonstrate the proposed technique's control over monomer distribution, fluorescent dye was added to one side of the device (with both sides at constant pH) such that its spatial and temporal distribution could be calculated based on fluorescent intensity.

Incremental results of the diffusion of Alexa Fluor 555 dye across the 6mm-long center channel are shown in Figure 4.2. Similar results were obtained whether dye was loaded in the side-channel immediately adjacent to or across from the flow-restricting membrane, thus confirming that the relatively large pore size of the membrane minimally reduced diffusivity of monomer-sized species. Background-corrected fluorescent

intensities were normalized with a flood image of a similar channel containing constant dye concentration. The experimental data is compared with the gradient predicted using the simple diffusion equation:

$$\frac{\partial c_i}{\partial t} = D_i \frac{\partial^2 c_i}{\partial x^2}$$

(4.4)

where the diffusion coefficient of the fluorescent molecules is estimated to be [84] $D = 1.8 \times 10^{-10} \, m^2/s$. The results show that this approach indeed yields a linear gradient of monomeric species confined to the desired channel segment following adequate equilibration time. Note that $t_{ss} \propto L^2$, therefore this time period must be adjusted when fabricating polymer gradients within channels of different length, or when nonlinear gradients are preferred. If desired, shorter L can dramatically reduce equilibration time with the trade-off of lower peak capacity within the segment, which is not necessarily a limitation if multiple segments are fabricated on the same chip. The concentration gradient will remain linear and confined to this segment provided that the solutions in the bordering side channels continue to flow. Without continuous flow in the flanking channels, monomer gradients will extend beyond the desired channel segment and may prove difficult to control and predict.
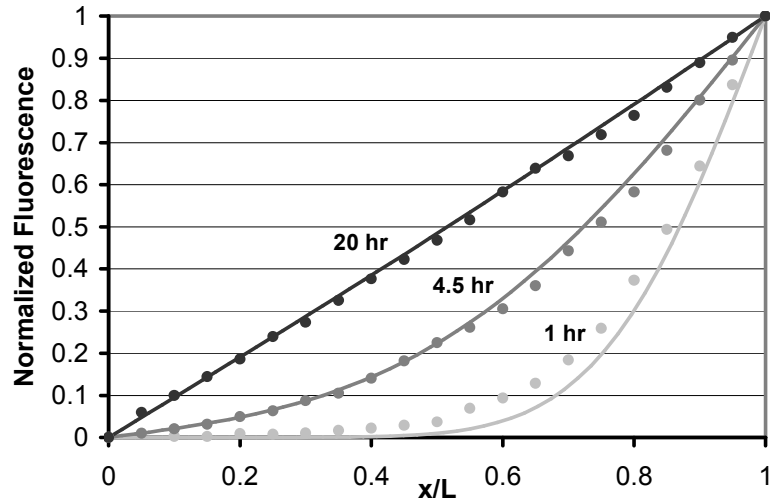
Figure 4.2. Time-dependent diffusion profiles of AlexaFluor 555 across 6 mm-long center channel. Experimental data (circles) are plotted along with predicted gradients calculated using equation (4.4) (solid lines).

pI marker and protein separations

Performance of the μIPG system was excellent, as shown in Figure 4.3a with fluorescent micrographs of several fluorescent pI markers and protein species focused along a pH 3.8 – 7.0 gradient. On-chip μIPG focusing was much faster than that possible with macroscale IPG strips, as demonstrated by high-resolution focusing of markers and proteins within 20 minutes. The pI markers in Figure 4.3a(i) ranging in pI from 4.0 – 6.8 were focused for 20 minutes under non-denaturing conditions and used to quantify the pH gradient across the μIPG. Figure 4.3a(ii) shows the separation of several proteins labeled with Alexa Fluor 647 dye and focused under denaturing conditions for 20 minutes. Sample proteins included bovine serum albumin (BSA, pI = 4.85), transferrin (Tfer, pI = 5.34), carbonic anhydrase (CA, bovine, pI = 6.16), phosphorylase B (PhB, rabbit muscle, pI = 6.30), and bovine hemoglobin (Hb, pI = 6.48). Figure 4.3a(iii) is a composite image of Alexa Fluor 488-labeled ovalbumin (OVA, pI = 4.43) focused under denaturing conditions, as well as non-denatured green fluorescent protein (GFP, pI = 5.00). The multiple focusing locations seen for some samples likely arise from either contaminants in the sample, species dimerization, or labeling effects from the Alexa Fluor dyes used in sample preparation. Fluorescent labeling can result in the formation of multiple species, with each having a slightly different pI [85], the CyDyes commonly used for DIGE analysis being an exception [86].

Figure 4.3b is a plot comparing the observed pH profile across the μIPG (calculated using the spatial focusing locations of the seven pI markers averaged over runs in three separate devices) with that predicted numerically based on linear gradients of Immobilines for the defined boundary conditions. As evident in this plot, the resulting pH gradient deviates from the linearity of the predicted profile. To rule out equilibration time as a factor, longer equilibration times were tested (even though diffusivity of the Immobilines was expected to be higher than the Alexa Fluor 555 dye used to empirically establish a conservative equilibration time). There was no added benefit to linearity for equilibration times up to 48 hours. The μIPG devices also exhibited pH gradient reproducibility from device to device, as indicated with the horizontal error bars in Figure 3b representing the spatial standard deviation of pI markers focused in the three separate devices. To confirm the prediction of gradient linearity, the recipe was evaluated with a

second program, IPGMAKER, widely used to develop IPG recipes [76]. The resulting profile matched the steady state prediction of gradient linearity.

However, it was found that the target pH range was broad enough that Immobilines serving as titrants should have been included in the recipe. As reported by Righetti [74], achieving linearity and uniform buffering capacity becomes increasingly difficult across wider pH intervals, such as that attempted here, and requires addition of Immobiline titrants with pK's at least 2 pH units above and below the desired pH range. The employed recipe does not satisfy that criteria on the acidic end with a pK 3.6 Immobiline only 0.2 pH units below the desired endpoint. Therefore, the best attempts to optimize both linearity and uniformity of buffering capacity (for the targeted pH range) would likely result in a flawed recipe using the Immobilines listed in Table 4.1. The slight "bowing" noticeable in the theoretical pH profiles is likely amplified experimentally as a result of nonuniform buffering capacity. A linear pH gradient for the targeted range should be achieved with an optimized recipe that includes a pK 1.0 titrating Immobiline.
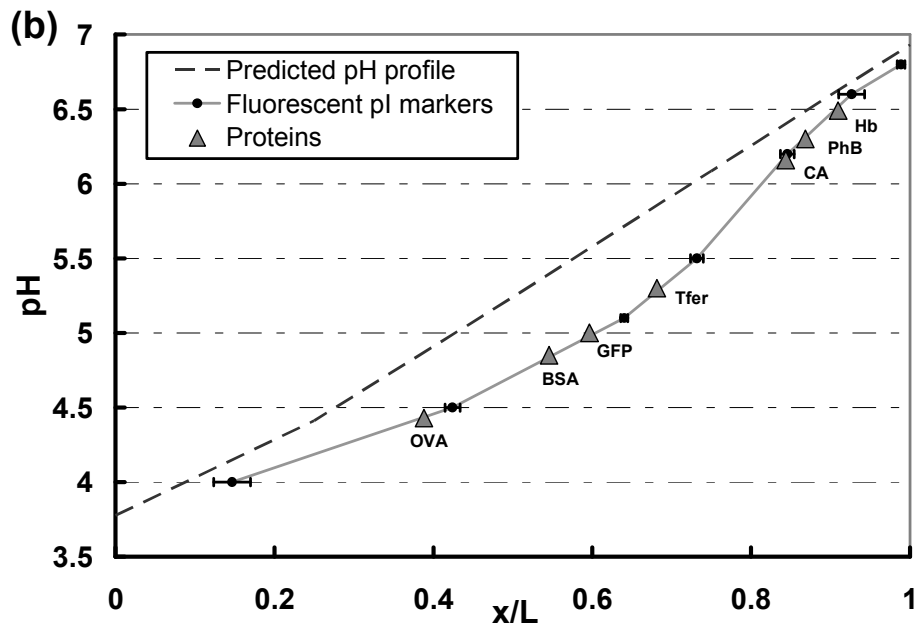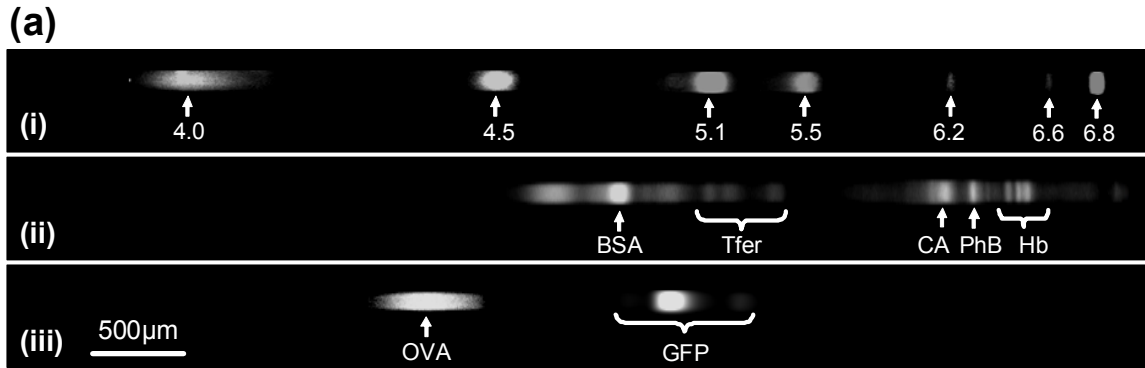
Figure 4.3. (a) Composite fluorescence IEF images spanning length of 6mm-long µIPG. (i) Fluorescent p*I* markers. (ii) AF 647-labeled proteins: Bovine serum albumin (BSA), Transferrin (Tfer), Carbonic anhydrase (CA, bovine), Phosphorylase B (PhB, rabbit muscle), Hemoglobin (Hb, bovine). (iii) AF 488-labeled ovalbumin (OVA) and green fluorescent protein (GFP). Fluorescent p*I* markers and GFP focused under non-denaturing conditions, all other proteins focused under denaturing conditions. (b) Comparison of pH profile predicted with numerical simulation (dashed line) with actual pH profile inferred from averaged focusing location of fluorescent p*I* markers in three separate devices (solid line). Horizontal error bars represent the spatial focusing location standard deviations. Protein focusing locations are denoted with triangles.

Resolution

　　　　The high resolution focusing achieved with μIPG's is an improvement over reported on-chip methods. Figure 4.4a shows the fluorescence profile of the GFP focused in Figure 4.3a(iii) under non-denaturing conditions. The three resolved bands are consistent with previous slab gel IEF results of GFP [87], with the predominant band at pI 5.00 and two secondary bands at pI 4.88 and 5.19. With an average bandwidth variance of $\sigma^2 \approx 0.42$ μm^2 in this plot, the resolving power in this region of the gel is $\Delta(pI)_{min} \approx 0.040$. Similar calculations for the carbonic anhydrase, phosphorylase B and bovine hemoglobin bands in Figure 4.4(b) reveal a slightly higher value of $\Delta(pI)_{min} \approx$ 0.054. We approximate the peak capacity for this 6mm-long μIPG to be $n \approx 78$.

　　　　These resolution calculations show slight improvement over some of the highest reported resolutions with on-chip CA-IEF separations, and ~10-fold improvement over the highest resolution FFIEF devices. However, a significant advantage of our μIPG system is that it enables further resolution enhancement by simply adjusting the pH range or length of the gel, as is typically done with macroscale IPG strips. Equation (4.10) clearly exhibits this potential, since $\Delta(pI)_{min} \propto (\Delta pH)^{1/2}$.

　　　　It is also possible that resolution could be improved by adding carrier ampholytes to the sample buffer solution to both strengthen the pH gradient and enhance the buffering capacity across the channel. We found, however, that CA's added unnecessary complexity to the separation and that our results were more consistent without. Loading CA's to the μIPG requires electrophoretic manipulation and therefore is not as straightforward as macroscale procedures in which the entire IPG strip is simply soaked with the buffering solution. The CA's presumably have much higher electrophoretic mobility than proteins entering the μIPG segment and would therefore concentrate must faster within the segment. Care must be taken to not overload the μIPG with CA's, which can lead to excessive conductivity and a skewed pH gradient; in conventional IPG methodology it is advised to load the gel with no more than 0.5% (v/v) CA solution [63].
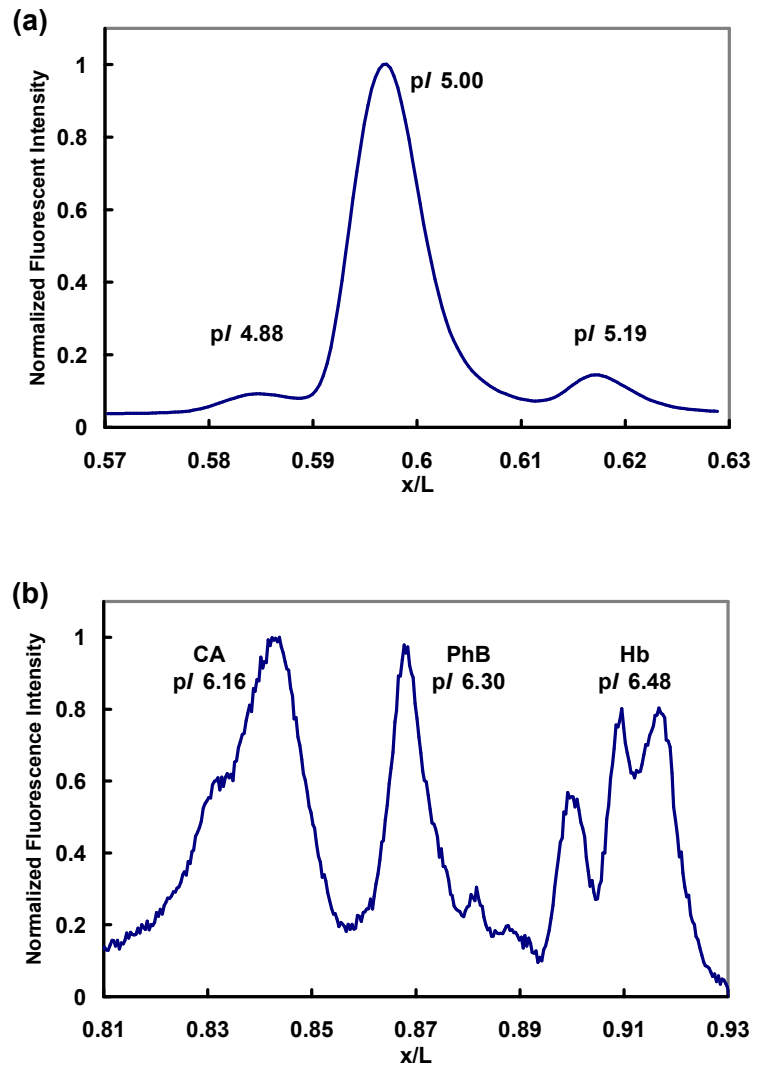
Figure 4.4. Fluorescent intensity profiles of focused proteins. (a) GFP focused under non-denaturing conditions. Profile shown after 18 minutes of focusing under ~300V/cm. (b) Carbonic anhydrase (CA), phosphorylase B (PhB) and bovine hemoglobin (Hb) focused under denaturing conditions. Profile shown following 20 minutes of focusing under ~350 V/cm.

Conclusions

The described µIPG methodology, the first successful on-chip IPG adaptation, exhibits several advantages over macroscale IEF conducted with commercial IPG strips. First, separation time (< 20 minutes) is a ~50-fold improvement due to the reduction in length scale. Moreover, this device requires ~200-fold less sample volume than a typical IPG strip, while allowing for convenient electrophoretic sample loading into the µIPG should additional sample be required. The gel-based format, which serves as a barrier to flow, may be especially advantageous for integration with other microscale architectures and multidimensional separations on-chip. The device also overcomes several shortcomings of most microscale CA-IEF and FFIEF devices, including temporal stability and CA-protein interactions, while providing comparable resolution ($\Delta(pI)_{min} \approx$ 0.040) and peak capacity ($n \approx 78$). Resolution can be improved analogous to IPG strips by reducing the pH range immobilized across the µIPG.

While µIPG's exhibit several benefits over conventional IPG methodology, it should be noted that certain conveniences of conventional IPG strips have not been addressed. Foremost is accessibility to the strip for secondary preparative or analytical measures, such as mass spectrometry, post-staining or orthogonal separations. The present chip layout was designed for the simplest possible feasibility test for casting µIPG's. The resulting µIPG's were fixed and accessible only at the two ends of the channel. However, as step-wise fabrication of devices integrating multiple gel types as well as open channel regions have been demonstrated, these limitations should be addressable. Relevant examples include the recent on-chip combinations of CA-IEF with native PAGE by Das *et al* [88] and with SDS-PAGE by Li *et al* [89] for 2-D separations. Integrating fixed µIPG sections on-chip with techniques previously developed in our lab for size-based separations [6, 75, 90] holds promise for improved performance over existing 2-D separation microdevices, and enhanced speed and convenience over current macroscale 2DGE methodology.

The simple and well-controlled gradient fabrication procedure presented here can also be used to generate nonlinear or stepwise gradient profiles. Chips can be designed to generate "serial" IPG configurations, in which certain regions of the pH gradient support

steeper or shallower *d(pH)/dx* gradients, depending on the complexity of the sample. Three-segment serial configurations were readily fabricated using this method without loss of precision (fluorescent monomer gradients, results not shown). Other options include "parallel" IPG configurations, in which a sample is concurrently fed into multiple μIPG channels with different $\Delta pH/L$ profiles. In this manner the chip can instantaneously provide a "broad" sample separation as well as multiple "fine-tuned" separations with higher resolution for certain pH ranges.

CHAPTER 5

POLYACRYLAMIDE POROSITY GRADIENTS IMMOBILIZED ON-CHIP FOR PROTEIN CONCENTRATION AND SEPARATION VIA PORE LIMIT ELECTROPHORESIS

Introduction

Pore limit electrophoresis (PLE) was introduced in the late 1960's as a method for protein fractionation across a gel supporting a porosity gradient such that a species' molecular weight (M_r) can be deduced from its distance migrated along the gel [91-95]. Pore size is principally controlled in polyacrylamide gels by varying the total concentration of acrylamide monomer (%T); however several studies [96-98] have demonstrated further porosity restrictions by simultaneously increasing the bisacrylamide crosslinker concentration (%C). At high crosslinker concentrations a gel will eventually exhibit turbidity, thus establishing a crosslinking "critical point" above which pore size will increase rather than decrease [99].

It has become generally accepted, both experimentally and theoretically [100, 101], that proteins fail to reach a true "dead stop" and that, given sufficient time, the species will continue to migrate through the gel – presumably due to a distribution of actual pore size at any location. However, for larger proteins the migration halts to a negligible rate within a reasonable run time such that an "effective" pore limit can be assumed.

While proven effective in improving peak resolution for the fractionation of complex samples [102], PLE has yet to be implemented as a standard analytical technique and, as such, has received little attention in the literature in recent years. Prevalent problems and limitations with the technique include: a) lack of a reliable and

accurate gel fabrication technique [103, 104] – complex gradient formation apparatuses involving mechanical stirrers and peristaltic pumps are typically used to cast macroscale PLE gels, b) lengthy and impractical run times of several hours to several days, and c) difficulty in extracting proteins from the gel as they are seemingly "trapped" upon reaching the pore limit.

In this chapter a new method is presented for polymerizing linear pore gradient gels within microchannels for on-chip microscale pore limit electrophoresis (µPLE). A simple and reliable fabrication technique is used based on diffusion of monomer and crosslinker across microchannels of any length. Native µPLE is demonstrated with several proteins of varying molecular size. The technique is also shown to enable stable pre-concentration of dilute samples with >40,000-fold concentration factors easily obtainable given adequate run time. µPLE can also be used in the design of thin membrane barrier systems that permit and exclude proteins based on M_r at controlled E-fields. Such a system would provide a rapid and highly selective tool for the fractionation of dilute, complex samples.

Theory

The Ferguson relationship, published in 1964 [105], has been widely used to approximate the logarithmic dependence of a protein's electrophoretic mobility on the gel's concentration parameters:

$$\log_{10} \frac{\mu}{\mu_0} = -K_R T \tag{5.1}$$

or

$$\ln \frac{\mu}{\mu_0} = -bT \tag{5.1a}$$

where μ_0 is the reference (free) mobility, K_R is the retardation coefficient, $b = K_R \ln(10)$, and T is the total acrylamide concentration.

The PLE gels fabricated in this work linearly vary not only the total acrylamide monomer concentration (%T), but also the degree of crosslinking (%C) with

bisacrylamide. While the true effect of varying the bisacrylamide concentration on pore size is complex and not entirely understood, Johnson provided an adapted Ferguson relationship to account for the amount of crosslinking based on empirical results [98]. For the sake of simplicity, in this analysis the following similar, yet less detailed, logarithmic relationship is assumed:

$$\ln \frac{\mu(x)}{\mu_0} = -RG(x) \tag{5.2}$$

where R is a constant that accounts for the retardation terms, and G represents the linear gel concentrations (%T and %C) at any point x along the channel: $G(x) = \frac{G_L - G_0}{L} x + G_0$.

The electrophoretic velocity of a species at any point in the channel is given by:

$$u_{ep}(x) = \mu(x)E(x) \tag{5.3}$$

where $E(x) \propto \frac{V}{A} x$ is the electric field strength and A is the porous cross-sectional area within the gel. Thus the electric field rises slightly in the higher concentration, less porous regions of the gel.

The spatial and temporal concentration of species is governed by the following conservation equation:

$$\frac{\partial c}{\partial t} = -\frac{\partial}{\partial x}\left[D\frac{\partial c}{\partial x} + u_{ep}c \right] \tag{5.4}$$

where $D(x)$ is the dispersion coefficient.

An interesting asymptotic limit solution to this equation can be derived to look at some scaling effects on initial concentration factors within the system. If dispersion is neglected for the moment and assume that the concentration, c, is everywhere locally constant ($\frac{\partial c}{\partial x} \approx 0$), equation (5.4) can be rearranged and solved to yield:

$$\ln \frac{c(x,t)}{c_0} = -\frac{du_{ep}}{dx} t \tag{5.5}$$

where c_0 represents some reference concentration.

By differentiating equation (5.3) and rearranging equation (5.5), we can approximate the relative concentration magnitudes at any point in the channel:

$$\frac{du_{ep}}{dx}(x) = -\frac{E(x)\mu_0 R(G_L - G_0)}{L}e^{-R\left((G_L - G_0)\frac{x}{L}+G_0\right)}$$ (5.6)

$$\frac{c(x,t)}{c_0} = e^{-\frac{du_{ep}}{dx}(x)t}$$ (5.6a)

This solution suggests that the concentration factor at the plug front will scale exponentially with increasing electric fields and decreasing channel lengths. Of course the concentration magnitude will be limited by dispersion in the system and high electric fields will ultimately induce heating and possible deterioration within the gel, but this analysis provides a simple rule-of-thumb approximation for μPLE design where enhanced concentration factors are required.

Experimental

Materials

40% acrylamide solution and 3-(trimethoxysilyl)propyl methacrylate (98%) were from Sigma (St. Louis, MO). N,N'-methylenebisacrylamide was from Fluka (Buchs, Switzerland). Water-soluble photoinitiator 2,2'-azobis[2-methyl-*N*-(2-hydroxyethyl)propionamide] (VA-086) was from Wako Chemicals (Richmond, VA). Tris/Glycine buffer (10X: 1X = 25mM Tris, 192mM Glycine, pH 8.3) was from Bio-Rad Laboratories (Hercules, CA).

Device fabrication

Polyacrylamide gels supporting a linear pore size gradient were polymerized within microchannels using the adapted diffusion-based polymer gradient fabrication technique presented in the previous chapter and illustrated in Figure 5.1. Glass microchips were designed in-house and fabricated by Caliper Life Sciences (Hopkinton, MA). The microchannels were arranged in an "H" configuration such that the center μPLE channel is flanked by two longer side channels connected to via reservoirs. The

channels were coated with acrylate-terminated self-assembled monolayers to ensure bonding between the gel and glass sidewalls. The microchips were first rinsed with 1M NaOH, rinsed twice with deionized water, and thoroughly dried via vacuum. A 2:3:5 (v/v/v) solution of 3-(trimethoxysilyl)propyl methacrylate, glacial acetic acid, and deionized water was mixed, sonicated, degassed, and loaded into the channels. Following 30 minutes of incubation, the channels were rinsed with a 3:7 mixture of acetic acid and water, rinsed with deionized water, and thoroughly dried via vacuum. 10%T, 2.6%C and 40%T, 12%C acrylamide/bisacrylamide solutions with 0.2% (w/v) VA-086 photoinitiator and 1X Tris/Glycine buffer were mixed, sonicated and degassed using the recipes shown in Table 5.1. The channels were loaded with 10%T, 2.6%C solution and all via holes were equilibrated taped off to prevent flow. A thin membrane was polymerized near the eventual 40%T end of the center channel by exposing that region to a rectangular shaped 355-nm laser beam for 15 seconds. The thin membrane prevents bulk flow through that channel while still allowing monomer diffusion. The chip was then loaded into a custom manifold as previously described [106] and the acrylamide/bisacrylamide solutions were fed through the side channels using a simple height difference in the reservoirs. The entire device was kept in a moist, dark environment for ~20 hours to ensure complete linear monomer equilibration across the μPLE channel. Following equilibration the 40%T side channel was masked off, (polymerization of this solution can induce bubbles in the channel), and the unmasked portions of the chip were exposed to a 100W 365nm lamp for 8 minutes to polymerize the gel. The chip was then removed from the manifold and stored in 1X Tris/Glycine buffer until use.

10%T, 2.6%C
Thin Membrane

100µm

L

10%T, 2.6%C

40%T, 12%C

Monomer Diffusion
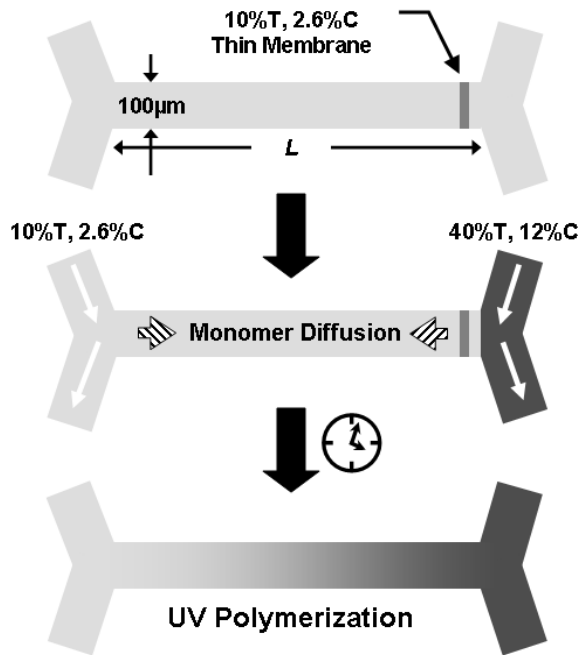
UV Polymerization

Figure 5.1. Fabrication of 10%T, 2.6%C → 40%T, 12%C µPLE channel. Side channels are ~15mm long and connected to via reservoirs. Channel depth ≈ 25µm. A thin membrane is polymerized near one end of the central separation channel to prevent bulk flow while allowing diffusion of monomer and crosslinker. Aqueous boundary solutions are flown continuously via gravity through adjoining side channels to establish a linear species gradient across the separation channel. Following equilibration the channel is polymerized via exposure to a 100W, 365nm UV lamp for 8 minutes. The device is then stored in 1X Tris/Glycine buffer until use.

Table 5.1. Recipe for preparing 10%T, 2.6%C and 40%T, 12%C solutions

	10%T, 2.6%C	**40%T, 12%C**
VA-086 photoinitiator	3 mg	3 mg
40% acrylamide solution	365 µL	1.320 mL
N,N'-methylenebisacrylamide	3.9 mg	72 mg
10X Tris/Glycine buffer	150 µL	150 µL
Deioniozed H$_2$0	985 µL	30 µL
Total Volume	1.5 mL	1.5 mL

µPLE Experiments

For all experiments, the device was loaded into the same manifold used in fabrication and mounted upon an inverted epifluorescence microscope (IX-70, Olympus, Melville, NY) equipped with a 1300 × 1030 pixel, Peltier-cooled interline CCD camera (CoolSnap HQ, Roper Scientific, Trenton, NJ). Prior to sample loading, channels were pre-run with 1X Tris/Glycine buffer for 20 minutes to remove any unpolymerized monomer and establish a stable electric field. Electric fields were applied through platinum electrodes using a programmable high-voltage power supply fabricated in-house [83]. Fluorescently-labeled protein samples were diluted in 1X Tris/Glycine buffer and loaded onto the separation channel via electrophoresis along the 10%T side channel. For separation experiments, the sample reservoir was emptied and replaced with buffer once a sample plug was loaded onto the separation channel. For pre-concentration experiments the sample was loaded continuously. Images were captured at various time increments and analyzed using Image-Pro Plus imaging software (MediaCybernetics, Bethesda, MD).

Results and Discussion

The experimental results presented in this manuscript were all acquired with μPLE gels ranging from 10%T, 2.6%C → 40%T, 12%C along channels of length 5mm or 7mm.

Protein separations

Figure 5.2(a) shows μPLE migrative profiles of several fluorescently-labeled proteins of varying molecular weight, plotted as distance traveled along the gel (%T, %C) vs. time (V-hr). Eluted species include trypsin inhibitor (TI, 21.5kDa), green fluorescent protein (GFP, 27kDa), ovalbumin (OVA, 43kDa), bovine serum albumin (BSA, 67kDa), transferrin (Tfer, 77kDa), BSA dimer (BSA', 134kDa), and TNFα monoclonal antibody (MAb, 144kDa). It is evident that all species easily traverse the initial (large pore) region, and then are abruptly slowed once they approach their pore limit. These profiles are consistent with previous reports of migrative patterns along PLE slab gels with similar porosity gradients; in particular the behaviors of trypsin inhibitor (TI), ovalbumin (OVA), and bovine serum albumin (BSA) show good agreement with data from Campbell *et al* [99] of the same species migrating along 3%T, 4%C → 40%T, 12.5%C gels.

While initial separations are based on both the molecular weight and charge of a given analyte, in PLE the separations will ultimately be dependent primarily on M_r as the proteins migrate into the less porous regions of the gel. The molecular weight distribution should have a logarithmic dependence on the gel concentration, according to the Ferguson relationship, equation (5.1). This has been shown for high molecular weight samples ($M_r > 50$kDa) on gels with lower %T and %C limits [107]. The μPLE system presented here allows for fractionation of lower molecular weight samples due to the higher acrylamide and bisacrylamide concentrations employed. Figure 5.2(b) shows a plot of the approximate pore limit vs. molecular weight for the separated species in Figure 5.2(a), taken as the position of the plug following 2000 V-hr of separation. The small deviations from linearity are most likely due to the unknown effects of crosslinking variations on the gel pore size.
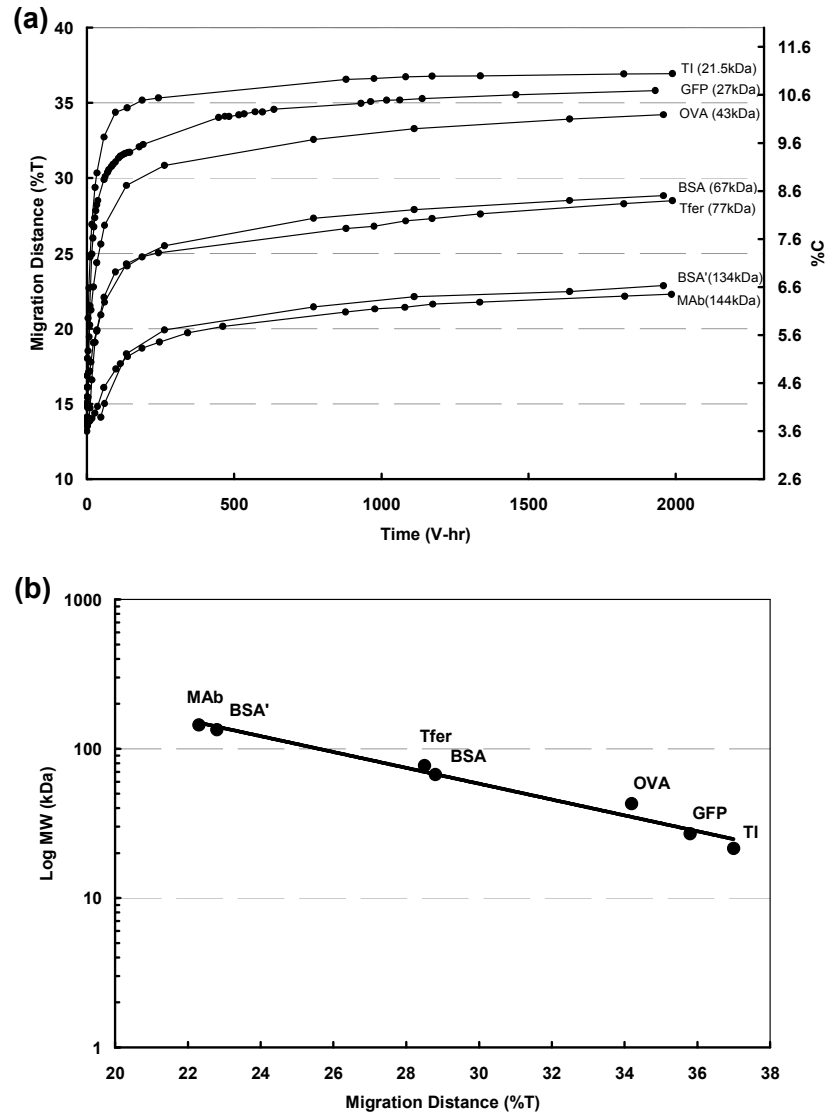
Figure 5.2. (a) Pore limit electrophoresis profiles of several proteins along μPLE channel with 40V applied for ~50 hours. Eluted species: trypsin inhibitor (TI), green fluorescent protein (GFP), ovalbumin (OVA), bovine serum albumin (BSA), BSA dimer (BSA'), transferrin (Tfer), and TNFα monoclonal antibody (MAb). (b) Pore limit vs. molecular weight following 2000 V-hr electrophoresis.

Under normal electrophoresis conditions, an injected Gaussian plug will gradually disperse and broaden as it migrates through the separation channel. However in PLE, due to the dispersion coefficient diminishing with reduced porosity and the inherent stacking phenomenon associated with the analyte's decreasing mobility, the sample plug will instead sharpen into a tighter band as it travels further down the gel. Figure 5.3 shows intermittent fluorescence profiles of a band of Alexa-647 labeled transferrin injected into

78

a 7mm-long µPLE gel. Note that the band remains essentially Gaussian through the early, more porous region of the gel, but starts to exhibit some "tailing" as it approaches its pore limit. This effect can most likely be attributed to residual sample from the loading (side) channel slowly being drawn into the gel, as well as a distribution in molecular weight of the sample due to, among other things, non-homogeneous labeling using the AlexaFluor dyes.
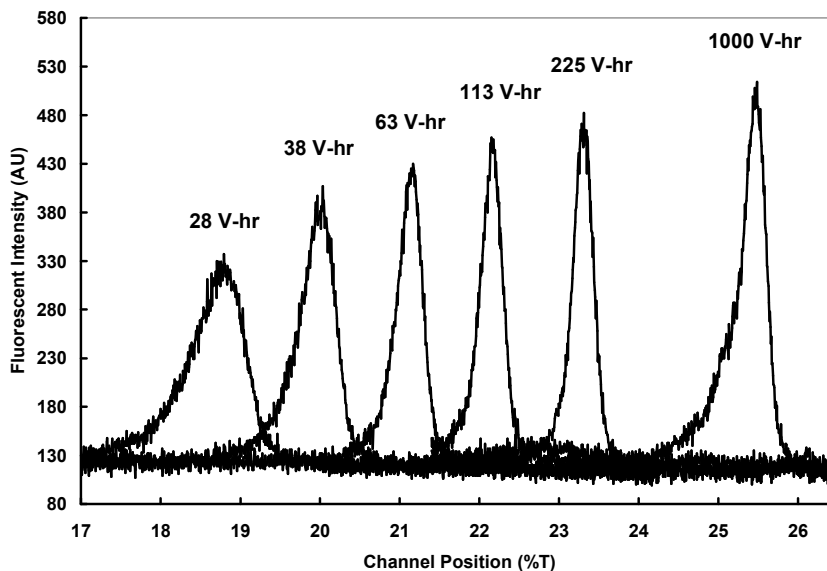
Figure 5.3. Fluorescent intensity profiles at various time intervals of Alexa-647 labeled transferrin migrating through 7mm-long µPLE channel under 50V applied.

Effect of electric field strength

To evaluate the effect of varying the electric field strength on the µPLE behavior of migrated proteins, a sample consisting of both OVA and BSA were loaded onto two separate 7mm-long gels and separated with 20V and 100V applied voltages. Figure 5.4(a) shows the individual migration profiles plotted vs. real time (hr), while Figure 5.4(b) displays the same data with time converted to V-hr. This plot simply shows that a sample plug will exhibit the same transport behavior when time is plotted as V-hr, therefore faster sample fractionation can be achieved by designing the µPLE channel to withstand higher electric fields. In this system ,high electric fields tend to eventually induce bubbles in the gel due to disruptions in the covalent bonds between the polyacrylamide and the silanized channel wall.
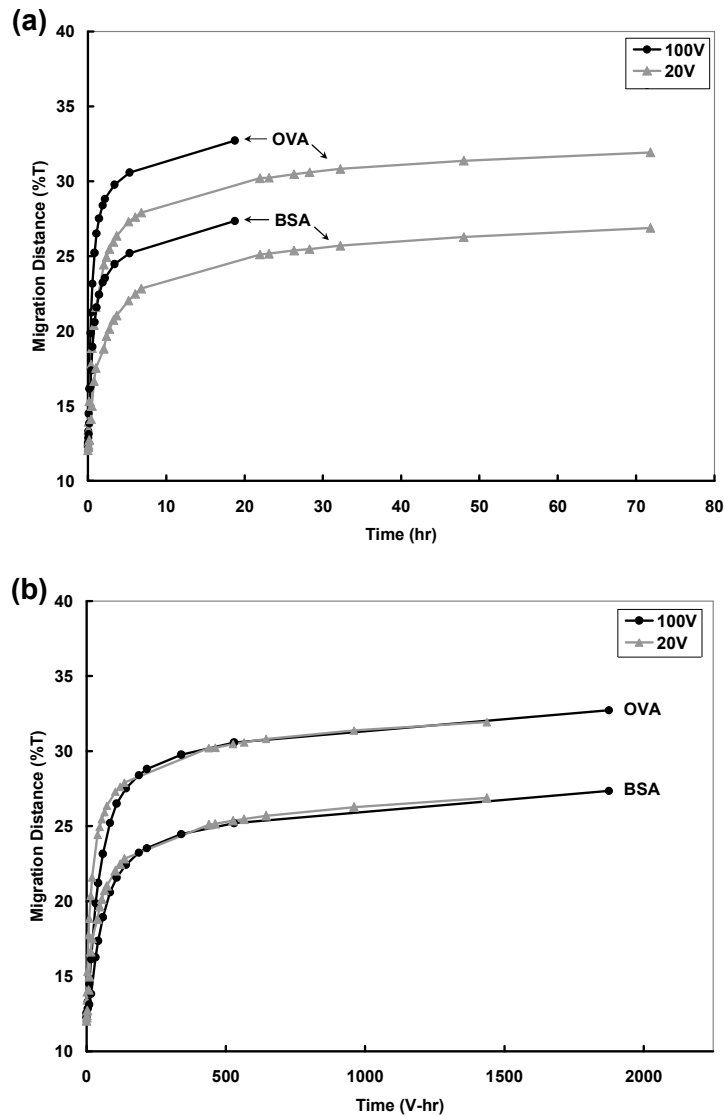
Figure 5.4. Migration profiles of OVA-488 and BSA-647 under two different applied voltages along 7mm-long µPLE channel. Circles: 100V, triangles: 20V. (a) Time plotted in hrs, (b) Time plotted in V-hr.

Stable preconcentration due to stacking phenomenon

Due to the inherent decelerating mobility of analytes as they traverse through the µPLE gels, this system provides a stable stacking mechanism and can be used to preconcentrate dilute species in solution. To demonstrate the preconcentration ability of the system, a solution of 100pM BSA and 100pM OVA was flushed into the open side channel along the 10%T side of a 5mm-long fabricated µPLE device and loaded continuously into the gel for ~3500V-hr. Figure 5.5(a) shows fluorescent intensity

profiles of the BSA sample along the gel captured at various time intervals. This plot shows the stacking and "tailing" behavior expected due to loading from a constant concentration source.

Figure 5.5(b) and (c) plot the maximum fluorescent intensity of the focused plugs vs. time. The maximum intensities are compared with those of concentration standards measured in open channels on the same device. Figure 5.5(b) shows that the BSA achieves a ~40,000-fold concentration factor following 3500V-hr of loading. This preconcentration will continue at an approximately linear rate as long as sample is being loaded.
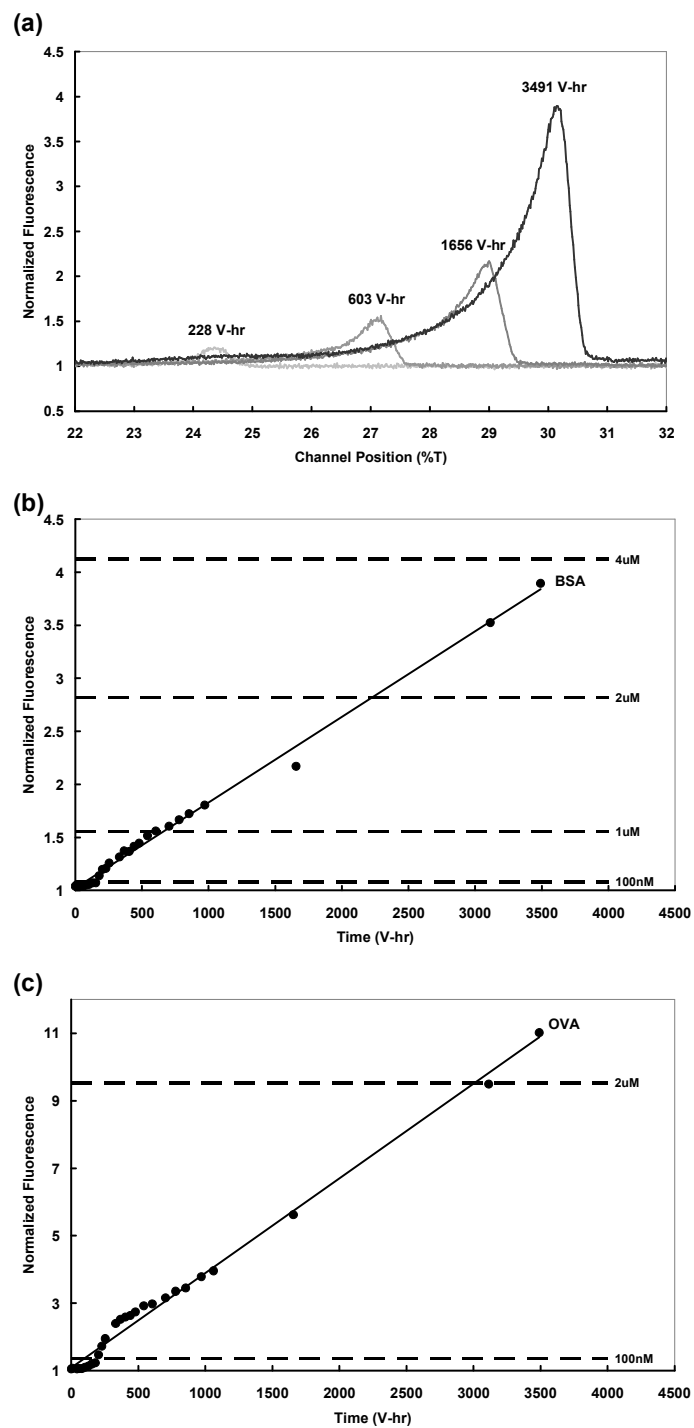
Figure 5.5. (a) Fluorescence intensity profiles of 100pM BSA migrated across 5mm-long µPLE channel under 150V at various time increments. (b)-(c) Concentration vs. time profiles of 100pM (b) BSA and (c) OVA under 150V. Maximum fluorescent intensities compared with concentration standards (dashed lines).

Conclusion

In this chapter, a method for establishing an on-chip polyacrylamide porosity gradient is presented and used for microscale pore limit electrophoresis (μPLE) of several proteins. Porosity is controlled through linear spatial gradients of acrylamide monomer and bisacrylamide crosslinker concentrations. Species are shown to migrate at unique rates through the μPLE gel and eventually approach an "effective" pore limit – the gel concentrations at which a protein nearly halts its migration due to its molecular size. Band width sharpening of an injected plug is due to the decelerating mobility and resulting stacking effect of a species traversing the porosity gradient. This same effect can also be exploited to provide preconcentration of a dilute species continuously loaded into the gel.

The μPLE method can be employed as a mechanism for on-chip multi-dimensional separations as a means to further resolve complex samples, such as blood serum. The fabrication technique may also be adapted to enable miniaturization of transverse pore gradient electrophoresis, a related technique in which samples are separated laterally along porosity gradients [108].

Perhaps a more interesting application of this technique is in the fabrication of a polyacrylamide membrane array for the fractionation of complex samples. Polyacrylamide size-exclusion membranes have been used to preconcentrate biological analytes-of-interest prior to separation [6]. By establishing an acrylamide/bisacrylamide gradient, we can selectively polymerize membranes of any concentration at different locations along a microchannel. Injected protein samples can then be fractionated into different size-dependent regions and manipulated for further analysis. μPLE plots such as Figure 5.2(a) can be used to design these size-based fractionation devices.

CHAPTER 6

CONCLUSIONS AND FUTURE WORK

Conclusions

The work presented in this dissertation is aimed at developing simple on-chip techniques for rapid concentration and separation of protein samples. Three independent projects are presented in which protein species uniquely focus along an imposed gradient based on molecular variations between sample analytes.

Chapters 2 and 3 present an experimental and numerical analysis of Temperature Gradient Focusing via Joule Heating, a mechanism in which an analyte's electrophoretic migration is balanced by the bulk fluid velocity at a unique temperature in the channel. Focusing is demonstrated along variable-width microchannels in which the electric field used to induce electrokinetic motion also imposes a temperature gradient due to Joule heating. Concentration factors > 500 are demonstrated in < 10 minutes for several analytes, including BSA and insulin. Numerical results show good agreement with experimental behavior, validating the model as a useful tool in device design.

Chapter 4 presents the first implementation of IPG-IEF methodology into a microscale format (μIPG's). Due to their stability and separation efficiency, μIPG's provide improved performance over conventional on-chip IEF in which carrier ampholytes are used to establish free-flow pH gradients. Commercial macroscale IPG strips (7 – 18 cm long) are frequently used for 2-D separations, however μIPG's allow for much faster separations (< 20 minutes) over their macroscale counterpart (12 – 30 hours), and also use significantly less sample volume. It is also shown that peak resolution, $\Delta(\text{p}I)_{\min}$, is independent of channel length given equal applied voltage. $\Delta(\text{p}I)_{\min} \approx 0.040$

is demonstrated. Therefore µIPG resolution is comparable to that achieved with commercial IPG strips.

Finally, chapter 5 employs a similar procedure used in µIPG fabrication to establish a polyacrylamide porosity gradient in a channel for microscale pore limit electrophoresis (µPLE). Proteins are separated and enriched based on their effective "pore limit" – the pore size at which a protein's electrophoretic migration is nearly halted due to its molecular size. Peak resolution is shown to improve as a plug traverses the porosity gradient due to the inherent stacking phenomenon of a decelerating sample. This phenomenon is also used to provide stable preconcentration of dilute samples, with concentration factors > 40,000 easily demonstrated.

Future Work

All three on-chip mechanisms presented here can be applied to future devices for enhanced detection and separation of target analytes. The simple fabrication procedures allow for relatively easy implementation with other chip-based techniques. This section will outline future work to be done for each project, and will highlight three conceptual devices that stem from the technology presented in this proposal.

Temperature Gradient Focusing via Joule Heating

While we have experimentally shown that our TGF device is able to separate a pair of target analytes along its axis, perhaps its most useful application is that of a preconcentrator for a single analyte. TGF may be especially effective in preconcentrating samples diluted in biological fluids as the high concentration 900mM Tris-Borate buffer most commonly employed is relatively unaffected by the presence of background salts in the sample solution. Preliminary data has shown consistent focusing of FITC-insulin with 100mM NaCl added as a background electrolyte. Another benefit of TGF is that, unlike many membrane-based preconcentration mechanisms, background salts and other

ions are not focused with the analyte; the focused plug remains in the same initial buffer solution concentrations.

With these clear advantages, TGF seems to be a proper candidate for implementation in assays where preconcentration of dilute biological samples is required. One such application is the competitive immunoassay described below and illustrated in Figure 6.1(a). Here, a biological sample is diluted in the 900mM Tris-borate buffer and loaded into the diverging TGF channel for sample enrichment. Upon preconcentrating the sample, the pneumatic valves (atop the channel, embedded in the PMDS slab) are activated to seal off the central concentration region. This finite aqueous volume is then transferred into a pressure-driven oil stream as a droplet to maintain its enhanced concentration. Adjoining channels then add fluorescently-labeled antigen (Ag*) and its appropriate antibody (Ab) to the droplet, as is standard for competitive immunoassays. A fluorescence polarization detector downstream can then measure the presence and corresponding concentration of analyte in the sample.

An additional benefit of this system is that it allows for assay parallelization, as shown in Figure 6.1(b). The TGF preconcentration mechanisms can be independently operated while feeding a continuous oil stream leading to the Ag* stream, Ab stream, and FP detector. In this manner, sample throughput is enhanced allowing for simultaneous analysis of multiple samples.
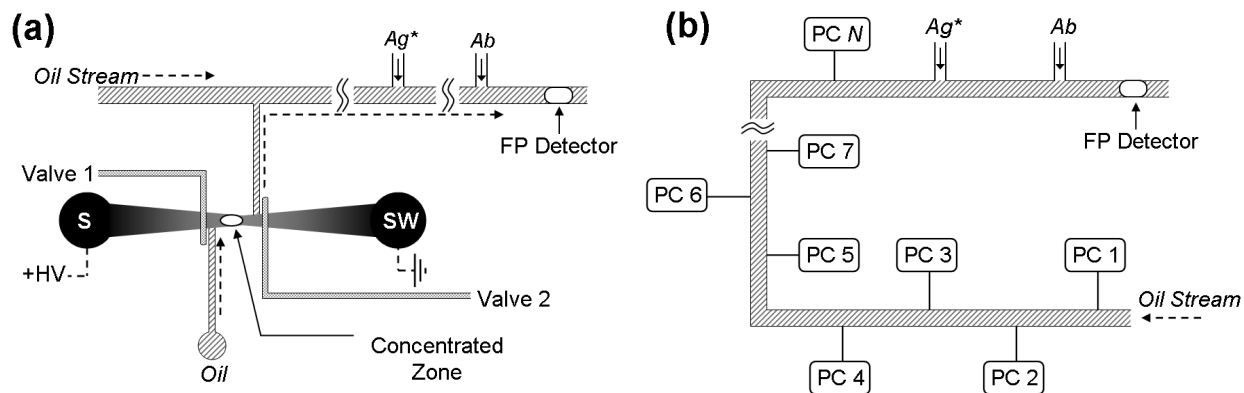
Figure 6.1. Conceptual competitive immunoassay employing TGF for analyte preconcentration. (a) Aqueous sample solution is loaded into TGF channel (S-SW) for sample enrichment. Pneumatic valves are used to contain the concentrated sample in a fixed volume. An oil stream is then pumped through TGF channel such that a droplet is formed with the target analyte. Fluorescently-labeled antigen (Ag*) and antibody (Ab) are added to the droplet in fixed concentrations prior to calibrated detection using fluorescence polarization (FP). (b) For enhanced throughput, this system allows for several preconcentrators (PC) to be operated in parallel, with the enriched samples being continuously fed into the adjoining oil stream. The Ag* stream, Ab stream, and FP detector serve all subsidiary PC systems.

Microscale Immobilized pH Gradients

The results presented in Chapter 4 show that μIPG's enable rapid and stable isoelectric focusing on microdevices. The core principles and processes for fabricating and operating μIPG's seem to be adequately developed. Further improvements in pH profile linearity (Figure 4.3b) may stem from better understanding of the acrylamido buffer solutions used in the fabrication, as more robust recipes may improve the buffering capacity homogeneity across the channel and yield a more linear pH gradient. Further work may also involve device design such that the membrane, used to ensure a linear species distribution prior to polymerization, can be eliminated from the fabrication procedure.

The natural progression of microscale IEF is to incorporate the μIPG with another separation mechanism for a 2-D separation. Macroscale IPG strips are typically transferred to a slab gel following IEF for a sized-based separation in the second dimension. A similar technique can be achieved on-chip, such as with the device featured in Figure 6.2 below. Here, the μIPG channel is abutted with orthogonal

separation channels for traditional PAGE in the second dimension. Each channel corresponds to a unique pH range to provide additional resolution in the separation. This configuration would also allow for sodium dodecyl sulfate (SDS) to be soaked into the µIPG gel following IEF such that SDS-PAGE could be achieved in the second dimension. SDS is an anionic surfactant that denatures and binds to proteins with a concentration proportional to the protein's mass. In this manner the protein's unique charge is masked and its migrative pattern through the gel is strictly based on its mass.
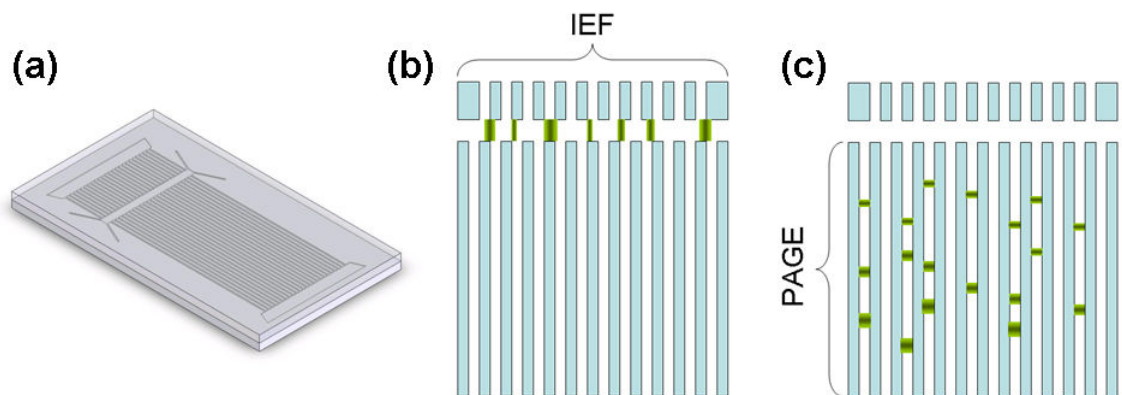
Figure 6.2. Conceptual two-dimensional IEF-PAGE separation device. (a) Device layout. (b) µIPG is established to enable isoelectric focusing across first dimension. (c) Remainder of device consists of polyacrylamide channels for size-based gel electrophoresis of IEF products. Device could also be designed to soak µIPG with SDS following IEF step such that second dimension is SDS-PAGE.

IEF-PAGE is a standard laboratory protocol for separating and sizing complex samples. Gels and reagents are commercially available from several companies, making the separation results independent of laboratory influences. Unfortunately, IEF-PAGE is a lengthy procedure typically requiring > 30 hours and several attentive loading and rinsing steps from laboratory technicians, making the technique undesirable if rapid results are necessary. Additionally, the method requires large sample volumes in order to meet the instrumental limits of detection.

Proper miniaturization of IEF-PAGE would provide a rapid, low-volume analytical procedure while retaining the resolution required in sample analysis. It would also preserve the separation profiles with which technicians and researchers are acquainted. Prior attempts to miniaturize IEF-PAGE have fallen short due to the

difficulties associated with conventional free-flow IEF in microdevices. However, the device depicted in Figure 6.2 may enable the stability and reliability required for this application. This device could also be integrated into a fully-automated platform such that attentive loading, rinsing, and detection would be eliminated.

Microscale Pore Limit Electrophoresis

The µPLE results presented in Chapter 5 show that this technique provides high resolution protein sizing and stable preconcentration. While effective, the assays shown here require significantly longer operations than the other techniques presented in this work. The increased assay times are mainly due to the slow migration of samples through the higher concentration regions of the gel, and the inability to apply large electric fields to µPLE gels without inducing bubbles and other disruptions in the gel. Therefore future work could be focused toward improving assay times by a) reducing the length of the µPLE gel, and b) improving the bond strength between the gel and silanized channel wall. Equation 5.6 shows the exponential increase in concentration factor achievable by increasing the electric field and reducing the channel length.

Perhaps the most useful application of this technique lies in the sized-based fractionation of complex samples. Polyacrylamide membranes have been previously shown to provide stable analyte preconcentration [6, 75]. Consider the device shown in Figure 6.3. A porosity gradient is established along the main channel, as previously shown. However, instead of polymerizing the entire channel, membranes are selectively polymerized near the intersections of orthogonal channels which will capture fractionated species. As a complex sample is introduced to the system, proteins will be selectively retained or permitted through each membrane, based on their sizes. In this manner, the membranes serve as a sort of "low-pass" filter for samples. µPLE migration patterns, such as in Figure 5.2(a), provide the means to design such a system. One can imagine simple systems with just one fractionation membrane to filter out unwanted species, or complex arrays of membranes that provide high resolution protein fractionation and separation. This system can also be applied to other biological samples, such as DNA and RNA, where sized-based separation is required.
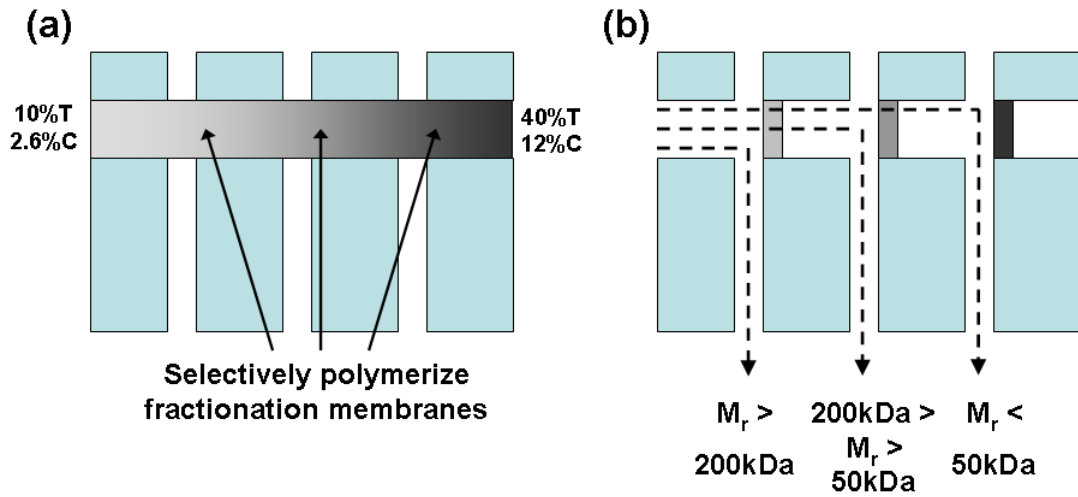
Figure 6.3. Conceptual fractionation device utilizing µPLE principle. (a) Acrylamide porosity gradient is established, but instead of polymerizing entire device, membranes are selectively polymerized near intersections. (b) Fractionation membranes enable sized-based exclusion of proteins such that complex samples are selectively separated for further analysis.

APPENDICES

APPENDIX 1

FURTHER DETAILS OF TGF NUMERICAL SIMULATION

The following details the steps used in formulating the Matlab numerical model used in this work. The model is a fundamental transient finite difference scheme solving the governing equations given in the manuscript. The simulations were conducted using a graphical user interface, which can be seen in Figure A1.1.

Calculating ϕ_i

After establishing the flow parameters, boundary values, and initial conditions, the code first solves for the constant current, I, through the channel. I is found iteratively using the *fzero* command. The function calculates ϕ at each point, then compares $\phi(N)$ with the specified $\phi(L)$. The function *fzero* finds the point at which the error = zero. We make an initial guess of:

$$I_{guess} = \frac{L[\phi(L) - \phi(0)]}{\sum_{i=1}^{N} \frac{1}{\sigma_i A_i}} \tag{A1.1}$$

After the program has converged on a solution for I, equation (3.12) can be used to solve for the change in potential at each point:

$$\frac{d\phi_i}{dx} = \frac{I}{\sigma_i A_i} \tag{A1.2}$$

The potential at each point along the channel is then calculated using:

$$\phi_i = \phi_{i-1} + \frac{d\phi_{i-1}}{dx} \tag{A1.3}$$

Note: In calculating first and second derivatives at point i, a central finite difference scheme was used throughout the model, i.e.

92

$$\frac{d\phi_i}{dx} = \frac{(\phi_{i+1} - \phi_{i-1})}{2dx} \tag{A1.4}$$

$$\frac{d^2\phi_i}{dx^2} = \frac{(\phi_{i+1} - 2\phi_i + \phi_{i-1})}{(dx)^2} \tag{A1.5}$$

Calculating P_i

The next step is to solve for the constant mass flow rate, uA, through the channel. Equation (3.2) is calculated at the channel inlet to provide an initial guess for u_{bulk}. The *fzero* command is used to iteratively solve for the mass flow rate using equation (3.1). The function solves for P at each point, and runs until the error between $P(N)$ and the imposed $P(L)$ is zero. Once the mass flux is known, the bulk velocity at each point, $u_{bulk,i}$, can be easily calculated.

Equation (3.2) is then used to solve for the pressure gradient at each point.

$$dP_i = \frac{-32\eta_i dx}{d_{h,i}^2} \left(u_{bulk,i} - \left(\frac{\varepsilon_0 \varepsilon_i \zeta_i}{\eta_i} \right) \frac{d\phi_i}{dx} \right) \tag{A1.6}$$

The pressure at each point is calculated as

$$P_i = P_{i-1} + \frac{dP_{i-1}}{dx} \tag{A1.7}$$

Calculating T_i and c_i

To calculate the temperature and concentration at each point in the channel, we used the Crank-Nicolson scheme, an inherently stable implicit formulation. Equations (3.7) and (3.13) are each discretized and solved at each time step. As an example of this method, we will walk through the process for solving for the concentration, c_i.

$$A_i \left(\frac{c_i^{n+1} - c_i^n}{dt} \right) = A_i D_{eff,i} \left(\frac{c_{i+1} - 2c_i + c_{i-1}}{dx^2} \right) + \left(A_i \frac{dD_{eff,i}}{dx} + D_{eff,i} \frac{dA_i}{dx} + A_i \mu_{ep,i} \frac{d\phi_i}{dx} - A_i u_{bulk,i} \right) \left(\frac{c_{i+1} - c_{i-1}}{2dx} \right) + \cdots$$

$$\cdots + \left(A_i \frac{d\mu_{ep,i}}{dx} \frac{d\phi_i}{dx} + \mu_{ep,i} \frac{dA_i}{dx} \frac{d\phi_i}{dx} + A_i \mu_{ep,i} \frac{d^2\phi_i}{dx^2} - A_i \frac{du_{bulk,i}}{dx} - u_{bulk,i} \frac{dA_i}{dx} \right) c_i \tag{A1.8}$$

The Crank-Nicolson scheme calculates the right-hand side as the average of the concentration changes from *time* = *n* to *time* = *n+1*. For simplicity, we will denote:

$$\alpha_i = \frac{D_{eff,i}\,dt}{2dx^2} \tag{A1.9}$$

$$\beta_i = \left(A_i \frac{dD_{eff,i}}{dx} + D_{eff,i}\frac{dA_i}{dx} + A_i \mu_{ep,i}\frac{d\phi_i}{dx} - A_i u_{bulk,i} \right)\frac{dt}{4A_i dx} \tag{A1.10}$$

$$\gamma_i = \left(A_i \frac{d\mu_{ep,i}}{dx}\frac{d\phi_i}{dx} + \mu_{ep,i}\frac{dA_i}{dx}\frac{d\phi_i}{dx} + A_i\mu_{ep,i}\frac{d^2\phi_i}{dx^2} - A_i \frac{du_{bulk,i}}{dx} - u_{bulk,i}\frac{dA_i}{dx} \right)\frac{dt}{2A_i} \tag{A1.11}$$

The formulation then becomes:

$$c_i^{n+1} - c_i^n = \alpha_i\left[\left(c_{i-1}^{n+1} - 2c_i^{n+1} + c_{i+1}^{n+1}\right) + \left(c_{i-1}^n - 2c_i^n + c_{i+1}^n\right)\right] + \beta_i\left[\left(c_{i+1}^{n+1} - c_{i-1}^{n+1}\right) + \left(c_{i+1}^n - c_{i-1}^n\right)\right] + \gamma_i\left(c_i^{n+1} + c_i^n\right) \tag{A1.12}$$

Or,

$$c_{i-1}^{n+1}(-\alpha_i + \beta_i) + c_i^{n+1}(1 + 2\alpha_i - \gamma_i) + c_{i+1}^{n+1}(-\alpha_i - \beta_i) = c_{i-1}^n(\alpha_i - \beta_i) + c_i^n(1 - 2\alpha_i + \gamma_i) + c_{i+1}^n(\alpha_i + \beta_i) \tag{A1.13}$$

The left-hand side of this equation is represented as a product of a vector and tridiagonal matrix. The right hand side is kept as a vector. The formulation is then written in matrix form as:

$$
\underbrace{\begin{bmatrix}
1+2\alpha_1-\gamma_1 & -\alpha_1-\beta_1 & 0 & \cdots & 0 \\
-\alpha_2+\beta_2 & 1+2\alpha_2-\gamma_2 & -\alpha_2-\beta_2 & 0 & 0 \\
0 & -\alpha_3+\beta_3 & 1+2\alpha_3-\gamma_3 & \ddots & 0 \\
\vdots & 0 & \ddots & \ddots & -\alpha_{N-1}-\beta_{N-1} \\
0 & 0 & 0 & -\alpha_N+\beta_N & 1+2\alpha_N-\gamma_N
\end{bmatrix}}_{A}
\underbrace{\begin{bmatrix}
c_1^{n+1} \\ c_2^{n+1} \\ c_3^{n+1} \\ \vdots \\ c_N^{n+1}
\end{bmatrix}}_{c^{n+1}}
=
\underbrace{\begin{bmatrix}
c_1^n(1-2\alpha_1+\gamma_1)+c_2^n(\alpha_1+\beta_1) \\
c_1^n(\alpha_2-\beta_2)+c_2^n(1-2\alpha_2+\gamma_2)+c_3^n(\alpha_2+\beta_2) \\
c_2^n(\alpha_3-\beta_3)+c_3^n(1-2\alpha_3+\gamma_3)+c_4^n(\alpha_3+\beta_3) \\
\vdots \\
c_{N-1}^n(\alpha_N-\beta_N)+c_N^n(1-2\alpha_N+\gamma_N)
\end{bmatrix}}_{R}
$$

The model first calculates the α, β, and γ values at each point, then establishes the tridiagonal matrix using the *spdiags* function. The next step is to establish the right-hand side vector using the known concentration values at the current time step, n. The concentration at the subsequent time step, n+1, is then calculated as:

$$c^{n+1} = R \cdot A^{-1} \tag{A1.14}$$

In order to smooth out the oscillations in the transient solutions, the following moving average was employed:

$$c_i^{n+1} = (2c_i^n + 2c_i^{n+1}) / 4 \tag{A1.15}$$

The time step, dt, is calculated using the following stability recommendation.

$$dt \cong \frac{N(dx)^2}{2D_{eff,max}} \tag{A1.16}$$

The same basic structure is used to calculate the temperature using equation (3.13).
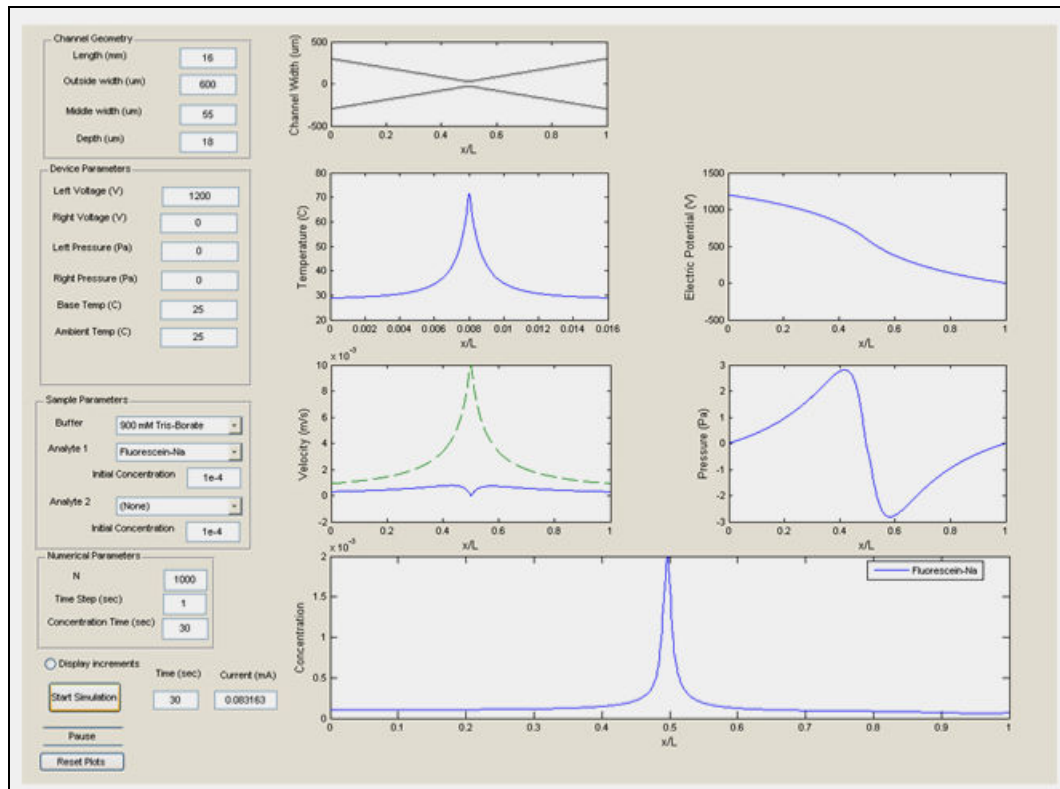
Figure A1.1 - Screen shot of Matlab graphical user interface (GUI) used to run simulations.

APPENDIX 2

FURTHER DETAILS OF μIPG ESTABLISHMENT, NUMERICAL SIMULATION, AND RESOLUTION THEORY

THEORY

pH gradient generation

The following fundamental equations are used in depicting monomeric diffusion and the resulting pH profile across the channel.

The concentration, c, of a species i at any location in the channel is governed by the simple diffusion equation,

$$\frac{\partial c_i}{\partial t} = D_i \frac{\partial^2 c_i}{\partial x^2} \tag{A2.2}$$

where D is the diffusion coefficient, t is time, and x is a coordinate along the length of the channel. Note that in this system we allow sufficient time for linear equilibration (t_{SS}) across our separation channel of length L. For our system $L = 6$mm, and thus $t_{SS} > \sim 12$ hours. Because $t_{SS} \propto L^2$, the monomeric distributions and pH gradient at different times is very much dependent on the channel length. This relationship can also be used to establish non-linear gradients.

The ionization equilibrium of each species in solution, both acidic and basic Immobilines, as well as the water are governed by the following well-known expressions,

$$K_{i,acidic} = \frac{[B_i^-][H^+]}{[B_i^0]} \tag{A2.2}$$

$$K_{i,basic} = \frac{[B_i^0][H^+]}{[B_i^+]} \tag{A2.3}$$

$$K_{water} = [H^+][OH^-] = 10^{-8}\,mol \cdot m^{-3} \tag{A2.4}$$

where K is the equilibrium constant, B^0 denotes a neutral species, and B^- and B^+ denote ionic species.

Each Immobiline has a unique pK, with the pK defined as,

$$\text{p}K = -log_{10}\,K \tag{A2.5}$$

The pH of the solution is calculated as,

$$\text{pH} = -log_{10}\,[H+] \tag{A2.6}$$

Finally, to complete our formulation, electroneutrality within solution requires that,

$$\sum_i c_i z_i = 0 \tag{A2.7}$$

where z_i is the net charge on species i.

Equations (A2.2) – (A2.7) can be solved simultaneously to calculate the pH at any location in the channel, given the local concentration of all Immobilines. Note that the local pH can be quite sensitive to even minor fluctuations in Immobiline concentrations, therefore it is imperative to maintain precise control over species distributions when fabricating immobilized pH gradients.

NUMERICAL SIMULATION

The governing diffusion and chemical equilibrium equations [equations (A2.1) – (A2.7)] were implemented into a 1-D numerical model to formulate a recipe for a desired pH profile based on the diffusion of Immobiline species across the separation channel, similar to models developed previously. The new experimental fabrication method employed here maintains precise control over time-dependent distributions provided diffusion coefficients of each monomer can be established, and therefore the model accurately predicts the pH profile for both linear and nonlinear Immobiline gradients. The model was created using Matlab (Mathworks, Natick, MA).

The concentration profile of each species along the discretized channel was found by solving equation (A2.1) using a Crank-Nicolson formulation at each node. The

boundary conditions were set such that $c_i(x=0)$ and $c_i(x=L)$ were prescribed, and the initial condition at each node within the channel was set such that $c_i(t=0) = 0$.

Equations (A2.2) – (A2.7) were implemented such that the pH at each location in the channel could be calculated based on the resulting concentration profiles of each Immobiline species. An iterative solver evaluates the concentrations of each ionic and neutral species at a node using equations (A2.2) - (A2.4), and adjusts those concentrations based on evaluation of equation (A2.7). Once electroneutrality was achieved to within a specified tolerance, the final pH was calculated using equation (A2.5).

The simulation was run using a graphical user interface (GUI) to allow simple user control over parameters such as Immobiline pK's and boundary concentrations, channel length, equilibration time, as well as convenient visualization of the final concentration and pH profiles.

SEPARATION EFFICIENCY

We first assume the bands focused via IEF exhibit a Gaussian distribution. Then their theoretical standard deviation of concentration can be estimated as

$$\sigma = \left(\frac{D/E}{-\dfrac{d\mu}{d(pH)}\dfrac{d(pH)}{dx}} \right)^{1/2} \tag{A2.8}$$

where E is the electric field strength, D is the analyte diffusion coefficient and μ is the analyte mobility. $d\mu/d(pH)$ denotes the mobility change around the pI of an analyte. Note that the square of the standard deviation, σ^2, is referred to as the band variance. The resolution between two bands of pI difference $\Delta(pI)$ can be approximated simply using R_s = $\Delta X/4\sigma$. Assuming $\Delta X = \dfrac{\Delta(\mathrm{p}I)}{d(pH)/dx}$ this yields:

$$R_s = \frac{\Delta(\mathrm{p}I)}{4} \left(\frac{E - d\mu/d(pH)}{D} \frac{}{d(pH)/dx} \right)^{1/2} \tag{A2.9}$$

Assuming a linear pH gradient such that $d(pH)/dx = \Delta pH/L$ and a uniform electric field such that $E = V/L$, equation (A2.9) can be rearranged to yield an expression for the $\Delta(pI)_{min}$ that can be resolved for unit resolution:

$$\Delta(pI)_{min} = 4\left(\frac{D}{V}\frac{\Delta pH}{-d\mu/d(pH)}\right)^{1/2} \qquad (A2.10)$$

REFERENCES

REFERENCES

1 The Big Lebowski (1998). Dir. Coen J and Coen E. Polygram Filmed Entertainment. Distributed by MCA / Universal Home Video. Universal City, CA. video recording.

2 Cho WS (2007) *Genomics, Proteomics & Bioinformatics* 5: 77-85.

3 Yager P, Edwards T, Fu E, Helton K, Nelson K, Tam MR and Weigl BH (2006) *Nature* 442: 412-418.

4 Khandurina J, Jacobson SC, Waters LC, Foote RS and Ramsey JM (1999) *Anal. Chem.* 71: 1815-1819.

5 Foote RS, Khandurina J, Jacobson SC and Ramsey JM (2005) *Anal. Chem.* 77: 57-63.

6 Hatch AV, Herr AE, Throckmorton DJ, Brennan JS and Singh AK (2006) *Anal. Chem.* 78: 4976-4984.

7 Wang YC, Stevens AL and Han J (2005) *Anal. Chem.* 77: 4293-4299.

8 Kim SM, Burns MA and Hasselbrink EF (2006) *Anal. Chem.* 78: 4779-4785.

9 Gebauer P and Bocek P (2002) *Electrophoresis* 23: 3858-3864.

10 Koegler WS and Ivory CF (1996) *Journal of Chromatography A,* 726: 229-236.

11 Petsev DN, Lopez GP, Ivory CF and Sibbett SS (2005) *Lab Chip* 5: 587-597.

12 Herr AE, Molho JI, Drouvalakis KA, Mikkelsen JC, Utz PJ, Santiago JG and Kenny TW (2003) *Anal. Chem.* 75: 1180-1187.

13 Tan W, Fan ZH, Qui CX, Ricco AJ and Gibbons I (2002) *Electrophoresis* 23: 3638-3645.

14 Han J and Craighead HG (2002) *Anal. Chem.* 74: 394-401.

15 Bjellqvist B, Ek K, Righetti PG, Gianazza E, Gorg A, Westermeier R and Postel W (1982) *J Biochem. Biophys. Meth.* 6: 317-339.

16 Righetti PG and Bossi A (1998) *Anal. Chim. Acta* 372: 1-19.

17 Huang Z and Ivory CF (1999) *Anal. Chem.* 71: 1628-1632.

18 Ross D and Locascio LE (2002) *Anal. Chem.* 74: 2556-2564.

19 Balss KM, Ross D, Begley HC, Olsen KG and Tarlov MJ (2004) *J. Am. Chem. Soc.* 126: 13474-13479.

20 Balss KM, Vreeland WN, Phinney KW and Ross D (2004) *Anal. Chem.* 76: 7243-7249.

21 Melcor Thermoelectric Coolers. http://www.melcor.com/OptoTEC_%20Series/1.5-31-F2A.PDF.

22 Duffy DC, McDonald JC, Schueller OJA and Whitesides GM (1998) *Anal. Chem.* 70: 4974-4984.

23 McDonald JC, Duffy DC, Anderson JR, Chiu DT, Wu H, Schueller OJA and Whitesides GM (2000) *Electrophoresis* 21: 27-40.

24 Chang W, Akin D, Sedlak M, Ladisch MR and Bashir R (2003) *Biomed. Microdevices* 5: 281-290.

25 Sakakibara J and Adrian RJ (1999) *Exp. Fluids* 26: 7-15.

26 Ross D, Gaitan M and Locascio LE (2001) *Anal. Chem.* 73: 4117-4123.

27 Schrum KF, Lancaster III JM, Johnston SE and Gilman SD (2000) *Anal. Chem.* 72: 4317-4321.

28 Mosier B, Molho J and Santiago J (2002) *Exp. Fluids* 33: 545-554.

29 Sinton D (2004) *Microfluidics and Nanofluidics* 1: 2-21.

30 Hu S, Ren X, Bachman M, Sims CE, Li GP and Allbritton N (2002) *Anal. Chem.* 74: 4117-4123.

31 Makamba H, Kim JH, Lim K, Park N and Hahn JH (2003) *Electrophoresis* 24: 3607-3619.

32 Hu S, Ren X, Bachman M, Sims CE, Li GP and Allbritton N (2003) *Electrophoresis* 24: 3679-3688.

33 Hu S, Ren X, Bachman M, Sims CE, Li GP and Allbritton NL (2004) *Anal. Chem.* 76: 1865-1870.

34 Yu C, Davey MH, Svec F and Frechet JMJ (2001) *Anal. Chem.* 73: 5088-5096.

35 Manz A, Graber N and Widmer HM (1990) *Sensors and Actuators B: Chemical* 1: 244-248.

36 Pritchett TJ (1996) *Electrophoresis* 17: 1195-1201.

37 Ryan T. Kelly,Adam T.Woolley, (2005) *Journal of Separation Science* 28: 1985-1993.

38 Lin S, Li Y, Tolley HD, Humble PH and Lee ML (2006/9/1) *Journal of Chromatography A* 1125: 254-262.

39 Balss KM, Vreeland WN, Howell PB, Henry AC and Ross D (2004) *J. Am. Chem. Soc.* 126: 1936-1937.

40 Erickson D, Sinton D and Li D (2003) *Lab Chip* 3: 141-149.

41 Tang G, Yan D, Yang C, Gong H, Chai JC and Lam YC (2006) *Electrophoresis* 27: 628-639.

42 Chein R, Yang YC and Lin Y (2006) *Electrophoresis* 27: 640-649.

43 Xuan X, Xu B, Sinton D and Li D (2004) *Lab Chip* 4: 230-236.

44 Tang GY, Yang C, Gong HQ, Chai CJ and Lam YC (2005) *Journal of Heat Transfer* 127: 660-663.

45 Horiuchi K and Dutta P (2004) *International Journal of Heat and Mass Transfer* 47: 3085-3095.

46 Petersen NJ, Nikolajsen RPH, Mogensen KB and Kutter JP (2004) *Electrophoresis* 25: 253-269.

47 Gas B (1993) *J. Chromatogr.* 644: 161-174.

48 Wooding RA (2006) *Journal of Fluid Mechanics Digital Archive* 7: 501-515.

49 Tang GY, Yang C, Gong HQ, Chai JC and Lam YC (2006) *Analytica Chimica Acta* 561: 138-149.

50 Probstein RF (2003) Physicochemical Hydrodynamics. John Wiley and Sons, New York.

51 Incropera FP and DeWitt DP (2001) Fundamentals of Heat and Mass Transfer. John Wiley & Sons, Inc., New York.

52 Knox J and McCormack K (1994) *Chromatographia* 38: 207-214.

53 Evenhuis CJ, Guijt RM, Macka M, Marriott PJ and Haddad PR (2006) *Electrophoresis* 27: 672-676.

54 Kirby BJ and Hasselbrink EF,Jr. (2004) *Electrophoresis* 25: 187-202.

55 Galambos P and Forster FK (1998) *Proceedings from uTAS* 1: 189-191.

56 Krouglova T, Vercammen J and Engelborghs Y (2004) *Biophys. J.* 87: 2635-2646.

57 Rezwan K, Studart AR, Voros J and Gauckler LJ (2005) *J Phys Chem B* 109: 14469-14474.

58 Shackman JG, Munson MS, Kan C and Ross D (2006) *Electrophoresis* 27: 3420-3427.

59 O'Farrell PH (1975) *J. Biol. Chem.* 250: 4007-4021.

60 Thormann W, Mosher RA and Bier M (1986) *J. Chromatogr., A* 351: 17-29.

61 Righetti PG (2006) *Electrophoresis* 27: 923-938.

62 Righetti PG, Simo C, Sebastiano R and Citterio A (2007) *Electrophoresis* 28: 3799-3810.

63 Görg A, Obermaier C, Boguth G, Harder A, Scheibe B, Wildgruber R and Weiss W (2000) *Electrophoresis* 21: 1037-1053.

64 Righetti PG (1990) Immobilized pH Gradients: Theory and Methodology. Elsevier, Amsterdam.

65 Hamdan M and Righetti PG (2005) Proteomics Today: Protein Assessment and Biomarkers Using Mass Spectrometry, 2D Electrophoresis, and Microarray Technology. Wiley-VCH, Hoboken.

66 Wu J and Pawliszyn J (1993) *Electrophoresis* 14: 469-474.

67 Wu X, Sze NS- and Pawliszyn J (2001) *Electrophoresis* 22: 3968-3971.

68 Han J and Singh AK (2004) *J. Chromatogr. , A* 1049: 205-209.

69 Albrecht JW and Jensen KF (2006) *Electrophoresis* 27: 4960-4969.

70 Cabrera CR, Finlayson B and Yager P (2001) *Anal. Chem.* 73: 658-666.

71 Huang T and Pawliszyn J (2002) *Electrophoresis* 23: 3504-3510.

72 Zilberstein G, Korol L, Bukshpan S and Baskin E (2004) *Proteomics* 4: 2533-2540.

73 Zilberstein GV, Baskin EM, Bukshpan S and Korol LE (2004) *Electrophoresis* 25: 3643-3651.

74 Righetti PG (2007) *Electrophoresis* 28: 545-555.

75 Herr AE, Hatch AV, Throckmorton DJ, Tran HM, Brennan JS, Giannobile WV and Singh AK (2007) *PNAS* 104: 5268-5273.

76 Altland K (1990) *Electrophoresis* 11: 140-147.

77 Giaffreda E, Tonani C and Righetti PG (1993) *J. Chromatogr. , A* 630: 313-327.

78 Giddings JC and Dahlgren K (1971) *Sep. Sci.* 6: 345.

79 Das C and Fan ZH (2006) *Electrophoresis* 27: 3619-3626.

80 Rilbe H (1973) *Ann. N. Y. Acad. Sci.* 209: 11-22.

81 Giddings JC (1991) Unified Separation Science. John Wiley & Sons, New York.

82 Righetti PG and Bossi A (1997) *Anal. Biochem.* 247: 1-10.

83 Renzi RF, Stamps J, Horn BA, Ferko S, VanderNoot VA, West JAA, Crocker R, Wiedenman B, Yee D and Fruetel JA (2005) *Anal. Chem.* 77: 435-441.

84 Pristinski D, Kozlovskaya V and Sukhishvili SA (2005) *J. Chem. Phys.* 122: 014907.

85 Goding JW (1976) *Journal of Immunological Methods,* 13: 215-226.

86 Schriebl K, Trummer E, Weik R, Lattenmayer C, Müller D, Kunert R, Katinger H and Vorauer-Uhl K (2007) *Electrophoresis* 28: 2100-2107.

87 Richards DP, Stathakis C, Polakowski R, Ahmadzadeh H and Dovichi NJ (1999) *J. Chromatogr. , A* 853: 21-25.

88 Das C, Zhang J, Denslow ND and Fan ZH (2007) *Lab on a Chip* 7: 1806-1812.

89 Li Y, Buch JS, Rosenberger F, DeVoe DL and Lee CS (2004) *Anal. Chem.* 76: 742-748.

90 Herr AE and Singh AK (2004) *Anal. Chem.* 76: 4727-4733.

91 Margolis J and Kenrick KG (1967) *Biochemical and Biophysical Research Communications* 27: 68-73.

92 Margolis J and Kenrick KG (1967) *Nature* 214: 1334-1336.

93 Slater GG (1968) *Analytical Biochemistry* 24: 215-217.

94 Margolis J and Kenrick KG (1968) *Analytical Biochemistry* 25: 347-362.

95 Slater G (1969) *Anal. Chem.* 41: 1039-1041.

96 Blattler DP, Garner F, van Slyke K and Bradley A (1972) *Journal of Chromatography A* 64: 147-155.

97 Margolis J and Wrigley CW (1975) *Journal of Chromatography A* 106: 204-209.

98 Johnson G (1979) *Biochem. Genet.* 17: 499-516.

99 Campbell WP, Wrigley CW and Margolis J (1983) *Analytical Biochemistry* 129: 31-36.

100 Rodbard D, Kapadia G and Chrambach A (1971) *Analytical Biochemistry* 40: 135-157.

101 Fawcett JS, Sullivan JV and Chrambach A (1989) *Electrophoresis* 10: 182-185.

102 Rainwater D, Moore P,Jr, Shelledy W, Dyer T and Slifer S (1997) *J. Lipid Res.* 38: 1261-1266.

103 Chrambach A and Wheeler DL (1994) *Electrophoresis* 15: 1021-1027.

104 Yamaoka T (1998) *Analytica Chimica Acta* 372: 91-98.

105 Ferguson K (1964) *Metabolism* 13: 985.

106 Renzi RF, Stamps J, Horn BA, Ferko S, VanderNoot VA, West JAA, Crocker R, Wiedenman B, Yee D and Fruetel JA (2005) *Anal. Chem.* 77: 435-441.

107 Andersson LO, Borg H and Mikaelsson M (1972) *FEBS Letters* 20: 199-202.

108 Chrambach A and Wheeler DL (1994) *Electrophoresis* 15: 1021-1027.